

HARVARD UNIVERSITY
Graduate School of Arts and Sciences



DISSERTATION ACCEPTANCE CERTIFICATE

The undersigned, appointed by the
Division of Medical Sciences
in the subject of Biological and Biomedical Sciences
have examined a dissertation entitled

*Investigating the Role of Heterogeneity in Breast Cancer and
Experimental Design*

presented by Jessica Faye Olive
candidate for the degree of Doctor of Philosophy and hereby
certify that it is worthy of acceptance.

Signature: 

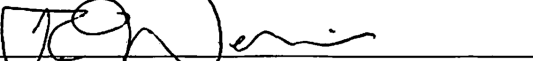
Typed Name: Dr. Marsha Moses

Signature: 

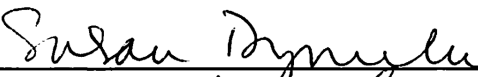
Typed Name: Dr. Kornelia Polyak

Signature: 

Typed Name: Dr. Bruce Zetter

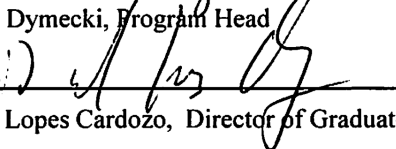
Signature: 

Typed Name: Dr. Robert Weinberg



Dr. Susan Dymecki, Program Head

Date: May 08, 2018



Dr. David Lopes Cardozo, Director of Graduate Studies

Investigating the Role of Heterogeneity in Breast Cancer and Experimental
Design

A dissertation presented

by

Jessica Faye Olive

to

The Division of Medical Sciences

in partial fulfillment of the requirements

for the degree of

Doctor of Philosophy

in the subject of

Biological and Biomedical Sciences

Harvard University

Cambridge, Massachusetts

May 2018

© 2018 Jessica Faye Olive

All rights reserved.

Investigating the Role of Heterogeneity in Breast Cancer and Experimental
Design

Abstract

Breast cancer is predicted to be the most frequent newly diagnosed cancer and second leading cause of cancer-associated death among women in the United States in 2018. Intratumoral heterogeneity plays an important role in disease progression and therapeutic resistance in many types of cancer, including breast cancer. However, the forces that drive heterogeneity, particularly functional heterogeneity, remain largely unknown.

During my doctoral studies, I developed a sequencing based molecular barcoding detection system to track the clonal dynamics of heterogeneous, single-cell derived populations of human and murine breast cancer cells in pre-clinical models. Using these tools, I demonstrated that the host systemic environment influences the degree of heterogeneity of human breast cancer xenografts and that particular systemic changes (such as those induced by the presence of a distant TNBC tumor that is capable of perturbing the immune system) can trigger the outgrowth of tumor cell subpopulations that would otherwise remain dormant. Furthermore, the systemically driven differential

patterns of clonal selection had functional consequences, including variable chemotherapeutic responsiveness.

Additionally, I worked with my colleagues to use heterogeneous, single-cell derived clonal populations of murine breast cancer models to demonstrate the importance of considering functional heterogeneity during experimental design. We demonstrated that a heterogeneous parental cell line could be an inappropriate control for gene-edited cell lines that underwent a selection or subcloning step. Accordingly, heterogeneity must be considered to prevent the generation of false-positive or false-negative results and inaccurate interpretations of data. We employed a modified gene-editing protocol to perform proof-of-concept and discovery studies that provide a model for generating appropriately matched edited and control cell lines when working with functionally heterogeneous populations.

These studies demonstrate for the first time that modulations to the host systemic environment can direct the selection of particular subclonal populations with functional relevance, highlighting the need for an increased understanding of heterogeneity and the processes that guide its formation in experimental disease models and in clinical settings. With an increased understanding of the forces that generate and maintain tumor heterogeneity, it may become possible to interdict the process, potentially slowing disease progression and improving therapeutic outcomes.

Table of Contents

Chapter 1	1
Introduction	1
1.1 <i>Breast Cancer</i>	2
1.1.1 Breast cancer statistics	2
1.1.2 Breast cancer subtype classification	2
1.1.3 Current treatment options	5
1.2 <i>Cancer cell dissemination, dormancy and metastatic outgrowth</i>	6
1.3 <i>Cancer Heterogeneity</i>	7
1.4 <i>Tumor Cell Non-Autonomous Influences</i>	10
1.4.1 Tumor-stromal interactions	10
1.5 <i>Molecular Barcoding</i>	15
1.6 <i>Summary</i>	17
Chapter 2	19
Development of a next-generation sequencing based barcode detection system	19
2.1 <i>Abstract</i>	21
2.2 <i>Introduction</i>	22
2.3 <i>Materials and Methods</i>	24
2.3.1 Cell lines	24
2.3.2 Lentiviral infection	24
2.3.3 Single cell cloning	25
2.3.4 CP pooling	25
2.3.5 Genomic DNA preparations	25
2.3.6 Animal experiments	27
2.3.7 Polymerase chain reaction	27
2.3.8 Illumina sequencing library preparation	29
2.3.9 Next generation sequencing data analysis	32
2.4 <i>Results</i>	33
2.4.1 Generation HMLER clonal cell lines with stably integrated DNA barcodes that are detectable by the PRISM system	33

2.4.2 The PRISM system generates lower barcode detection signals from in vivo samples than in vitro samples	35
2.4.3 Luminex barcodes can be detected using Sanger sequencing	37
2.4.5 PCR-based methods are more suitable for multiplexed Illumina library preparation than low efficiency ligation based methodology	38
2.4.6 PRISM barcodes extracted from both in vitro and in vivo samples can be accurately detected using Illumina next-generation sequencing technology	45
Chapter 3	54
The host systemic environment can direct functionally consequential enhancement of intratumoral heterogeneity	54
3.1 <i>Abstract</i>	56
3.2 <i>Introduction</i>	57
3.3 <i>Materials and Methods</i>	60
3.3.1 Cell lines	60
3.3.2 Lentiviral infection	60
3.3.3 Single cell cloning	61
3.3.4 Clonal population pooling	61
3.3.5 Genomic DNA preparations	61
3.3.6 Long-term proliferation kinetics assays	62
3.3.7 Tumorsphere formation assays	62
3.3.8 Animal experiments	62
3.3.9 Polymerase chain reaction	63
3.3.10 Illumina sequencing library preparation	64
3.3.11 Next generation sequencing data analysis	65
3.3.12 Immunohistochemistry	65
3.3.13 Microscopy and image analysis	65
3.3.14 Flow cytometry	66
3.3.15 LINCS L1000 gene expression analysis	66
3.3.16 Protein arrays	66
3.3.17 ELISAs	67
3.3.18 Cell Titer Glo assays	67
3.3.19 Statistical analysis	68
3.4 <i>Results</i>	69
3.4.1 Generation of a collection of heterogeneous, barcoded clonal populations from the HMLER-HR cell line	69
3.4.2 The activated host-systemic environment is associated with enhanced HMLER ^S intratumoral heterogeneity	71
3.4.3 Enhanced intratumoral heterogeneity in HMLER ^S tumors is associated with differential innate immune cell infiltration	78

3.4.4 A functional innate immune system is required for differential CP selection in N-HSE and A-HSE HMLER ^S tumors	81
3.4.5 Subclonal populations can act cooperatively to generate unique cytokine and chemokine expression patterns	90
3.4.6 HMLER ^S subpools have unique gene expression signatures	95
3.4.7 CPs selected in the A-HSE are less chemosensitive than those selected in the N-HSE	98
3.5 Discussion	102
3.6 Conclusions	105
Chapter 4	106
Generation of a molecular barcoding system to examine host systemic influences on heterogeneity in an immunocompetent model of breast cancer	106
4.1 Abstract	108
4.2 Introduction	109
4.3 Materials and Methods	111
4.3.1 Cell lines	111
4.3.2 Single cell cloning	111
4.3.3 HER2-CP pooling	112
4.3.4 Lentiviral infection	112
4.3.5 Genomic DNA preparations	112
4.3.6 Animal experiments	114
4.3.7 Polymerase chain reaction	114
4.3.8 Illumina sequencing library preparation	115
4.3.9 Next generation sequencing data analysis	115
4.3.10 Long-term proliferation kinetics assays	116
4.4 Results	117
4.4.1 Generation of a molecular barcoding system in an immunocompetent murine HER2 ⁺ breast cancer model system	117
4.4.2 Investigating the effects of host systemic activation in an immunocompetent murine breast cancer model	119
4.5 Discussion	122
4.6 Conclusions	125
Chapter 5	126
Accounting for tumor heterogeneity when using CRISPR-Cas9 for cancer progression and drug sensitivity studies	126

5.1 <i>Abstract</i>	128
5.2 <i>Introduction</i>	129
5.3 <i>Materials and Methods</i>	131
5.3.1 Cell lines	131
5.3.2 New gene editing protocol	131
5.3.3 Vector construction	132
5.3.4 Evaluating target site modification by Sanger sequencing	132
5.3.5 Animals and tumor studies	133
5.3.6 Chemotherapy studies	134
5.3.7 Osteopontin ELISAs and western blotting	135
5.3.8 Immunohistochemistry, immunofluorescence and microscopy	136
5.3.9 In vitro chemosensitivity studies	137
5.3.10 Statistical analyses	137
5.4 <i>Results</i>	138
5.4.1 Selection of Her2+ and Estrogen receptor-negative mammary carcinoma models	138
5.4.2 Heterogeneity between subclonal populations derived from McNeuA and Met-1	144
5.4.3 McNeuA and Met-1 derived clonal populations behave differently in vivo	146
5.4.4 Evidence that identification of proper controls is necessary for correct interpretation of experimental findings	151
5.4.5 Generating spp1 knockout clonal populations via CRISPR/Cas9	153
5.4.6 Osteopontin is dispensable for primary tumor growth	157
5.4.7 Loss of osteopontin reduces multifocal metastatic outgrowth	163
5.4.8 Loss of osteopontin enhances chemosensitivity	168
5.5 <i>Discussion</i>	172
Chapter 6	174
Discussion	174
6.1 <i>Summary of Findings</i>	175
6.2 <i>Discussion: Future directions and clinical implications</i>	178
6.3 <i>Concluding remarks</i>	183
References	184

Figures and Tables

Chapter 2

Figures

- Figure 2.1.** HMLER-HR CP barcodes can be detected using a Luminex-based detection system.
- Figure 2.2.** The PRISM system can detect Luminex barcodes from *in vivo* tumor samples with limited sensitivity.
- Figure 2.3.** Luminex DNA barcodes can be detected using Sanger sequencing.
- Figure 2.4.** Ligation-based library preparation methods can introduce error into multiplexed barcode libraries.
- Figure 2.5.** PCR-based multiplexed Illumina library preparation method can be used to accurately identify sequenced barcode-index pairs.
- Figure 2.6.** Luminex barcodes can be detected using next-generation sequencing.

Tables

- Table 2.1.** Barcodes present in HMLER[§].
- Table 2.2.** Barcode-index reverse (R) primer sequences.
- Table 2.3.** Illumina Library Preparation Primer Sets.

Chapter 3

Figures

- Figure 3.1.** HMLER clonal populations are functional heterogeneous.
- Figure 3.2.** HMLER[§] tumors recovered from the activated host systemic environment are more heterogeneous than those in the naïve host systemic environment.
- Figure 3.3.** Tumor growth kinetics in N-HSE and A-HSE.
- Figure 3.4.** Differential levels HMLER[§] intratumoral heterogeneity in N-HSE and A-HSE occurs independent of tumor mass.
- Figure 3.5.** Enhancement of HMLER[§] intratumoral heterogeneity in A-HSE is replicable and independent of barcode detection method.
- Figure 3.6.** HMLER[§] tumors in N-HSE and A-HSE have different patterns of innate immune infiltration.
- Figure 3.7.** A functional innate immune system is required for enhanced heterogeneity in A-HSE HMLER[§] tumors.

- Figure 3.8.** Cell intrinsic properties of individual CPs do not explain selection patterns observed *in vivo*.
- Figure 3.9.** HLA-I expression levels on individual CPs do not correlate with *in vivo* selection patterns.
- Figure 3.10.** CD47 expression levels on individual CPs do not correlate with *in vivo* selection patterns.
- Figure 3.11.** Hierarchical clustering of L1000 gene expression signatures of individual CPs.
- Figure 3.12.** HMLER[§] subpools exhibit unique patterns of cytokine and chemokine secretion.
- Figure 3.13.** HMLER[§] subpools have unique gene expression signatures despite containing common CPs.
- Figure 3.14.** N-HSE[§] subpool is more chemosensitive than A-HSE[§] subpool both *in vitro* and *in vivo*.

Chapter 4

Figures

- Figure 4.1.** Generation of a functionally heterogeneous collection of barcoded HER2⁺ clonal populations.
- Figure 4.2.** HER2-CPs for tumors with different incidence, growth kinetics, and levels of intratumoral heterogeneity in WT and MMTV-*neu* transgenic mouse strains.

Table

- Table 4.1.** Barcodes present in HER2-CP Pool.

Chapter 5

Figures

- Figure 5.1.** Phenotypic and functional heterogeneity of McNeuA and Met-1 breast cancer cells.
- Figure 5.2.** Met-1 and McNeuA Parental Tumor Characteristics.
- Figure 5.3.** Phenotypic heterogeneity of McNeuA and Met-1 subclonal populations.
- Figure 5.4.** MDA-MB-435 subclonal populations are heterogeneous.
- Figure 5.5.** McNeuA and Met-1 subclonal populations are functionally heterogeneous in tumor incidence, latency and growth kinetics.
- Figure 5.6.** Generation of appropriately matched wild-type and OPN knockout cell lines using CRISPR-Cas9 mediated gene editing.

- Figure 5.7.** Sanger sequencing of matched wild type and CRISPR-Cas9 OPN knockout cell lines.
- Figure 5.8.** OPN depletion does not affect primary tumor formation in murine models of HER2⁺ and ER⁻ breast cancer.
- Figure 5.9.** OPN depletion does not affect final primary tumor mass or spleen mass in murine models of HER2⁺ and ER⁻ breast cancer.
- Figure 5.10.** Matched wild type and knockout OPN cell lines can be used for pre-clinical metastasis studies.
- Figure 5.11.** OPN knockout results in reduced metastatic burden.
- Figure 5.12.** MT-2 OPN-KO derived tumors exhibit enhanced chemosensitivity *in vivo*.
- Figure 5.13.** Enhanced Chemosensitivity of OPN-depleted cell lines is not observed *in vitro*.

Chapter 6

Figure

- Figure 6.1.** The systemic environment can modulate intratumoral heterogeneity.

Personal Acknowledgements

I truly could not have completed the PhD process without the unwavering support and encouragement of all of the people that I interacted with professionally and personally. I owe such a debt of gratitude to everyone who mentored me, taught me, and cheered me on during both the good and bad times during these past 6 years. Thank you, thank you, thank you.

First, I owe so much to my mentor and thesis advisor, Dr. Sandra McAllister. You have taught me to trust myself and my abilities, and that persistence and perseverance can truly pay off. You provided both the professional and personal support that I needed to make it through this process and I am truly thankful for your mentorship and friendship.

Thank you to the members of the McAllister lab, past and present, for your scientific guidance, experimental assistance, and your friendship. I was so lucky to have spent the past 6 years with you as my peers.

Thank you to the individuals who have served on my dissertation advisory committee during my graduate career, Dr. Marsha Moses, Dr. David Frank, Dr. Stephanie Dougan, Dr. Glenn Dranoff, and Dr. Sridhar Ramaswamy. Your thoughtful advice and scientific guidance have been invaluable in helping to move my project forward and to achieve my professional goals.

Thank you to my family, particularly my mother, for your support, constant encouragement, and unconditional love. You have sacrificed so much to allow

me to reach my goals and it is impossible to put into words how much I appreciate that and how thankful I am. I love you all so very much.

Thank you to my dear friends for your love and encouragement. The Sisterhood, Alex, Jim, and my Harvard classmates, particularly Steph, Troy, and Mitch- you have all become my family and I could not have done this without you by my side.

Thank you to my husband, Andrew. I love you more than words can say and if one person got me through this experience, it was you. You have never stopped believing in me and you make me see that I can do the things that I doubt. You make me a better person and support me in every possible way. Thank you for being my person.

Finally, thank you to my daughter, Grace. You don't understand this yet, but you provided so much motivation and inspiration to see this process through. You arrived just when I needed you, and you actually were right there with me during many long nights in lab while I waited for you to get here. I love you, Roo.

Chapter 1

Introduction

1.1 Breast Cancer

1.1.1 Breast cancer statistics

Breast cancer is predicted to be the most frequent newly diagnosed cancer and second leading cause of cancer-related death among women in the United States in 2018 [1]. Improved screening methods and treatment options have led to an overall decrease in breast-cancer related deaths in the United States over time, however metastatic disease remains largely incurable, with a median survival time of only 2-3 years [2]. While only 6-10% of patients harbor detectable metastases at the time of their initial diagnosis, an estimated 30% of breast cancer patients will eventually experience recurrence and relapsed disease, at which point treatment options are palliative rather than curative [2, 3]. A better understanding of the biology underlying breast cancer progression and disease recurrence is necessary for the development of more effective treatments for metastatic disease.

1.1.2 Breast cancer subtype classification

Breast cancer is a heterogeneous disease that can be separated into subtypes [4]. Subtypes have traditionally been assigned based upon histopathological features and the immunophenotypic profile (i.e. protein expression patterns) of the primary tumor. Both the histopathological characterization and the expression levels of hormone receptors (HRs), specifically estrogen receptor (ER) and progesterone receptor (PR), as well as expression levels of the human epidermal growth factor receptor 2 (HER2), have

been shown to have prognostic value and are used to determine treatment regimens [4]. Recently, breast cancer classification schemes based upon gene expression patterns have been proposed, further refining the division of breast cancer into molecular subtypes (referred to as intrinsic subtypes) that differ in their patterns of disease recurrence and therapeutic response [5-8].

While the immunophenotypic and intrinsic subtype classifications do not entirely correspond to one another, the patterns that they reveal are largely overlapping and can be integrated to provide a more comprehensive prognostic profile [9]. The different subtypes show propensities to metastasize to particular locations, which can have an impact on clinical outcome [2]. In fact, median overall survival (OS), progression-free survival (PFS), and post-progression survival (PPS) rates all differ by subtype [2].

1.1.2.1 HR-positive breast cancer

Breast tumor HR status is typically evaluated using immunohistochemistry (IHC) to evaluate the expression levels of ER and/or PR [4]. If at least 1% of tumors cells stain positively for ER, then a tumor is considered to fall into the HR-positive (HR⁺) immunophenotypic subtype [4]. The HR⁺ classification can be subdivided based on HER2 expression levels, and HR⁺ tumors that also overexpress HER2 are frequently referred to as triple-positive (ER⁺/PR⁺/HER2⁺) [2]. HR⁺ tumors are more likely to metastasize to the bone than to visceral organs [2].

HR⁺/HER2⁻ tumors usually fall into one of two intrinsic subtypes: Luminal A or Luminal B [9]. Luminal A tumors typically have the best overall prognosis and are usually endocrine-therapy sensitive [2]. Luminal B tumors tend to be less endocrine-therapy sensitive, more proliferative, and have a worse prognosis than Luminal A tumors [2, 9]. Both Luminal A and Luminal B tumors are less chemosensitive than other intrinsic subtypes [9]. The majority of triple-positive tumors fall into either the Luminal B or HER2-enriched intrinsic subtypes [9].

1.1.2.2 *HER2-positive breast cancer*

HER2/*neu* encodes a transmembrane protein that is amplified in about 30% of human breast cancers [10]. HER2 status is characterized using IHC and/or fluorescence in situ hybridization (FISH) [4]. For a tumor to be classified as HER2-positive (HER2⁺), at least 30% of the tumor cells must display positive staining for membrane-associated HER2⁺ based on IHC or show evidence of genomic amplification of HER2 (a ratio of at least 2.2 copies of the *HER2* gene to its chromosome) from FISH [4]. The majority (88%) of HER2⁺ tumors fall into the HER2-enriched intrinsic subtype [2, 9].

The HER2⁺ subtype is associated with higher rates of metastasis to the central nervous system and liver [2]. Despite the initial success of HER2-targeted therapies, the majority of HER2⁺ breast cancer patients develop resistance against these therapies and experience disease recurrence, making effective therapies for HER2⁺ breast cancer an unmet clinical need.

1.1.2.3 Triple negative breast cancer

Triple negative breast cancer (TNBC) does not meet the positivity thresholds for HR or HER2-positivity. Patients diagnosed with TNBC are at the highest risk of early recurrence out of all breast cancer patients, and there are currently no curative treatments available for recurrent and metastatic disease [2, 11]. TNBC is associated with lung metastasis, but also has increased rates of metastasis to the central nervous system [2]. TNBC tumors are usually classified as either having basal-like or claudin-low intrinsic subtypes [9].

1.1.3 Current treatment options

Treatment recommendations for breast cancer differ based on tumor subtype, staging, pathology, and intrinsic subtype, among other features [12]. Treatment regimens frequently include both local (i.e. surgery and radiotherapy) and systemic (i.e. chemotherapy and targeted therapies) components [12]. Patients with HR⁺ disease almost always receive endocrine therapy (such as tamoxifen or aromatase inhibitors), and sometimes receive additional chemotherapy depending upon the tumor's intrinsic subtype classification and how advanced the disease is at diagnosis [12]. A combination of HER2-targeted therapies (such as Herceptin or lapatinib) and cytotoxic chemotherapy are frequently prescribed for HER2⁺ breast cancer [12]. Unlike the other two immunophenotypic subtypes, no targeted therapies are currently available for TNBC, so various chemotherapeutic regimens serve as the mainstays of treatment for this subtype [12].

1.2 Cancer cell dissemination, dormancy and metastatic outgrowth

Metastasis accounts for 90% of cancer related deaths and represents one of the least understood aspects of cancer pathogenesis [13, 14]. Intensive study of the process of metastatic spread has revealed that it is a multi-step process, frequently referred to as the invasion-metastasis cascade [14]. This process involves the local invasion and intravasation of tumor cells into the vasculature or lymphatic system, survival in circulation, extravasation into a distant tissue, the establishment of an amenable microenvironment, and adequate proliferation to transition from a micrometastatic colony to a life-threatening macrometastatic outgrowth [13, 14].

Numerous studies have demonstrated that the process of tumor cell dissemination commences in the early stages of primary tumor growth [15, 16]. Circulating tumor cells (CTCs) and disseminated tumor cells (DTCs) can be observed in the early stages of cancer progression in both preclinical models and in patients [15-18]. However, many of these DTCs lie dormant in distant tissues for extended periods of time. Micrometastatic outgrowths frequently do not transition into an active growth phase and reach a detectable size for months or years after diagnosis of the primary tumor [19]. Studies have revealed that DTCs are highly heterogeneous and that less than 1% of DTCs are capable of forming overt metastases [20-22]. It is not known what properties of individual DTCs make them more or less threatening than their counterparts and the forces that

trigger a transition from a state of dormancy to active proliferation are also poorly understood [20-22].

1.3 Cancer Heterogeneity

While breast cancer subtype classifications are useful, it is important to remember that they are not indicative of homogeneity and the sweeping characterization of a tumor based on histopathological or molecular features can be misleading. In the case of HER2 overexpression, only 30% of tumor cells analyzed must display high levels of membrane-associated HER2 expression for a tumor to be classified as HER2⁺ [4]. Even more striking, only 1% of the epithelial cells within a given tumor need to be ER-positive for the patient to be diagnosed with ER⁺ breast cancer [4]. What is overlooked by these classifications is a phenomenon referred to as intratumoral heterogeneity. Although tumors are believed to originate from a single mutant cell, many mutations are acquired over time, generating heterogeneous subpopulations of cells (or subclones) with different genetic backgrounds and functional characteristics [23, 24]. In a study of patient breast tumors, 77% of the tumors sampled exhibited intermediate to high levels of genomic heterogeneity [25]. Importantly, when serial samples were taken over time, previously minor subclonal populations become dominant following chemotherapy and metastases appeared to be derived from populations that were present in the primary tumor, demonstrating the important role that subclonal populations can play in disease progression [25].

Along with variations in genetic background, differences between the differentiation states and epigenetic modifications present in individual cells can cause additional intratumoral heterogeneity [26]. A recent study highlighted the importance of non-genetic sources of heterogeneity by using a clonal tracking system to demonstrate that subpopulations of colorectal cancer cells within tumors can exhibit markedly different behaviors without accompanying changes in copy number or single nucleotide variations [27]. Finally, cell extrinsic properties, such as interaction with the tumor microenvironment, can also contribute to heterogeneity [26]. Epithelial cells within a tumor are often exposed a microenvironment that is very different from that of normal tissue, such as direct contact of epithelial cells with fibroblasts, and to differential environmental cues directed at cells located in different areas of the tumor [26]. These microenvironmental abnormalities can lead to increased intratumoral heterogeneity and can promote cancer progression [28].

Intratumoral heterogeneity has implications for both tumor evolution and therapeutic efficacy. The clonal evolution model suggests that differences between tumor cell subpopulations provide variable fitness advantages and serve as substrates for evolutionary selection, causing particular subpopulations to dominate the tumor and dictate the clonal dynamics of a tumor at different points during tumor progression [24, 26, 29, 30]. Although differences in the mutational profile of subpopulations may be the best-documented parameter of tumor heterogeneity, it is ultimately the functional heterogeneity, a result of both genetic and non-genetic sources of heterogeneity, which drives the selection

process [27]. The effects of functional heterogeneity have been largely unexplored, resulting in a lack of understanding of the phenotypic properties that drive the selection process.

One accepted driving force of intratumoral selection is the differential proliferation rates of subclones. It has been hypothesized that proliferation rates dictate clonal dynamics, and that the most proliferative clones will dominate the tumor [31]. It isn't clear whether the selection of equivalently proliferative subclones is a driven or stochastic process, and which other phenotypic characteristics provide the greatest selective pressure [31]. This represents an important gap in our understanding because there is evidence that the fastest proliferating or dominant clones within a primary tumor may not comprise the most aggressive and threatening subpopulations. There are several studies that demonstrate discordance between primary tumors and metastases and provide evidence that metastases are derived from subclones present at low frequency in the primary tumor [32-34]. This suggests that during the course of disease progression there are alternative mechanisms that drive the selection of seemingly unthreatening subclones for reasons that are not currently understood. A better understanding of these mechanisms could aid in the identification of therapeutic targets that could prevent disease progression. New evidence also suggests that clonal cooperation within breast tumors may be an important driver of heterogeneity and may play a role in the selection process during tumor evolution [35, 36]. This presents a new potential mode of therapeutic targeting, as elimination of a clonal population that other subclones depend on for their

survival could both decrease overall heterogeneity and promote tumor regression.

Cancer therapeutics can serve as strong selective forces that drive the clonal evolution of a tumor, and the selective pressure applied by treatment is believed to contribute to the development of therapeutic resistance [37]. Patients often initially respond to targeted therapies, such as Herceptin for HER2⁺ breast cancer, but eventually develop resistance to the treatments, leading to disease recurrence and progression [37]. Resistance is believed result from the selection of subclones that are unresponsive to therapy, either due to a lack of targeting, mutations in target genes or mutations in genes that are able to bypass the therapeutic mechanism [37]. Therefore, heterogeneity presents a challenge to the success of targeted therapy. A better understanding of clonal dynamics could suggest combinatorial treatments that would prevent the emergence of resistance by simultaneously targeting several (or ideally all) threatening subclonal populations. Similar approaches have been used successfully in the treatment of other diseases in which treatment resistance is an issue, such as human immunodeficiency virus (HIV) infection [37].

1.4 Tumor Cell Non-Autonomous Influences

1.4.1 Tumor-stromal interactions

While the heterogeneity presented within the epithelial compartments of tumors already generates complicated and cooperative networks of cells, the

epithelial-stromal interactions within tumors add an additional layer of complexity to this system. In contrast to normal tissue architecture, in which stromal cells provide signals that help to maintain homeostasis, tumor-associated stroma often provides inappropriate growth signals and/or suppresses immune function that would prevent the outgrowth of incipient cancerous lesions [38]. Resident tissue stromal cells can be co-opted in response to abnormal signals produced by tumor cells. Once assuming a 'cancer-associated' phenotype, these stromal cells will frequently begin to assume aberrant signaling patterns themselves, driving a feed-forward loop that results in cancer progression [38]. On the other hand, some tumor-infiltrating stromal cells can effectively counter tumor development, through enacting a combination of tumor cell clearance and/or halting cell proliferation [39, 40]. While the complexities of these interactions make it so that each tumor ecosystem is unique, it is possible to identify unifying patterns of tumor-stromal cell interaction. For example, a recent study demonstrated that the spatial distribution of stromal cells within tumors is prognostic, and by using automated microenvironmental analyses in combination with epithelial cell characterization it is possible to improve survival predictions in ER⁻ breast cancer [41].

Breast cancers, and successful metastatic outgrowths, frequently contain a mixture of epithelial, fibroblast, endothelial, and immune cell populations. In fact, metastatic dormancy is often attributed to a lack of the required tumor-supportive cell populations outside of the primary tumor microenvironment [38]. While many tumor-supportive roles of microenvironmental populations have been

identified, the plasticity of stromal cell populations and their potential to assume anti-tumoral phenotypes make them attractive therapeutic targets [38]. Additionally, their relative genomic stability in comparison to tumor cells make them theoretically less susceptible to developing therapeutic resistance. Therefore, it is critical that we gain a more thorough understanding of tumor-stromal interactions and identify targetable signaling mechanisms that are potentially disruptive to tumor maintenance or progression.

1.4.2 The host systemic environment

Along with tissue resident stromal cells, distant reservoirs of cells can be triggered to adopt a tumor supportive phenotype [42, 43]. A number of elegantly designed studies have revealed ways in which the host systemic environment can be activated to generate microenvironments that allow for the emergence of progressively malignant phenotypes. Several forces that are capable of 'systemic activation' have been identified, including signals from the primary tumors, acute inflammatory processes such as wound healing, and secondary disorders that affect the immune system in a chronic fashion (both through chronic inflammation or by rendering the host immunocompromised) [44-51].

1.4.2.1 The tumor-induced systemic environment

Previous work has demonstrated that particular types of breast tumors are capable of activating the host systemic environment, leading to modulations of stromal cell composition and function in distant locations which promote

metastatic outgrowth [44-47, 52, 53]. This phenomenon has been observed in several preclinical breast cancer models and studies have uncovered mechanistic details of tumor driven systemic changes that culminate in enhanced metastatic burden.

One of the first examples of systemic promotion of metastasis was described in a model of triple negative breast cancer (TNBC), in which an aggressively growing BPLER tumor was shown to be capable of mobilizing functionally activated cells from the bone marrow [47]. These bone marrow cells (BMCs) infiltrated distant tumor cell growths and were capable of triggering the outgrowth of normally indolent tumor cells. The incorporation of these BMCs was associated with the formation of a desmoplastic stroma, in which cancer associated fibroblasts (CAFs) expressed high levels of alpha-smooth muscle actin (α -SMA). Genetic studies revealed that BPLER-secreted osteopontin was necessary, but not sufficient, to see these effects. Further experimentation demonstrated that the activated BMCs expressed high levels of the protein granulin, and that treatment with recombinant granulin was sufficient to induce the characteristic desmoplastic stroma in the distant tumors responding to the BPLER-driven host systemic modulation [45]. The properties of the activated host systemic environment, including high levels of plasma osteopontin and granulin expression in tumors, correlated with poor patient prognosis [45, 47]. An important observation from these studies was that not all aggressively growing tumors are capable of generating an activated host systemic environment, suggesting that risk stratification is possible [43].

A pre-clinical luminal breast cancer model of systemic activation utilizing the MCF7-Ras cell line revealed a distinct mechanism of macroenvironmental tumor promotion [46]. In this case, tumor secreted cytokines were taken up by platelets, which were able to travel to distant tumor cell outgrowths and provide signals that activated angiogenesis and aided in tumor progression. Mobilized bone marrow cells also infiltrated the distant tumor outgrowths, triggering an increase in CD24 expression on tumor cells, which helped to direct platelet chemotaxis.

Recent work using the genetically engineered mouse model (GEMM) *K14cre;Cdh1^{F/F};Trp53^{F/F}* (KEP) breast cancer model demonstrated that tumor-derived CCL2 was able to generate a cascade of immune cell modulations that promoted the outgrowth distant metastases [52, 53]. CCL2 caused macrophages to secrete interleukin (IL)-1 β , which in turn triggered gamma-delta T-cells to secrete IL-17. The IL-17 generated a systemic increase in granulocyte-colony stimulating factor (G-CSF) levels. The increased levels of systemic G-CSF resulted in systemic expansion of neutrophils and a functional polarization of the neutrophil population that allowed them to suppress the activity of CD-8⁺ cytotoxic T-cell populations. The CD-8⁺ T-cells normally constrain the growth of metastases, and the neutrophil-mediated suppression of this lymphocyte population resulted in an increased metastatic burden in the KEP primary tumor bearing mice.

Although these studies describe three unique mechanisms employed by primary tumors to activate the host systemic environment to promote distant

tumor cell growth, the fundamental approaches are quite similar. In all three cases, the primary tumor is capable of eliciting a functional change in a circulating immune cell population, which can then travel to distant organ locations and affect changes that support metastatic outgrowth. Together, these studies suggest that tumor-induced systemic host activation is capable of generating a growth permissive environment. It is reasonable to assume that such a growth permissive environment could allow for the outgrowth of immunogenic cancer cell subpopulations that would normally be cleared by the immune system, but this has not been demonstrated experimentally. If this hypothesis is correct, it could result in a systemically driven increase in intratumoral heterogeneity, and with it an increased risk for the development of therapeutic resistance and disease progression in “systemically activated” hosts.

1.5 Molecular Barcoding

Experimental techniques to identify clonal populations and track clonal dynamics have become increasingly quantitative and sensitive over the past fifty years. The majority of the early work employing clonal tracking techniques examined hematopoietic stem cells and patterns of hematopoiesis [54]. A variety of experimental methods have been employed including clonal identification via karyotypic analysis, heterozygosity of particular genes, and viral integration patterns [55-57]. These techniques allowed for the effective tracking of a small number of clonal populations, but were limited by their lack of sensitivity and their qualitative natures. The advent of molecular barcoding techniques, in which

short, non-coding DNA sequences are stably integrated into the genome of cellular populations of interest using viral infection, allows for the tracking of thousands of clonal populations simultaneously in a quantitative fashion [58-60].

DNA barcoding techniques have been used to successfully track clonal dynamics among heterogeneous tumor cell populations both *in vitro* and *in vivo* [61-68]. These techniques utilized barcode library infection methods, in which thousands of barcodes were introduced to a heterogeneous population of tumor cells simultaneously. This methodology allows for the tracking of a large number of clonal populations simultaneously, but it does not allow for the isolation of populations of interest from the library-infected pool for further study. This limitation makes it difficult to determine how and why particular patterns of heterogeneity are observed. Additionally, this method introduces the possibility of overestimations of heterogeneity, as individual cells from a single subpopulation could be infected with several barcodes. This could be particularly problematic if the various subclonal populations exhibit differential sensitivity to lentiviral infection.

DNA barcodes can theoretically be detected using any biological technique capable DNA-sequence specific binding or by using DNA sequencing. The DNA barcoding system employed in this thesis was developed in the Golub lab at the Broad Institute, and was designed for use with a Luminex-based detection system called PRISM [68]. The PRISM system detects the presence of particular DNA barcodes through complementary binding of anti-sense oligonucleotide sequences that are tethered to color coded beads that can be identified using a

Luminex FlexMap 3D detector [68]. Other potential methods of barcode detection include next-generation sequencing (NGS), fluorescence in situ hybridization (FISH), and quantitative polymerase chain reaction (qPCR) using DNA barcode sequence specific primers.

1.6 Summary

In this thesis, I describe the development of approaches that allowed for an investigation of systemic forces that can shape intratumoral heterogeneity. The first section focuses on the adaptation of the PRISM molecular barcode detection system to institute a workflow that allows for next-generation sequencing based detection of the DNA barcodes. I discuss the unique challenges posed by incorporating a multiplexing step into traditional ligation-based Illumina sequencing library preparation. I go on to describe an alternative protocol that can be used to successfully prepare multiplexed Illumina sequencing libraries that allow for sequencing-based detection of the PRISM barcodes. I utilize this barcoding system to demonstrate that BPLER tumor induced host systemic activation can result in significant enhancement of intratumoral heterogeneity in distant tumors. This enhancement of heterogeneity was accompanied by a decrease in innate immune cell infiltration compared to the less heterogeneous tumors recovered from a control cohort. We demonstrated that a functional innate immune system is required to observe systemically-mediated, differential patterns of intratumoral heterogeneity. We also showed that the clonal populations that emerged in the activated-host

systemic environment acted cooperatively to generate tumors with more malignant phenotypes, including reduced responsiveness to chemotherapy. These findings have implications for cancer patients that are subject to various types of systemic activation, such as primary tumors that secrete particular inflammatory cytokines, surgery, and secondary diseases that involve chronic inflammation or immunosuppression.

Additionally, I examined the ways in which functional heterogeneity can impact experimental design and described a novel gene editing protocol that appropriately controls for functional heterogeneity. The demonstration of how functional heterogeneity can impact the interpretation of results from studies that employ gene editing and can lead to false-positive or false-negative results represents an important observation with wide-ranging implications for studies utilizing gene editing technology.

Chapter 2

Development of a next-generation sequencing based barcode detection system

*Some of the material described in this chapter will be submitted as part of a manuscript to a peer-reviewed journal.

Acknowledgements

This study was designed by Jessica Olive, with supervision from Dr. Sandra McAllister. Dr. Channing Yu and Aristotle Mannan (Golub Lab, Broad Institute) provided the lentiviral barcode vectors and performed barcode composition analysis using the PRISM system. Dr. Zafira Castano and Dr. Jarom Chung generated the HMLER-HR-tdTomato barcoded cell lines. Tyler Laszewski assisted with *in vivo* experiments. Frances Greathouse provided experimental assistance. The Harvard Biopolymers Facility performed next-generation sequencing. Dr. Rory Kirchner performed next-generation sequencing data analysis. Jessica Olive performed all other experiments and data analysis.

2.1 Abstract

DNA barcoding represents a powerful clonal tracking tool that can be used to monitor large numbers of cellular populations in a highly sensitive fashion. The PRISM system is a Luminex-based DNA barcode detection system that can be used to track cellular responses and clonal dynamics in complex *in vitro* screens. Here I describe an adaptation of the PRISM system that allows for next-generation sequencing based Luminex-barcode detection and increased signal detection capabilities for DNA barcodes in *in vivo* samples. Our system utilizes multiplexing to sequence multiple samples per Illumina MiSeq lane, increasing its efficiency. We identify potential sources of error in ligation-based sequencing library preparation methods for multiplexed samples containing DNA barcodes and describe an alternate PCR-based library preparation protocol that resolves this issue. This represents a novel, highly adaptable DNA barcoding tool that uses widely available equipment that can be applied to resolve complicated biological questions.

2.2 Introduction

Clonal tracking techniques have been employed for several decades to track clonal dynamics in both normal and disease settings [55-57]. Much of the early work utilizing these methodologies involved cell fate mapping and detailing the process of hematopoiesis [54]. Refinements of clonal tracking methodologies, such as DNA barcoding, have provided more quantitative and sensitive clonal detection methods [58-62, 64, 65, 67]. One such technology is the Luminex-based PRISM system, which allows for the detection and quantification of up to 250 cellular populations, each of which contains a unique, stably integrated 24-base pair (bp) DNA barcode [68]. The PRISM system is high-throughput and adaptable, making it ideal for use in complex *in vitro* screens, such as massively parallel screens of drug sensitivity among hundreds of unique cancer cell lines [68].

Here we describe the generation of a collection of 30 single-cell derived clonal populations (CPs) from a human triple-negative breast cancer cell line, HMLER. Unique Luminex-barcodes intended for PRISM-based detection were stably integrated into each CP, and we demonstrated that PRISM could be used to accurately detect all 30 barcodes in CPs cultured *in vitro*. We also confirmed that the PRISM system could detect barcodes from *in vivo* samples, but with limited sensitivity.

We then developed of a protocol that allowed for the detection of Luminex barcodes using a next-generation sequencing based barcode detection system. This protocol allowed for the accurate and sensitive detection of all 30 Luminex barcodes, in both *in vitro* and *in vivo* samples, using Illumina sequencing technology, despite limited sequence diversity among the barcodes and their flanking regions. Our protocol allows

for the multiplexing of samples, increasing the efficiency and high-throughput nature of the system. Additionally, we describe a thresholding strategy that can be employed to differentiate between low-level false positive signals introduced by PCR and sequencer error from signal generated by true, low-frequency barcode variants.

2.3 Materials and Methods

2.3.1 Cell lines

HMLER-hygro-H-*ras*V12 (HMLER-HR) cells [47, 69] were cultured in advanced DMEM/F12 (Gibco) supplemented with 5% calf serum (CS, HyClone), 0.1% hydrocortisone (Sigma Aldrich), and 1% Penicillin Streptomycin (Gibco) at 37C with 5% carbon dioxide (CO₂).

293T cells were cultured in DMEM (Gibco) supplemented with 10% FBS (Gibco) and 1% Penicillin Streptomycin (Gibco) at 37C with 5% CO₂. All cell lines were confirmed to be mycoplasma negative.

2.3.2 Lentiviral infection

293T cells were transfected with 2.5 µg of lentiviral vector DNA (PLV-tdTomato was a generous gift from Dr. Robert Weinberg; barcode vectors were generous gifts from Todd Golub, Broad Institute, [68]), 2.5 µg PHR' (Addgene plasmid 8455), 1 µg VSVG (Addgene plasmid 8454) in Opti-MEM Reduced Serum Medium (Gibco) with Fugene HD (Promega). 48 and 72 hours following transfection, viral supernatants were collected and were filtered through a 40 micron syringe filter. Viral supernatants were stored at -80C and were mixed together prior to infection.

For lentiviral infection, HMLER-HR cells were infected with a 1:1 mixture of the appropriate viral supernatant in media with Polybrene (Sigma Aldrich). 72 hours after infection, isolation of successfully infected cells was performed either by FACS for tdTomato+ cells (for generation of the HMLER-HR-tdTomato cell lines) or by selecting

for blasticidin resistance (for lentiviral barcode infections; 5 µg/ml blasticidin S HCl (Invitrogen)).

2.3.3 Single cell cloning

HMLER-HR cells expressing tdTomato (HMLER-HR-tdTomato) were stained with antibodies against CD44 (APC-conjugated, BD Biosciences) and CD24 (FITC-conjugated, BD Biosciences) in PBS with 2% FBS for 30 minutes on ice. Single cells were determined to be tdTomato-positive and expression levels of CD44/CD24 were determined prior to sorting into single wells of a 96-well plate. Single cell clonal cell lines were expanded in culture.

2.3.4 CP pooling

Equal numbers of 30 CPs were mixed to form the CP Pool, referred to as HMLER[§] (**Table 2.1**). Aliquots with 500,000 HMLER[§] cells were frozen down to serve as the starting point for future experiments.

2.3.5 Genomic DNA preparations

Genomic DNA for barcode detection using the PRISM system was extracted using a Proteinase K/Tween-20/NP40 lysis buffer, as previously described [68]. Genomic DNA for barcode detection using next-generation sequencing was extracted using the QiaAmp DNA Mini Kit (Qiagen) and was eluted in 200 µl of water. Final DNA concentration was quantified using a Nanodrop 8000 Spectrophotometer (Thermo Fisher).

Table 2.1. Barcodes present in HMLER[§].

BC number	Barcode sequence
1	CTTTAATCTCAATCAATACAAATC
2	CTTTATCAATACATACTACAATCA
5	CAATTCAAATCACAATAATCAATC
7	CAATTCATTTACCAATTTACCAAT
8	AATCCTTTTACATTCACTTACTTAC
9	TAATCTTCTATATCAACATCTTAC
19	TCAATCAATTACTTACTCAAATAC
23	TTCAATCATTCAAATCTCAACTTT
26	TACTCAAATCTACACTTTTTTCA
28	CTACAAACAAACAAACATTATCAA
30	TTACCTTTATACCTTTCTTTTTAC
32	ATTATTCACTTCAAATAATCTAC
33	TCAATTACTTCACTTTAATCCTTT
38	TCAATCATTACACTTTTCAACAAT
42	CTATCTTCATATTTCACTATAAAC
44	TCATTTACCAATCTTTCTTTATAC
45	TCATTTCACAATTCAATTACTCAA
47	CTTCTCATTAECTTACTTCATAAT
48	AAACAACTTCACATCTCAATAAT
49	TCATCAATCTTTCAATTTACTTAC
50	CAATATACCAATATCATCATTTAC
53	TAATTATACATCTCATCTTCTACA
54	CTTTTTCAATCACTTTCAATTCAT
64	CTACATATTCAAATTACTACTTAC
66	TAACATTACAATACTATCTACTAC
67	TCATTTACTCAACAATTACAAATC
68	TCATAATCTCAACAATCTTTCTTT
70	ATACCAATAATCCAATTCATATCA
72	TCATTTACCTTTAATCCAATAATC
73	ATCAAATCTCATCAATTCAACAAT

2.3.6 Animal experiments

Experiments were performed in 6-8 week old female NCr nude mice (sp/sp, Taconic). All mouse cohorts received subcutaneous injections of 2×10^6 barcoded HMLER-HR-tdTomato cells suspended in 100 μ l of 20% matrigel (Corning). The naïve host systemic environment (N-HSE) cohort received a contralateral injection of 100 μ l of 20% matrigel (Corning). The TNBC environment cohort received a contralateral injection of 2×10^5 BPLER cells [70] suspended in 100 μ l of 20% matrigel (Corning). Tumors were measured using calipers once per week and tumor volume was calculated as $0.5 \times \text{length} \times \text{width}^2$.

Mice were euthanized via CO₂ inhalation. All mouse experiments were performed in accordance to federal laws and institutional guidelines and were approved by the Institutional Animal Care and Use Committee of Boston Children's Hospital and Brigham and Women's Hospital (Protocol 2017N000056).

2.3.7 Polymerase chain reaction

The barcode region of the lentiviral barcode vector was amplified using either primer set JO primer F/R (F: TGGAGCATGCGCTTTAGCAG; R: ATCGTTTCAGACCCACCTCC) or indexed primer sets (F: JH p05: ATC GTT TCA GAC CCA CCT CCC; R: JH p11-14 and JH p31-46, **Table 2.2**). PCR reaction mixtures contained 250 ng DNA, OneTaq 2x MasterMix (New England Biolabs), and 10 μ M each of F/R primers. The following PCR program was used to PCR amplify the template DNA: 94C for 30 seconds; repeat the following steps for 30 cycles: 94C for 20

Table 2.2. Barcode-index reverse (R) primer sequences.

Primer	Sequence (Reverse Complement)	Barcode-index #	Barcode Index Sequence
JH p11	TAGGTGTTTCGTCATTACTAACCGG	1	AACACCTA
JH p12	AGGCTGGACGTCATTACTAACCGG	2	TCCAGCCT
JH p13	GATGCAATCGTCATTACTAACCGG	3	ATTGCATC
JH p14	AGCTACGTCGTCATTACTAACCGG	4	ACGTAGCT
JH p31	CAGTTAGTCGTCATTACTAACCGG	5	ACTAACTG
JH p32	ATCTTAAGCGTCATTACTAACCGG	6	CTTAAGAT
JH p33	CTGTTTAAACGTCATTACTAACCGG	7	TTAAACAG
JH p34	CGAATTCACGTCATTACTAACCGG	8	TGAATTCC
JH p35	AATAGGATCGTCATTACTAACCGG	9	ATCCTATT
JH p36	TCCTATATCGTCATTACTAACCGG	10	ATATAGGA
JH p37	TAGCAACTCGTCATTACTAACCGG	11	AGTTGCTA
JH p38	ACTAGCTACGTCATTACTAACCGG	12	TAGCTAGT
JH p39	GTTAACTCCGTCATTACTAACCGG	13	GAGTTAAC
JH p40	GAATCTAGCGTCATTACTAACCGG	14	CTAGATTC
JH p41	GATTCGTACGTCATTACTAACCGG	15	TACGAATC
JH p42	GCAATCTTCGTCATTACTAACCGG	16	AAGATTGC
JH p43	ACGGTATACGTCATTACTAACCGG	17	TATACCGT
JH p44	TGTGACTACGTCATTACTAACCGG	18	TAGTCACA
JH p45	TCAGCATTTCGTCATTACTAACCGG	19	AATGCTGA
JH p46	ATAACGGTCGTCATTACTAACCGG	20	ACCGTTAT

seconds, 54C for 30 seconds, 68C for 20 seconds; final extension at 68C for 5 minutes). PCR products were purified using Agencort AMPure XP beads (Beckman Coulter) according to the manufacturer's protocol and purified DNA was eluted in 20-40 μ l water.

2.3.8 Illumina sequencing library preparation

Ligation-based Illumina library preparation was carried out by the Harvard Biopolymers Facility using an Integex Apollo 324 PrepX ILM kit using Kappa reagents, according to manufacturers' protocols. Ligation products were PCR amplified using primers against the P5/P7 Illumina adaptor regions.

For PCR-based Illumina library preparation, samples that had been amplified using one of the barcode-indexed primer sets were subject to a second PCR reaction using an Illumina indexed primer set with regions that were complementary to the barcode lentiviral vector regions (F: JO p50, R: JO p65-p88, **Table 2.3**). PCR reaction mixtures contained 100 ng DNA, OneTaq 2x MasterMix (New England Biolabs), and 10 μ M each of F/R primers. The following PCR program was used to PCR amplify the template DNA: 94C for 30 seconds; repeat the following steps for 15 cycles: 94C for 20 seconds, 54C for 30 seconds, 68C for 20 seconds; final extension at 68C for 5 minutes. PCR products were purified using Agencort AMPure XP beads (Beckman Coulter) according to the manufacturer's protocol and purified DNA was eluted in 20-40 μ l water.

Table 2.3. Illumina Library Preparation Primer Sets.

Primer	TruSeq Index	Primer Sequence
JO p50	N/A	AATGATACGGCGACCACCGAGATCTACACTCTTTCCCTACA CGACGCTCTTCCGATCTGACGGTATCGATAACTGCAG
JO p65	(1) CGTGAT	CAAGCAGAAGACGGCATAACGAGATCGTGATGTGACTGGAG TTCAGACGTGTGCTCTTCCGATCTCGTCATTAATAACCGG
JO p66	(2) ACATCG	CAAGCAGAAGACGGCATAACGAGATACATCGGTGACTGGAG TTCAGACGTGTGCTCTTCCGATCTCGTCATTAATAACCGG
JO p67	(3) GCCTAA	CAAGCAGAAGACGGCATAACGAGATGCCTAAGTGACTGGAG TTCAGACGTGTGCTCTTCCGATCTCGTCATTAATAACCGG
JO p68	(4) TGGTCA	CAAGCAGAAGACGGCATAACGAGATTGGTCAGTGACTGGAG TTCAGACGTGTGCTCTTCCGATCTCGTCATTAATAACCGG
JO p69	(5) CACTGT	CAAGCAGAAGACGGCATAACGAGATCACTGTGTGACTGGAG TTCAGACGTGTGCTCTTCCGATCTCGTCATTAATAACCGG
JO p70	(6) ATTGGC	CAAGCAGAAGACGGCATAACGAGATATTGGCGTGACTGGAG TTCAGACGTGTGCTCTTCCGATCTCGTCATTAATAACCGG
JO p71	(7) GATCTG	CAAGCAGAAGACGGCATAACGAGATGATCTGGTGACTGGAG TTCAGACGTGTGCTCTTCCGATCTCGTCATTAATAACCGG
JO p72	(8) TCAAGT	CAAGCAGAAGACGGCATAACGAGATTCAAGTGTGACTGGAGT TCAGACGTGTGCTCTTCCGATCTCGTCATTAATAACCGG
JO p73	(9) CTGATC	CAAGCAGAAGACGGCATAACGAGATCTGATCGTGACTGGAG TTCAGACGTGTGCTCTTCCGATCTCGTCATTAATAACCGG
JO p74	(10) AAGCTA	CAAGCAGAAGACGGCATAACGAGATAAGCTAGTGACTGGAG TTCAGACGTGTGCTCTTCCGATCTCGTCATTAATAACCGG
JO p75	(11) GTAGCC	CAAGCAGAAGACGGCATAACGAGATGTAGCCGTGACTGGAG TTCAGACGTGTGCTCTTCCGATCTCGTCATTAATAACCGG
JO p76	(12) TACAAG	CAAGCAGAAGACGGCATAACGAGATTACAAGGTGACTGGAG TTCAGACGTGTGCTCTTCCGATCTCGTCATTAATAACCGG
JO p77	(13) TTGACT	CAAGCAGAAGACGGCATAACGAGATTTGACTGTGACTGGAGT TCAGACGTGTGCTCTTCCGATCTCGTCATTAATAACCGG
JO p78	(14) GGAACT	CAAGCAGAAGACGGCATAACGAGATGGAAGTGTGACTGGAG TTCAGACGTGTGCTCTTCCGATCTCGTCATTAATAACCGG
JO p79	(15) TGACAT	CAAGCAGAAGACGGCATAACGAGATTGACATGTGACTGGAGT TCAGACGTGTGCTCTTCCGATCTCGTCATTAATAACCGG
JO p80	(16) GGACGG	CAAGCAGAAGACGGCATAACGAGATGGACGGGTGACTGGAG TTCAGACGTGTGCTCTTCCGATCTCGTCATTAATAACCGG
JO p81	(18) GCGGAC	CAAGCAGAAGACGGCATAACGAGATGCGGACGTGACTGGAG TTCAGACGTGTGCTCTTCCGATCTCGTCATTAATAACCGG
JO p82	(19) TTTCAC	CAAGCAGAAGACGGCATAACGAGATTTTCACGTGACTGGAGT TCAGACGTGTGCTCTTCCGATCTCGTCATTAATAACCGG

Table 2.3 (Continued). Illumina Library Preparation Primer Sets.

JO p83	(20) GGCCA C	CAAGCAGAAGACGGGCATACGAGATGGCCACGTGACTGGA GTTTCAGACGTGTGCTCTTCCGATCTCGTCATTACTAACCGG
JO p84	(21) CGAAAC	CAAGCAGAAGACGGGCATACGAGATCGAAACGTGACTGGAG TTCAGACGTGTGCTCTTCCGATCTCGTCATTACTAACCGG
JO p85	(22) CGTACG	CAAGCAGAAGACGGGCATACGAGATCGTACGGTGACTGGAG TTCAGACGTGTGCTCTTCCGATCTCGTCATTACTAACCGG
JO p86	(23) CCACTC	CAAGCAGAAGACGGGCATACGAGATCCACTCGTGACTGGAG TTCAGACGTGTGCTCTTCCGATCTCGTCATTACTAACCGG
JO p87	(25) ATCAGT	CAAGCAGAAGACGGGCATACGAGATATCAGTGTGACTGGAG TTCAGACGTGTGCTCTTCCGATCTCGTCATTACTAACCGG
JO p88	(27) AGGAAT	CAAGCAGAAGACGGGCATACGAGATAGGAATGTGACTGGAG TTCAGACGTGTGCTCTTCCGATCTCGTCATTACTAACCGG

2.3.9 Next generation sequencing data analysis

Next-generation sequencing data analysis was analyzed by Dr. Rory Kirchner by identifying index and barcodes in each read by searching for the pattern [8 base index]-[17 bases]-ACGCGT-[24 base barcode]-CTGCAG and counting the index-barcode pairs.

2.4 Results

2.4.1 Generation HMLER clonal cell lines with stably integrated DNA barcodes that are detectable by the PRISM system

Single cell-derived clonal populations (CPs) were derived from the HMLER-hygro-H-*ras*V12 (HMLER-HR) cell line, a transformed mammary epithelial cell line, which had been stably infected to express the fluorescent protein tdTomato [47, 69]. To do so, we sorted single cells based on their CD24/44 profiles as an arbitrary way to capture heterogeneity, and expanded these to establish the CPs (**Figure 2.1A**). Thirty individual CPs were infected with unique lentiviral barcoding vectors developed for use with the Luminex-based PRISM detection system [68]. Each barcode consists of a heritable 24-base pair Luminex DNA barcode sequence that can be PCR amplified from genomic DNA preparations using a common barcode flanking sequence (**Figure 2.1B, Table 2.1**).

We evaluated the ability of the PRISM system to accurately detect the barcodes from the 30 CPs by mixing equal numbers of each barcoded cell line, extracting genomic DNA from this mixture, and submitting it to our collaborators at the Broad Institute for PRISM barcode analysis, as previously described [68]. Briefly, barcode DNA is PCR-amplified using a single primer set (including one biotinylated primer) and is incubated with Luminex microsphere-conjugated oligonucleotides that are anti-sense to the barcode sequences and phycoerythrin-streptavidin (**Figure 2.1C**). A Luminex detector is used to analyze barcode composition, with the Luminex microsphere color indicating barcode identity and the phycoerythrin intensity giving a relative

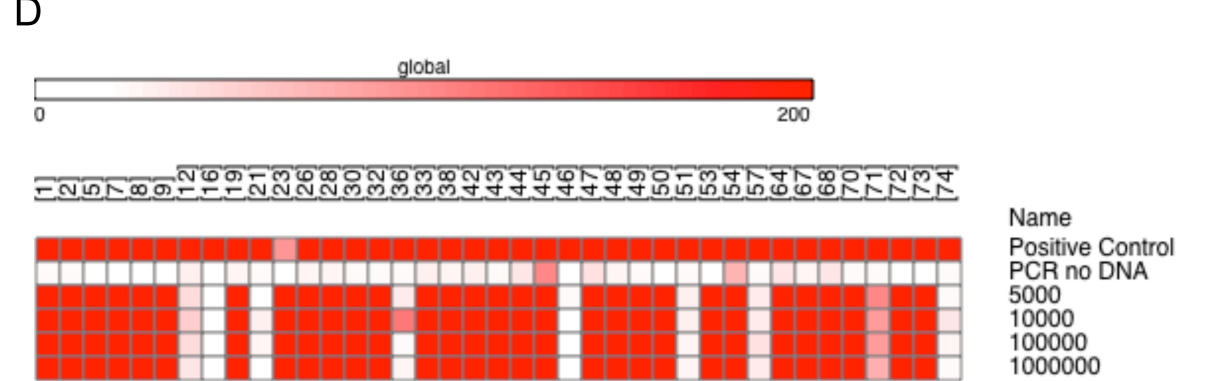
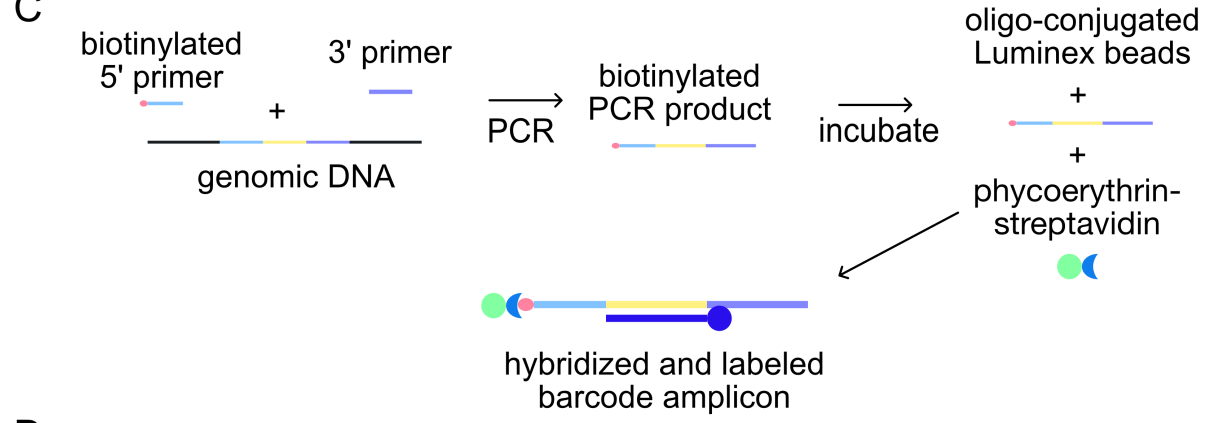
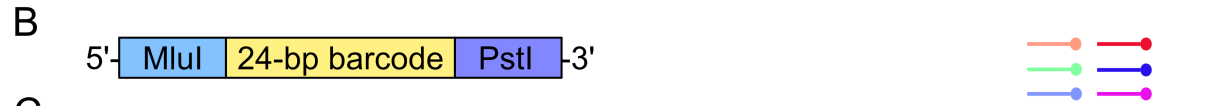
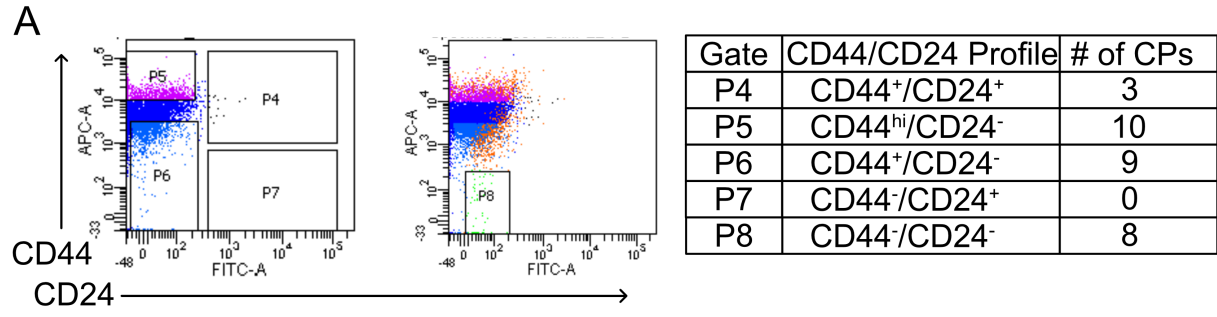


Figure 2.1. HMLER-HR CP barcodes can be detected using a Luminex-based detection system. (A) Gating strategy for FACS sorting of single HMLER-HR cells based on CD44/CD24 staining and summary of original CD44/CD24 profiles of the 30 barcoded CPs. (B) 24-bp Luminex DNA barcodes have common flanking regions, with a MluI restriction site 5' to the barcode and a PstI restriction site on the 3' end. (C) Genomic DNA is extracted from barcoded cell lines and is PCR amplified against the common flanking regions, including use of a 5' biotinylated primer. Biotinylated barcode amplicons are incubated with oligonucleotide-conjugated Luminex beads that are antisense to the Luminex barcode sequences and phycoerythrin-streptavidin, generating hybridized and labeled barcode amplicons. A Luminex FlexMap machine is used to deconvolute barcode identity and clonal abundance. (D) The PRISM system accurately identifies barcodes in a pool of cultured HMLER-HR barcoded CPs. The total number of cells that DNA was extracted from is indicated to the right of the heat map.

measure of barcode abundance (**Figure 2.1C**).

Our collaborators were blinded to the identities of the barcodes that had been introduced into our CPs, and were able to accurately identify all 30 barcodes that were present in our sample (**Figure 2.1D**). Several Luminex beads specific for barcodes that were not present in our sample generated some low level signal, but overall these results suggested that the PRISM barcode detection system was able to accurately identify our barcoded CPs.

2.4.2 The PRISM system generates lower barcode detection signals from *in vivo* samples than *in vitro* samples

We next evaluated whether the PRISM system could detect the barcoded CPs in DNA extracted from *in vivo* tumor samples. An equal number of each of the 30 barcoded CPs was mixed to generate a clonal population pool, referred to as HMLER[§]. HMLER[§] cells were injected subcutaneously into nude mice, contralateral to either a matrigel control (naïve host systemic environment, N-HSE) or an aggressively growing TNBC tumor (activated host systemic environment, A-HSE) (**Figure 2.2A**). Genomic DNA was extracted from the HMLER[§] cells at Day 0, to serve as an input control. Tumors were allowed to grow for 90 days. A total of 6 HMLER[§] tumors were recovered, with masses ranging from 1 mg – 891 mg. Larger tumors were divided into several pieces to allow for a sampling of regional heterogeneity, and bulk genomic DNA was extracted from each tumor section. PRISM barcode analysis was able to detect signal from all recovered tumors, however the average total read count for *in vivo* samples was ~20 fold lower than the *in vitro* Day 0 input control (**Figure 2.2B**). Average total

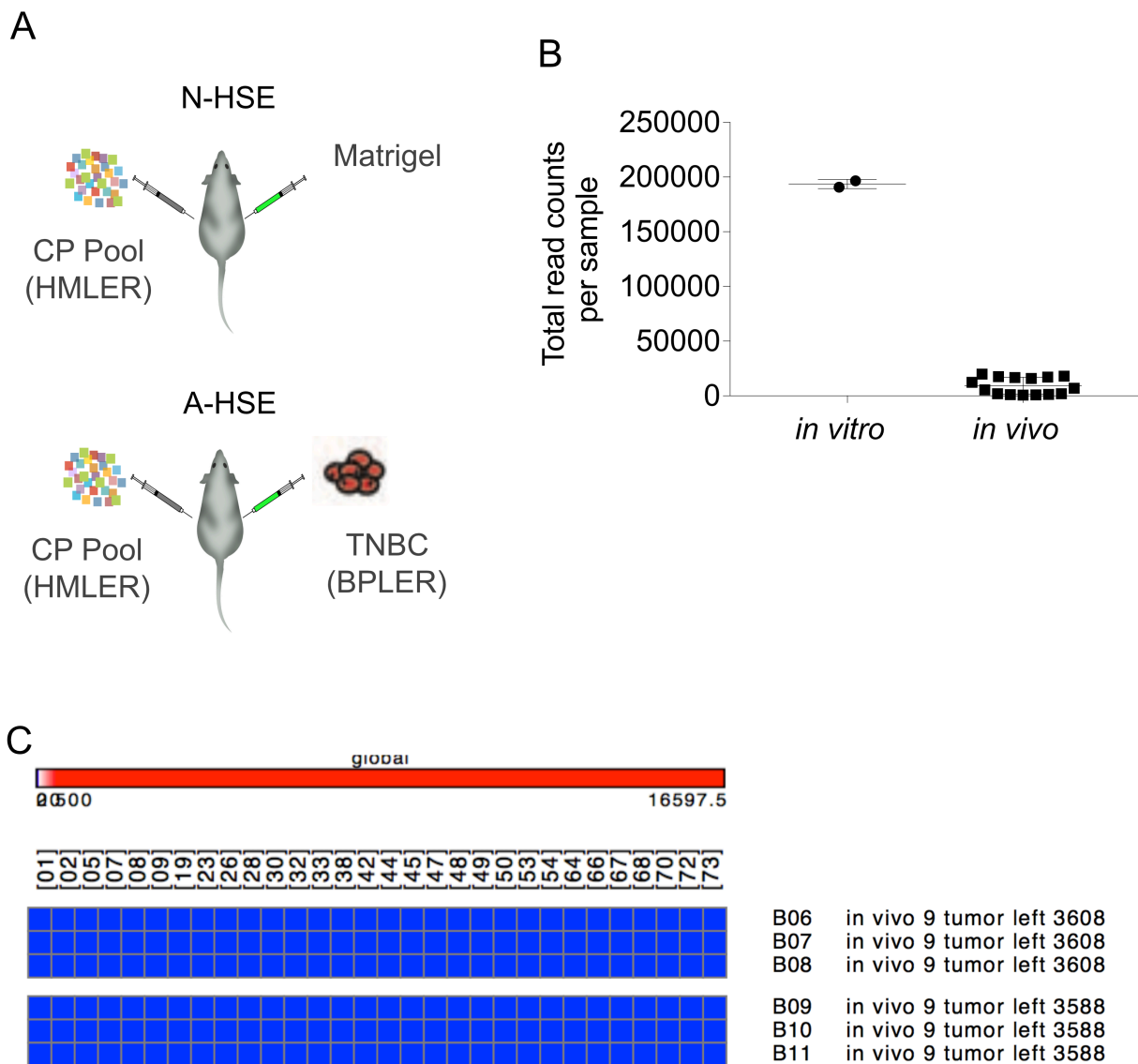


Figure 2.2. The PRISM system can detect Luminex barcodes from *in vivo* tumor samples with limited sensitivity. (A) Nude mice received subcutaneous injections of HMLER^S cells contralateral to either Matrigel or the BPLER cell line. Genomic DNA was extracted from recovered HMLER^S tumors and PRISM barcode composition analysis was performed. **(B)** Total read counts per sample generated by PRISM for either the *in vitro* input control samples or HMLER^S tumor sections. **(C)** Representative heat map depicting barcode read counts in cases where PRISM was unable to detect barcodes from *in vivo* tumor samples. Blue > Red represents Low > High read counts.

read counts were similar for every tumor, and did not correlate with final tumor mass, suggesting that this phenomenon was likely attributable to a reduced PRISM detection sensitivity for *in vivo* samples.

More concerning than the signal differential that we observed in different sample types was that we submitted gDNA from several consecutive *in vivo* experiments for which the Luminex barcode detection system was unable to detect any barcodes (**Figure 2.2C**). The research question that I was interested in addressing (namely, how does the host systemic environment influence breast cancer intratumoral heterogeneity) required extensive *in vivo* experimentation; therefore, it was desirable to develop an alternative barcode detection method that had enhanced sensitivity for *in vivo* samples. Additionally, access to a Luminex FlexMap machine was a rate-limiting step in my experimental workflow and it was preferable to transition to a detection method that could utilize more readily available technology. These two factors motivated me to develop a next-generation sequencing based detection method for the Luminex DNA barcodes.

2.4.3 Luminex barcodes can be detected using Sanger sequencing

The Luminex barcodes were not designed with sequencing in mind, so several of their design properties posed potential challenges for sequencing-based barcode detection. First, the barcodes themselves have low sequence diversity, as they contain no guanine (G) nucleotides (**Table 2.1**). Additionally, the barcodes are flanked by common sequences, so PCR-amplified barcode amplicons all begin with identical nucleotide sequence. Low sequence diversity is known to cause issues during next-

generation sequencing with the Illumina platform due to the mechanics of the algorithm that assigns DNA template locations within the sequencer flow-cell [71]. While there are strategies available to overcome this issue, it was not a given that we would be able to successfully detect the PRISM barcodes using a sequencing-based detection method.

We first sought to confirm that we could detect the correct barcode from each individual CP using Sanger sequencing. Sanger sequencing tends to produce low quality reads towards each end of the amplicon, so I designed new primers against the lentiviral barcode vector that were further upstream and downstream than those used for PCR amplification prior to Luminex-based barcode detection (**Figure 2.3A**).

Additionally, I transitioned to a Qiagen kit based DNA extraction method (Qiagen QiaAmp DNA Mini Kit) that yielded DNA samples that were less prone to degradation than the Proteinase K/Tween-20/NP40 based extraction that the PRISM system employs, and therefore could be PCR amplified more efficiently (**Figure 2.3B**). Using this optimized DNA extraction and PCR amplification protocol, I validated that all 30 unique Luminex barcodes could be amplified and detected using Sanger-sequencing (**Figure 2.3C**). This suggested that the Luminex barcodes were amenable to sequencing-based detection methods.

2.4.5 PCR-based methods are more suitable for multiplexed Illumina library preparation than low efficiency ligation based methodology

In order to maximize the number of samples that we could sequence per Illumina sequencer lane, we chose to use multiple levels of multiplexing within our Illumina

A ##

```

      >JO primer R                                >PRISM R
ATCGTTTCAGACCCACTCCcaaccgccgggggaccgccagggcccgaaggaatagaagaagtgaggagagagacagagacagatccattcgatta < 100
I V S D P P P N P E G T R Q A R R N R R R R W R E R Q R Q I H S I S
S F Q P T H L P T P R G P D R P E G I E E E G G E R D R D R S I R L
R F R P T S Q P R G D P T G P K E * K K K V E R E T E T D P F D *
TAGCAAAGTCTGGGTGGAGGgttggggctcccctgggctgtccgggtctcttctctcttctccacctctctctctgtctctgtctaggttaagctaat
      10      20      30      40      50      60      70      80      90

      >PstI      >MluI      >PRISM F
gtgaacggatctcgcagctatcgatataaCTGCAGACCGGTaccggttagtaatgacgatggttaacctaccgggtaggggaggcgcttttccaaggcagt < 200
E R I S T V S I * L Q T R T G * * R W Y L P G R G G A F P K A V
V N G S R R Y R Y N C B R V P V S N D D G T Y R V G E A L F P P Q S
* T D L D G I D I T A D A Y R L V M T M V P T G * G R R F S Q G S
caccttgctagagctgccatagctatatTGCCTCCGCATggccaatcattactgtaccatggatggccatcccctccggaaaagggttcgctca
      110      120      130      140      150      160      170      180      190

      >JO primer F
cTGGAGCATCGCTTAGCAGccccgctggggcacttggcgctacacaagtgccctctggcctcgcaacattccacatccaccggtagggcgaaccggc < 300
W S M R F S S P A G H L A L H K W P L A S H T F H I H R * A P T G
G A C A L A A P L G T W R Y F S G L W P R T H S T S T G R R Q P A
L E H A L * Q P R W A L G A T Q V A S G L A H I P H P P V G A N R L
gACCTCGTACGCGAAATCCTCggggcgaccctgaaccggatgttccaccggagaccggagcgtgtgtaaggtgtaggtggccatcccggttggccg
      210      220      230      240      250      260      270      280      290

```

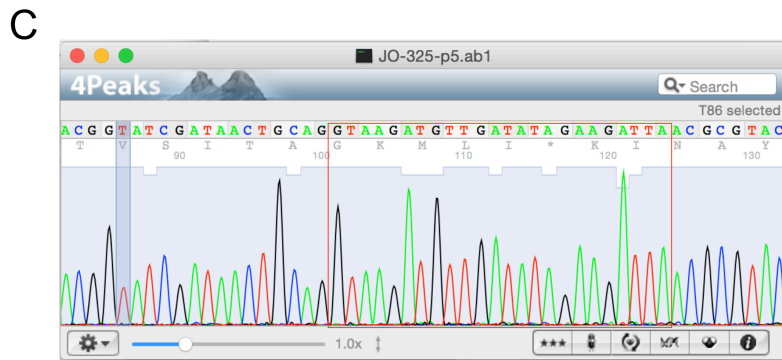
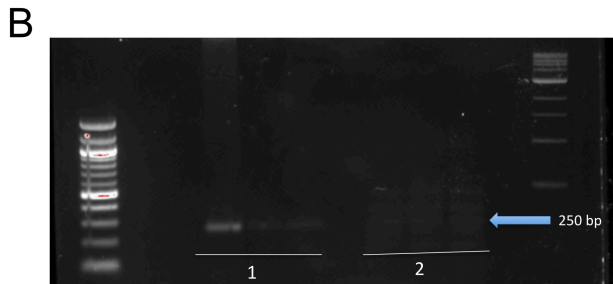


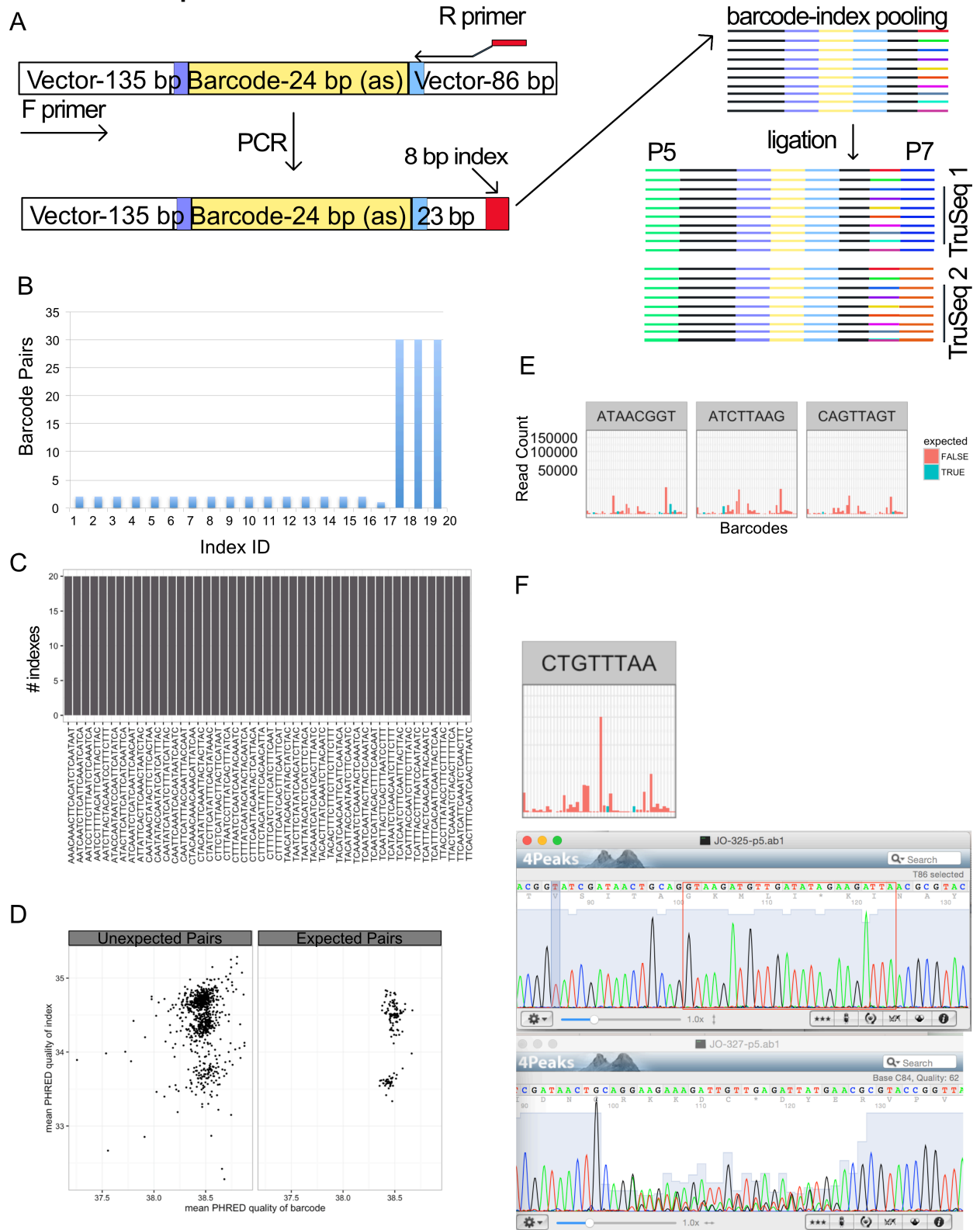
Figure 2.3. Luminex DNA barcodes can be detected using Sanger sequencing. (A) New primers (JO primer F and JO primer R) were designed further upstream and downstream of the barcode region (barcodes were inserted between PstI/MluI restriction sites) to use for PCR amplification prior to Sanger sequencing. (B) Agarose gel comparing PCR product yields from PCR reactions using gDNA input extracted using a Qiagen kit (designated as 1; lanes contained reactions with DNA input of 500 ng, 250 ng, and 100 ng, respectively) or the PRISM gDNA extraction method (designated as 2; lanes contained reactions with DNA input of 500 ng, 250 ng, and 100 ng, respectively). Expected amplicon size is ~250 bp (blue arrow). (C) Representative chromatogram from Sanger sequencing results of a Luminex barcode amplicon (barcode region is boxed in red).

library preparation strategy. Twenty-four uniquely indexed Illumina adaptors are commercially available, allowing for the pooling of up to 24 samples within a single sequencing lane. Systems that allow for further multiplexing through addition of a second index during PCR amplification have been previously described [72]. We chose to introduce a second PCR step into our library preparation work-flow during which one of 20 unique indexes would be added to the 3' end of the barcode amplicon (**Figure 2.4A, Table 2.2**). Following PCR purification of the indexed barcode amplicons, pooling of equal molar amounts of each amplicon is performed (barcode-index pooling, **Figure 2.4A**). Each barcode-index pool is then inserted into an indexed Illumina adaptor via a ligation reaction. Up to 24 unique barcode-index pools can be paired with the indexed Illumina adaptors, thereby allowing for the sequencing and deconvolution of up to 480 unique samples (20 barcode-index pairs x 24 indexed Illumina adaptors) in a single sequencing lane (**Figure 2.4A**). Identification of the barcodes present within each sample requires deconvolution by: first, isolating all barcode reads associated with a single Illumina index; and second, isolating all barcode reads within a single Illumina index that are associated with the specific barcode-index that is associated with that sample.

I began by testing each indexed primer for its ability to successfully amplify the barcode region of gDNA extracted from barcoded CPs, and then using Sanger sequencing to verify that the index had been incorporated. I confirmed that all 20 indexes could be added to the 3' end of barcode amplicons using PCR. I then designed an experiment to test whether our library preparation method could be used to accurately detect and deconvolute known barcode-index pairs that had been ligated into

Figure 2.4. Ligation-based library preparation methods can introduce error into multiplexed barcode libraries. **(A)** Multi-level multiplexing is achieved by attaching 1 of 20 unique barcode-indexes to the 3' end of each sample. Up to 20 indexed samples can be pooled into a single barcode-index library. Each barcode-index library can be ligated into 1 of 24 uniquely indexed Illumina adaptors. Purple region represents PstI, light blue represents MluI. **(B)** Expected number of barcodes within each barcode-index pairing. **(C)** Actual number of indexes (vertical axis) found to be associated with each barcode (horizontal axis) with the barcode-index pairs upon deconvolution of sequencing data. **(D)** The spread for the mean PHRED scores of the index sequence reads versus the barcode sequence reads is similar among unexpected and expected barcode-index pairings. **(E)** Representative sample of summary graphs showing the read counts per barcode paired with individual indexes. Each summary graph represents a unique index. Barcodes that were expected to be paired with that index are shown in green and barcodes that were not expected to be paired with that index are shown in red. **(F)** Next-generation sequencing data suggested that the index CTGTTAA was paired with all 30 barcode sequences and that the most abundant barcode associated with this index represented an unexpected pairing (top panel). However, Sanger sequencing of the indexed sample that was entered into the barcode-index pool revealed a clear and clean signal for the single expected barcode (middle panel, barcode sequence boxed in red). A representative chromatogram for a barcode amplicon that contained multiple barcodes (HMLER[§], 30 barcodes) is also shown (bottom panel).

Figure 2.4 (Continued). Ligation-based library preparation methods can introduce error into multiplexed barcode libraries.



indexed Illumina adaptors. For this test run, I used PCR to pair each of 17 indexes with 2 different barcode sequences to generate 17 barcode-index pools (**Table 2.2**). I used input DNA from single CPs, so that a single known DNA barcode would be present in each sample. Additionally, I indexed DNA samples from HMLER^S (which contains 30 DNA barcodes) with 3 separate indexes to interrogate a situation where a larger number of barcodes are associated with each index (**Table 2.1**). I then submitted these 20 samples to the Harvard Biopolymers facility (BPF) for Illumina library preparation. The BPF was directed to use an Illumina kit to ligate each of the 20 barcode-index pools into a uniquely indexed Illumina adaptor. These adaptors have identical P5 regions, and their P7 regions each contain a unique TruSeq Index. These 20 multiplexed samples were then mixed and run on a single lane of an Illumina MiSeq sequencer. In order to help to adjust for the low sequence diversity present in the sample, 40% PhiX was spiked into the sequencing reaction to increase the sample diversity [71].

The expected result was that we would see 17 indexes that were each associated with 2 DNA barcodes and 3 indexes that were each associated with 30 DNA barcodes (**Figure 2.4B**). However, after deconvolution of the sequencing data, we found that every index was associated with every barcode present (**Figure 2.4C**). The quality of these unexpected barcode-index sequence reads was high, with PHRED scores comparable to the expected combinations, suggesting that these reads were ‘real’ and not due to sequencer error (**Figure 2.4D**). Additionally the number of reads for unexpected barcode-index pairs was as high or higher than the expected combinations in many cases, providing further evidence that this result was not due to sequencer noise (**Figure 2.4E**). Our initial hypothesis was that PCR contamination was to blame.

However, Sanger sequencing of the individual barcode-index PCR products that were submitted to the BPF revealed that a single barcode was present in each case evaluated, rather than the mixture of barcodes that would be observed if DNA barcode cross contamination had occurred during PCR (**Figure 2.4F**).

Further discussions with the BPF revealed that due to low ligation efficiency during the library preparation, they had PCR amplified the ligation products using primers against the Illumina P5/P7 adaptor sequences. During this PCR step every barcode and every index were present in single reaction mixture, providing an opportunity for recombination to occur, generating the unexpected DNA barcode-index hybrids that we observed during the Illumina sequencing run [73].

An alternative to ligation-based Illumina library preparation methods is to attach the Illumina adaptor regions to the amplicons being sequenced using PCR-based methods. To pursue this method, we designed a single forward PCR primer with complementarity to the barcode vector and 20 reverse primers that each contained a unique Illumina TruSeq index (**Table 2.3**). In our pilot attempt to prepare the Illumina libraries using PCR, we did not pursue the second level of multiplexing. The barcode-indexes that we designed were located at the 3' terminus of the barcode amplicons, and maintenance of the indexes during the second PCR step would have required unique R primers for each barcode-index/Illumina index combination (**Table 2.2**). The primers are ~80 bp and expensive to synthesize, and a cost-benefit analysis revealed that for the number of samples that we planned to analyze it would have been more expensive to synthesize the unique R primers than to run multiple sequencing lanes. However, the

system is amenable to further multiplexing by using R primers specific for the barcode-index tags.

We generated a test library that contained five DNA samples from individual CPs in order to evaluate whether this method allowed for the correct identification of the expected barcode-Illumina index pairs. The PCR reactions for each primer set were highly specific and efficient, generating a single strong band of the expected length (**Figure 2.5A**). Additionally, we Sanger sequenced the amplicons and verified that they contained the expected barcode/Illumina index pairings, and that there was no suggestion of multiple barcodes being present. This library was successfully sequenced on an Illumina MiSeq sequencer, demonstrating that our PCR-based library preparation method was effective. Importantly, the expected barcode-Illumina index pairs generated signal that was ~233-2,500-fold higher than the highest false positive signal, allowing for simple thresholding of true signal from background sequencer noise (**Figure 2.5B**).

Together, this data demonstrated that the Luminex-barcodes were amenable to next-generation sequencing based detection.

2.4.6 PRISM barcodes extracted from both *in vitro* and *in vivo* samples can be accurately detected using Illumina next-generation sequencing technology

We next sought to determine whether we could reliably detect DNA barcodes extracted from *in vivo* tumor samples using next-generation sequencing. To do this, we sequenced barcode amplicons that had been prepared from gDNA extracted from tumors that had formed following injection of HMLER^S cells (**Figure 2.2A**). Our *in vivo* PRISM data suggested that there is selective pressure against many

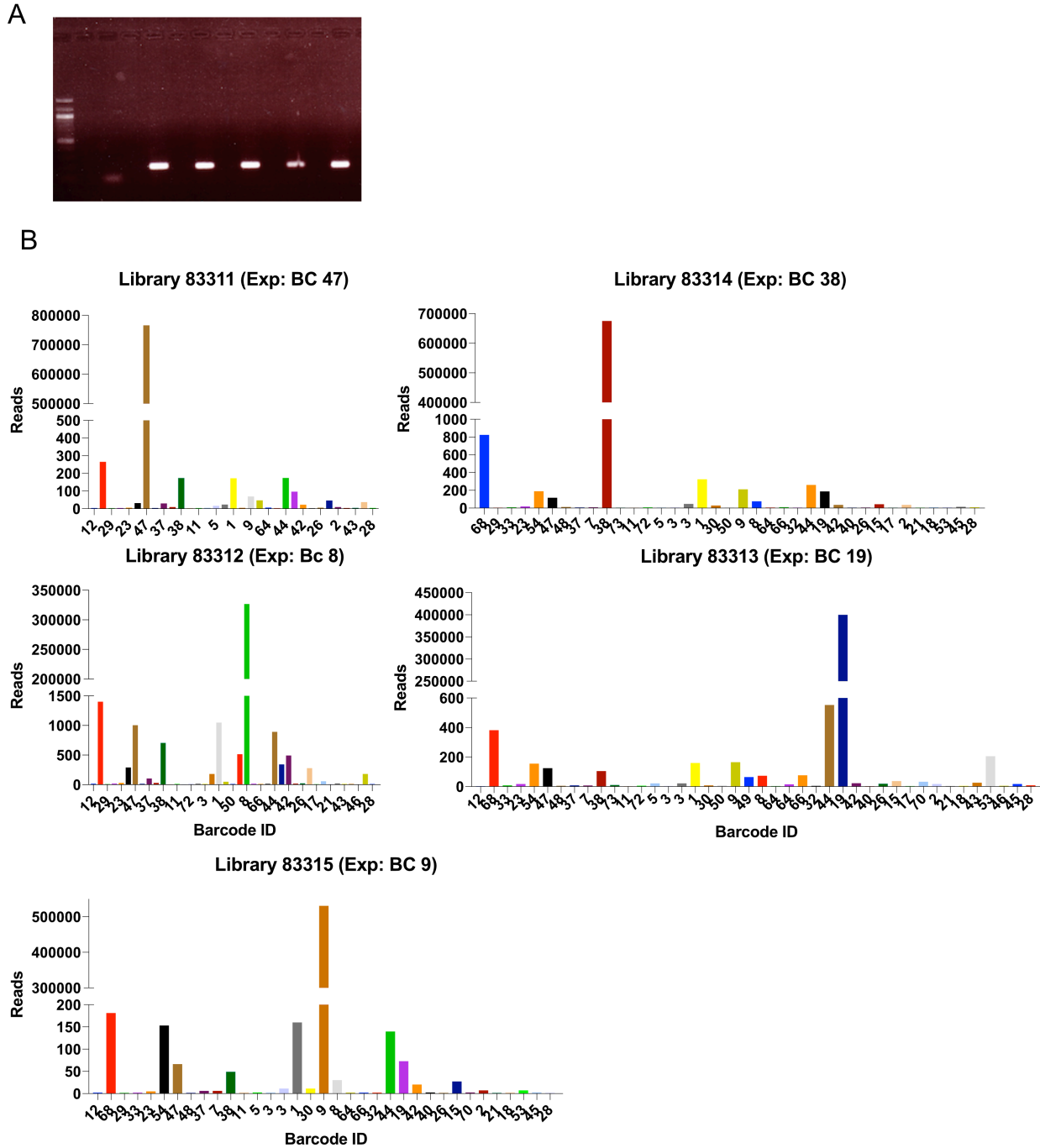


Figure 2.5. PCR-based multiplexed Illumina library preparation method can be used to accurately identify sequenced barcode-index pairs. (A) Agarose gel of PCR products following attachment of Illumina adaptors to barcode-index amplicons (Lane 1: 100 bp ladder; Lane 2: no DNA control; Lanes 3-7: PCR products). **(B)** Sequencing read counts for the 5 test samples using the PCR-based Illumina library preparation method. Each library corresponds to a single Illumina adaptor, and the expected barcode pair for each library is indicated.

CPs in nude mice, so we expected that some of the CPs would be present at relatively low levels within the tumors. It is well documented that both PCR and sequencer error can contribute to false-positive reads among rare variant populations using Illumina sequencing technology, including in DNA barcoding systems [74]. Additionally, we observed low-level sequencer ‘noise’ among our *in vitro* samples, suggesting that we would need a reliable thresholding method to discriminate between true low-read count signal and low-read count false-positive signal within this data (**Figure 2.5B**). As these experiments were discovery-based rather than for system validation, we were not going into them knowing which barcodes among the 30 in HMLER^S to expect to be detected, so we had to modify our thresholding strategy from the one employed in section **2.4.5**.

There are 70 additional Luminex barcode sequences available that were not introduced into HMLER^S. I had previously verified that 17/70 of the additional Luminex barcodes were detectable using Sanger sequencing. I therefore decided that these sequences represented an ideal ‘unexpected’ barcode population that I could use to threshold my *in vivo* sequencing data. When analyzing the next-generation sequencing data, we searched for not only the 30 expected barcode sequences, but also the 17 unexpected sequences among the sequencing reads. I then compared the number of sequencing read counts for the barcodes in the expected and unexpected groups. I designated the highest unexpected barcode read count within each sample as the false positive threshold for that tumor. Any ‘expected’ barcodes that had read counts above this threshold were considered to be true signal, and any ‘unexpected’ barcodes

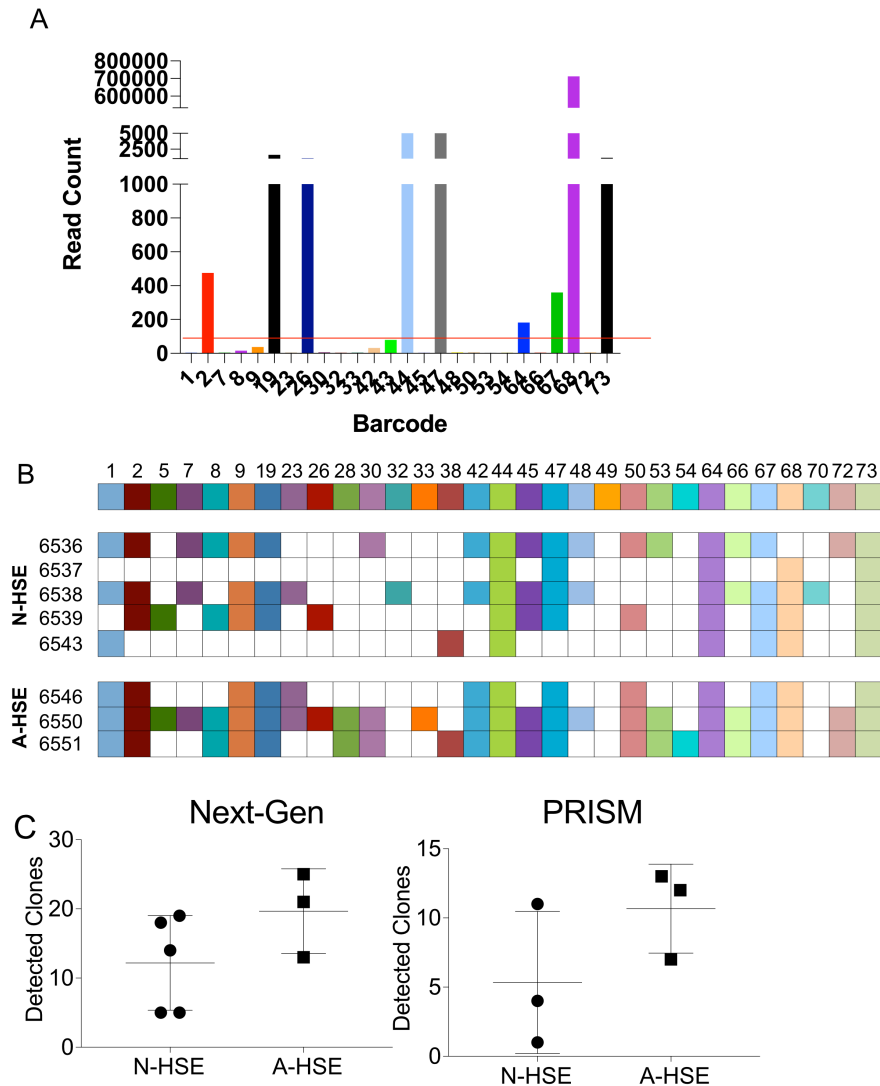


Figure 2.6. Luminex barcodes can be detected using next-generation sequencing. (A) Read counts for each barcode from an *in vivo* tumor sample. The only false positive read corresponds to CP-47, which was used as the false-positive threshold (red line). Any ‘expected’ barcodes with read counts below this read count were discarded as sequencer noise. (B) Summary of barcodes detected from 7 tumor samples using next-generation sequencing barcode detection. Rows represent individual tumors and columns represent barcodes. Tumors from two mouse cohorts (N-HSE and A-HSE) are represented. (C) Average number of CPs detected per tumor in each mouse cohort in experimental repetitions that employed either the next-generation sequencing based barcode detection method or the PRISM method.

that had read counts below this threshold were discarded as noise (**Figure 2.6A**).

I tested this thresholding strategy by repeating the *in vivo* experiment described in **Figure 2.2** and using the next-generation sequencing based detection method to perform barcode composition analysis. Using this method, I was able to successfully detect barcodes in all tumor samples analyzed and employ the thresholding strategy described above to remove low-level reads below the false positive threshold (**Figure 2.6B**). This method does appear to be more sensitive than the PRISM based detection method, as there was an increase in the number of low-frequency variants detected in tumors from both systemic environments using the sequencing-based detection method compared to the PRISM method (**Figure 2.6C**). Together, this data suggested that we had developed a next-generation sequencing based detection method that could be used to analyze Luminex barcode composition in both *in vitro* and *in vivo* samples.

2.5 Discussion

DNA barcoding is a powerful technology that allows for the tracking of clonal dynamics in both normal physiological and disease settings. In the context of cancer, DNA barcoding can be used to answer a wide range of biological questions including descriptive studies of intratumoral heterogeneity, tracking shifts in clonal dynamics in response to selective pressures (such as drug treatment), and tracking disease progression through the identification of metastatic founders. The technologies employed to track clonal dynamics have evolved at a rapid pace and have become increasingly sensitive and quantitative.

The PRISM system is a powerful DNA barcode detection system that was designed to provide a high throughput and highly adaptable screening system for complicated *in vitro* drug sensitivity studies [68]. We found that the PRISM system's Luminex barcodes can be readily introduced into CPs from the HMLER-HR-tdTomato cell line. The Luminex barcodes can be readily amplified from gDNA extracted from *in vitro* cultured HMLER-HR CPs and detected using the PRISM system with high specificity and low background signal. The disadvantage of this system is that it requires access to specialized equipment that is not readily available in most lab settings, and it is not amenable to tracking *in vivo* clonal dynamics at a level that is sensitive enough to meet our needs.

We developed a next-generation sequencing based detection system that was able to accurately detect the Luminex barcodes from both *in vitro* and *in vivo* samples. The common flanking sequence surrounding the barcodes allows for the amplification of multiple barcodes with a single PCR step, increasing the high-throughput nature of the

system. This feature also decreases the diversity of the samples, requiring the addition of PhiX to the sequencing reaction. This work around does not detract from the accuracy of the method, but it does take up space on the sequencing lane, reducing the total barcode read count. Future refinements of the barcoding system could incorporate staggered primers to introduce diversity at the termini of the barcode amplicon regions, removing the necessity for the addition of PhiX and increasing barcode sequencing depth.

The current next-generation barcode detection system allows for multiplexing of samples, increasing the efficiency of the sequencing step and reducing total cost. However, a much higher degree of multiplexing is possible with this system and future iterations could incorporate the use of barcode-index specific R primers to make the protocol more high-throughput.

An important observation made during the development of this protocol was that ligation-based Illumina library preparation methods might not be appropriate for multiplexed barcoding systems. Ligation efficiency is often low, necessitating the addition of a PCR-amplification step in order to generate sufficient library material for sequencing. This introduces a step in which sample contamination can occur at the barcode-index level, making it impossible to accurately deconvolute results and generating false-positive sequence reads within individual samples. Here we have demonstrated that the alternate PCR-based library preparation methods are more appropriate for multiplexed library preparation.

In the future, this system should be evaluated for its ability to sensitively detect barcodes extracted from smaller lesions, including micrometastatic outgrowths. We

have already demonstrated that the detection system is capable of detecting low-frequency barcode variants, however we have not evaluated the limits that could be imposed by the potential increased signal-to-noise ratio in smaller outgrowths.

2.6 Conclusions

Here I have described a method for adapting the Luminex-based PRISM barcoding system developed in the Golub lab to a next-generation sequencing based barcode detection method. We demonstrated that our method allows for the accurate detection of Luminex-barcodes from both *in vitro* and *in vivo* samples in a multiplexed, high-throughput fashion. The system is also amenable to additional layers of multiplexing, allowing for future increases in efficiency. Additionally, we identified a potential source of error in ligation-based Illumina preparation methods when employing multiplexed barcode sequencing, and suggest a PCR-based library preparation protocol that serves as a suitable alternative. This represents a valuable tool for the evaluation of clonal composition of tumor cells and explants, that could easily be adapted for use in other models.

Chapter 3

**The host systemic environment can direct functionally consequential
enhancement of intratumoral heterogeneity**

*The entirety of this chapter will be submitted as a manuscript, on which Jessica Olive will be first author, to a peer-reviewed journal.

Acknowledgements

This study was designed by Jessica Olive and Dr. Zafira Castano, with supervision from Dr. Sandra McAllister. Dr. Channing Yu and Aristotle Mannan (Golub Lab, Broad Institute) provided the lentiviral barcode vectors and performed barcode composition analysis using the PRISM system. Dr. Zafira Castano and Dr. Jarom Chung generated the HMLER-HR-tdTomato barcoded cell lines. Dr. Zafira Castano and Tyler Laszewski assisted with *in vivo* experiments. The Harvard Biopolymers Facility performed next-generation sequencing. Dr. Rory Kirchner (HSPH) performed next generation sequencing data analysis. Dr. Ted Natoli (Broad Institute) performed L1000 gene expression analysis. Dr. Rebecca Gelman (DFCI) provided assistance with statistical analyses. Jessica Olive performed all other experiments and data analysis.

3.1 Abstract

The ability of cancer cells to respond to systemic and local microenvironments, especially during periods of indolence, is recognized as a critical determinant of malignancy and disease progression. It is not known whether select sub-populations of tumor cells are endowed with these abilities or whether malignant progression is a stochastic process. Recent genetic and genomic analyses have provided certain insights into copy number and clonal relationships within heterogeneous tumors. Nevertheless, how intratumoral phenotypic and functional diversity arises and the role it plays in malignancy are not understood. Using a unique barcoding approach that enables us to trace discrete clonal populations among heterogeneous tumors, we report that systemic processes shape intratumoral diversity and the selection of malignant phenotypes within a population of otherwise indolent triple-negative breast cancer (TNBC) cells. The presence of a distant TNBC tumor is associated with an increase in intratumoral heterogeneity and a reduction in innate immune cell infiltration. The observed systemically-driven selection results in enhanced disease progression and reduced sensitivity to chemotherapy *in vitro* and *in vivo*. Importantly, our experimental approach allows us to study the selected subpopulations both before and after their progression and response to therapy. These results have implications for improved risk assessment and new therapeutic approaches to treat breast cancer patients.

3.2 Introduction

Among women in the United States, breast cancer is the most common type of newly diagnosed cancer and is the second leading cause of cancer related death [1]. Multiregion sequencing of primary tumors and metastases from patients with breast cancer, along with a number of other cancer types, has identified intratumoral mutational heterogeneity in the majority of regions sampled [33]. Intratumoral heterogeneity has implications for tumor evolution, therapeutic efficacy, and disease progression [30]. Although differences in the mutational profile of tumor cell subpopulations may be the best-documented parameter of tumor heterogeneity, it is ultimately the functional heterogeneity, a result of both genetic and non-genetic sources of heterogeneity, which drives the clonal evolution process, thereby directing disease progression [27]. The effects of functional heterogeneity have been largely unexplored, resulting in a lack of understanding of the phenotypic properties that drive the selection process. Perhaps more importantly, there is a complete lack of understanding of the forces that direct the generation and maintenance of heterogeneity, making it difficult to interdict the process.

Cell extrinsic properties, such as interaction with the tumor microenvironment or the systemic environment, can also contribute to heterogeneity and promote cancer progression [26]. Modulations to the host systemic environment by primary tumors, surgery, and other inflammatory processes have been demonstrated to promote disease progression and metastasis [42-48, 52, 53]. Our lab previously described a model of host

systemic activation, in which certain distantly located tumors are able to trigger the malignant conversion of normally indolent tumor cell populations of the HMLER-HR TNBC cell line, through the use of circulating factors, mobilization of pro-tumorigenic bone marrow cell populations and activation of the tumor microenvironment [44, 45, 47]. Interestingly, the differentially activated host systemic environments promote the formation of HMLER-HR tumors with vastly different histopathologies and molecular profiles, despite having an identical cell line of origin [44-47]. We hypothesized that host systemic activation could drive the selection of unique subclonal populations, resulting in differential patterns of intratumoral heterogeneity that correspond to the distinct histopathologies that we previously observed.

Here we use a molecular barcoding system to demonstrate that host systemic activation can direct functionally consequential enhancement of heterogeneity. HMLER-HR tumors recovered from an activated host systemic environment (A-HSE) are significantly more heterogeneous than those recovered from a naïve host systemic environment (N-HSE). The enhanced heterogeneity corresponded to a reduction in intratumoral innate immune cell infiltration. Tumors recovered from NSG mice, which have dysfunctional innate immune systems, also exhibited enhanced intratumoral heterogeneity compared to those from the N-HSE. Together, this suggests that host systemic modulation of innate immune function can direct the generation of specific patterns of intratumoral heterogeneity.

Importantly, our unique molecular barcoding system allows for the functional characterization of clonal populations that were identified as being biologically relevant. Follow up studies revealed that the unique subclonal combinations that were selected for in the A-HSE were able to function cooperatively and exhibited reduced sensitivity to doxorubicin, 5-fluorouracil, and paclitaxel *in vitro* and doxorubicin *in vivo*. Therefore, the activated host systemic environment selected for functionally relevant clonal populations that could potentially contribute to disease progression and therapeutic resistance. This highlights the need for further investigation into the forces driving intratumoral heterogeneity and its consequences for disease outcome.

3.3 Materials and Methods

3.3.1 Cell lines

HMLER-hygro-H-*ras*V12 (HMLER-HR) cells [47, 69] were cultured in advanced DMEM/F12 (Gibco) supplemented with 5% calf serum (CS, HyClone), 0.1% hydrocortisone (Sigma Aldrich), and 1% Penicillin Streptomycin (Gibco) at 37C with 5% carbon dioxide (CO₂).

293T cells were cultured in DMEM (Gibco) supplemented with 10% FBS (Gibco) and 1% Penicillin Streptomycin (Gibco) at 37C with 5% CO₂. All cell lines were confirmed to be mycoplasma negative.

3.3.2 Lentiviral infection

293T cells were transfected with 2.5 µg of lentiviral vector DNA (PLV-tdTomato was a generous gift from Dr. Robert Weinberg; barcode vectors were generous gifts from Todd Golub, Broad Institute, [68]), 2.5 µg PHR' (Addgene plasmid 8455), and 1 µg VSVG (Addgene plasmid 8454) in Opti-MEM Reduced Serum Medium (Gibco) with Fugene HD (Promega). 48 and 72 hours following transfection, viral supernatants were collected and were filtered through a 40 micron syringe filter. Viral supernatants were stored at -80C and were mixed together prior to infection.

For lentiviral infection, HMLER-HR cells were infected with a 1:1 mixture of the appropriate viral supernatant in media with Polybrene (Sigma Aldrich). 72 hours after infection, isolation of successfully infected cells was performed, either by FACS for tdTomato+ cells (for generation of the HMLER-HR-tdTomato cell lines) or selecting for blasticidin resistance (for lentiviral barcode infections).

3.3.3 Single cell cloning

HMLER-HR cells expressing tdTomato (HMLER-HR-tomato) were stained with antibodies against CD44 (APC-conjugated, BD Biosciences) and CD24 (FITC-conjugated, BD Biosciences) in PBS with 2% FBS for 30 minutes on ice. Single cells were determined to be tdTomato-positive and expression levels of CD44/CD24 were determined prior to sorting into single wells of a 96-well plate. Single cell clonal cell lines were expanded in culture.

3.3.4 Clonal population pooling

Equal numbers of 30 clonal populations were mixed to form the CP Pool, referred to as HMLER^S (**Table 2.1**). Aliquots with 500,000 HMLER^S cells were frozen down to serve as the starting point for future experiments.

3.3.5 Genomic DNA preparations

Genomic DNA for barcode detection using the PRISM system was extracted using a Proteinase K/Tween-20/NP40 lysis buffer, as previously described [68]. Genomic DNA for barcode detection using next-generation sequencing was extracted using the QiaAmp DNA Mini Kit (Qiagen) and was eluted in 200 µl of water. Final DNA concentration was quantified using a Nanodrop 8000 Spectrophotometer (Thermo Fisher).

3.3.6 Long-term proliferation kinetics assays

Individual CPs or HMLER^S were plated in triplicate at a density of 100,000 cells/well in a 6-well plate (Corning). Cells were passaged and counted when they reached ~70% confluence (or approximately every 1-4 days) and were then replated in triplicate at 100,000 cells/well. The assay was carried out for a total of 14 days.

Cell counts were used to extrapolate and estimate the overall proliferative capacity of each cell line at each passage point over the 14-day time period using the equation: $T_2 = (C_2/100,000) * C_1$, where T_2 is the extrapolated total number of cells, C_2 is the total cell count from passage 2, and C_1 is the total cell count from passage 1. This calculation was performed for T_3 through the final passage. The log of each total extrapolated cell count was plotted against time (days) and the slopes of these lines were used to compare the proliferation kinetics rates of individual CPs.

3.3.7 Tumorsphere formation assays

100 cells were plated per well (n=5 per CP) in 100 μ l MammoCult media (Stem Cell Technologies) in ultra-low attachment 96 well plates (Corning). 50 μ l of fresh media was added every 72 hours. After 7 days, wells were imaged and tumorspheres were manually counted. Average tumorsphere counts are represented.

3.3.8 Animal experiments

Experiments were performed in 6-8 week old female NCr nude (sp/sp, Taconic) or NSG (Jackson NOD.Cg-*Prkdc*^{scid} *Il2rg*^{tm1Wjl}/Szj) mice. All mouse cohorts received subcutaneous injections of 2×10^6 HMLER^S cells suspended in 100 μ l of 20% matrigel

(Corning). The naïve host systemic environment (N-HSE) cohort received a contralateral injection of 100 µl of 20% matrigel (Corning). The activated host systemic environment (A-HSE) cohort received a contralateral injection of 2×10^5 BPLER cells [70] suspended in 100 µl of 20% matrigel (Corning). Tumors were measured using calipers once per week and tumor volume was calculated as $0.5 \times \text{length} \times \text{width}^2$.

For chemotherapy studies, mice received identical bilateral, subcutaneous injections of 2×10^6 A-HSE[§] or N-HSE[§] cells. Tumors were measured using calipers three times per week and tumor volume was calculated as $0.5 \times \text{length} \times \text{width}^2$. At day 33, when the majority of mice had palpable tumors (average tumor volume: 25 mm³) mice were randomized into vehicle (saline) and treatment (doxorubicin: 1.5 mg/kg, Patterson Veterinary) groups. Mice received the appropriate treatment via retro-orbital injections at days 35, 37 and 42.

Mice were euthanized via CO₂ inhalation. All mouse experiments were performed in accordance to federal laws and institutional guidelines and were approved by the Institutional Animal Care and Use Committee of Boston Children's Hospital Brigham and Women's Hospital (Protocol 2017N000056).

3.3.9 Polymerase chain reaction

The barcode region of the lentiviral barcode vector was amplified using either primer set JO primer F/R (F: TGGAGCATGCGCTTTAGCAG; R: ATCGTTTCAGACCCACCTCC) or indexed primer sets (F: JH p05: ATC GTT TCA GAC CCA CCT CCC; R: JH p11-14 and JH p31-46, **Table 2.2**). PCR reaction mixtures contained 250 ng DNA, OneTaq 2x MasterMix (New England Biolabs), and 10 µM each

of F/R primers. The following PCR program was used to PCR amplify the template DNA: 94C for 30 seconds; repeat the following steps for 30 cycles: 94C for 20 seconds, 54C for 30 seconds, 68C for 20 seconds; final extension at 68C for 5 minutes). PCR products were purified using Agencort AMPure XP beads (Beckman Coulter) according to the manufacturer's protocol and purified DNA was eluted in 20-40 µl water.

3.3.10 Illumina sequencing library preparation

Ligation-based Illumina library preparation was carried out by the Harvard Biopolymers Facility using an Integex Apollo 324 PrepX ILM kit using Kappa reagents, according to manufacturers' protocols. Ligation products were PCR amplified using primers against the P5/P7 Illumina adaptor regions.

For PCR-based Illumina library preparation, samples that had been amplified using one of the barcode-indexed primer sets were subject to a second PCR step using an Illumina indexed primer set with regions that were complementary to the barcode lentiviral vector regions (F: JO p50, R: JO p65-p88, **Table 2.3**).

PCR reaction mixtures contained 100 ng DNA, OneTaq 2x MasterMix (New England Biolabs), and 10 µM each of F/R primers. The following PCR program was used to PCR amplify the template DNA: 94C for 30 seconds; repeat the following steps for 15 cycles: 94C for 20 seconds, 54C for 30 seconds, 68C for 20 seconds; final extension at 68C for 5 minutes. PCR products were purified using Agencort AMPure XP beads (Beckman Coulter) according to the manufacturer's protocol and purified DNA was eluted in 20-40 µl water.

3.3.11 Next generation sequencing data analysis

Next-generation sequencing data analysis was analyzed by Dr. Rory Kirchner by identifying index and barcodes in each read by searching for the pattern [8 base index]-[17 bases]-ACGCGT-[24 base barcode]-CTGCAG and counting the index-barcode pairs.

3.3.12 Immunohistochemistry

Immunostaining for α -SMA (Biolegend, clone 1A4) was performed as previously described [47], using the Vectastain mouse secondary kit (Elite ABC-HRP, PK-6102) and AEC Chromagen (Dako). Hematoxylin counterstaining was performed (Vector). Hematoxylin and eosin, F4/80 (clone CI:A3-1, AbD Serotec), and myeloperoxidase (Dako, A0398) stains were performed by the BWH/DF HCC Specialized Histopathology Services facility.

3.3.13 Microscopy and image analysis

Images were taken using a Nikon Eclipse Ni microscope using NIS Elements software. For select samples, whole tumor imaging was performed and images were stitched together with the NIS Elements software. Quantifications of MPO stains were performed using CellProfiler software (Broad Institute). F4/80 localization was scored in a blinded fashion.

3.3.14 Flow cytometry

Individual CPs, HMLER[§], or the HMLER[§] subpools were plated and treated with either vehicle control (PBS) or 10 ng/ml recombinant human IFN-gamma (Peprotech). After 24 hours, cells were trypsinized, and between 250,000-1,000,000 cells per condition were stained with FITC-CD47 (Biolegend) and APC-Cy7 HLA-A,B,C (Biolegend) for 30 minutes in the dark on ice. Cells were fixed and permeabilized (eBioscience, catalog 00-5521-00) and stored at 4C overnight. Flow cytometry was performed on a FACS Canto (BD Biosciences) and FlowJo (TreeStar) was used for data analysis.

3.3.15 LINCS L1000 gene expression analysis

Individual CPs, HMLER[§], or the HMLER[§] subpools were plated at a density of 2,000 cells/well in a 96 well plate. RNA was extracted and L1000 profiles were generated as previously described [75].

3.3.16 Protein arrays

Serum-free media was added to subconfluent cell culture plates containing the HMLER subpools and was incubated for 24 hours. Conditioned media was removed and stored at -80C. Cells were trypsinized and counted, and cell lysates were generated using Lysis Buffer 17 (R&D Systems) and proteinase inhibitor (Sigma). Conditioned media was profiled using a Proteome Profiler Human Chemokine Array kit (R&D Systems, catalog #ARY107) and cell lysates were profiled using a Proteome Profiler Human Cytokine Array kit (R&D Systems, catalog #ARY005B). Arrays were imaged

using a ChemiDoc Imaging System (BioRad) and image analysis was performed using ImageJ (NIH).

3.3.17 ELISAs

Serum-free media was added to subconfluent cell culture plates containing the HMLER subpools and was incubated for 24 hours. Conditioned media was removed and stored at -80C. ELISAs were performed on conditioned media according to manufacturer's instructions using a Human IL-8/CXCL8 Quantikine ELISA Kit (R&D Systems, D800C), Human G-CSF Quantikine ELISA Kit (R&D Systems, DCS50), or Human CXCL1/GRO alpha Quantikine ELISA Kit (R&D Systems, DGR00B). Absorbance was measured using a FilterMax F5 Multi-Mode Plate Reader (Molecular Devices) with SoftMax Pro 6.4 software.

3.3.18 Cell Titer Glo assays

HMLER^s or the HMLER^s subpools were plated at 5,000 cells/well in 96 well plates. After 24 hours, cells were treated with the vehicle (DMSO) or the appropriate chemotherapy dose (doxorubicin: 10 nM, 50 nM, 100 nM, 10 uM; paclitaxel: 1 nM, 50 nM, 10 uM, 50 uM; 5-fluorouracil: 50 uM, 250 uM, 500 uM, 1 mM; n=6 per concentration per cell line). All chemotherapeutics were purchased from Sigma. 72 hours after the initiation of treatment, cell viability was measured using CellTiter-Glo Luminescent Cell Viability Assay (Promega), following manufacturer's instructions. Luminescence measurements were normalized to the vehicle control.

3.3.19 Statistical analysis

Statistical analyses were performed using PRISM 7 software (GraphPad). *In vitro* chemotherapy studies were analyzed by Dr. Rebecca Gelman using a two-sided Wilcoxon rank sum test, stratified for dose.

3.4 Results

3.4.1 Generation of a collection of heterogeneous, barcoded clonal populations from the HMLER-HR cell line

In order to identify the cells within a heterogeneous, normally indolent tumor cell population that are capable of responding to systemic and microenvironmental cues to progress to malignancy, we developed a unique molecular barcoding system that would enable us to analyze intratumoral subclonal composition. We first generated 30 single cell-derived subclones from a parental triple-negative human breast cancer cell line (HMLER-HR) [47, 69], which we refer to as clonal populations (CPs). To do so, we sorted single cells based on their CD24/44 profiles as an arbitrary way to capture heterogeneity, and expanded these to establish the CPs (**Figure 3.1A**). Each individual CP was infected with a unique, heritable 24-base pair DNA barcode sequence that can be PCR amplified from genomic DNA preparations using a common barcode flanking sequence and is detectable using either the Luminex-based PRISM detection system [76] or next-generation sequencing (**Figure 3.1A, Figure 2.4**).

The individual barcoded CPs were morphologically heterogeneous, ranging across a spectrum from epithelial to mesenchymal (**Figure 3.1B**). In addition, the CPs differed in their long-term *in vitro* proliferation kinetics and the ability to form tumorspheres in suspension culture (**Figure 3.1C**). Targeted exome sequencing of a selection of CPs did not reveal genetic heterogeneity between the CPs (data not shown).

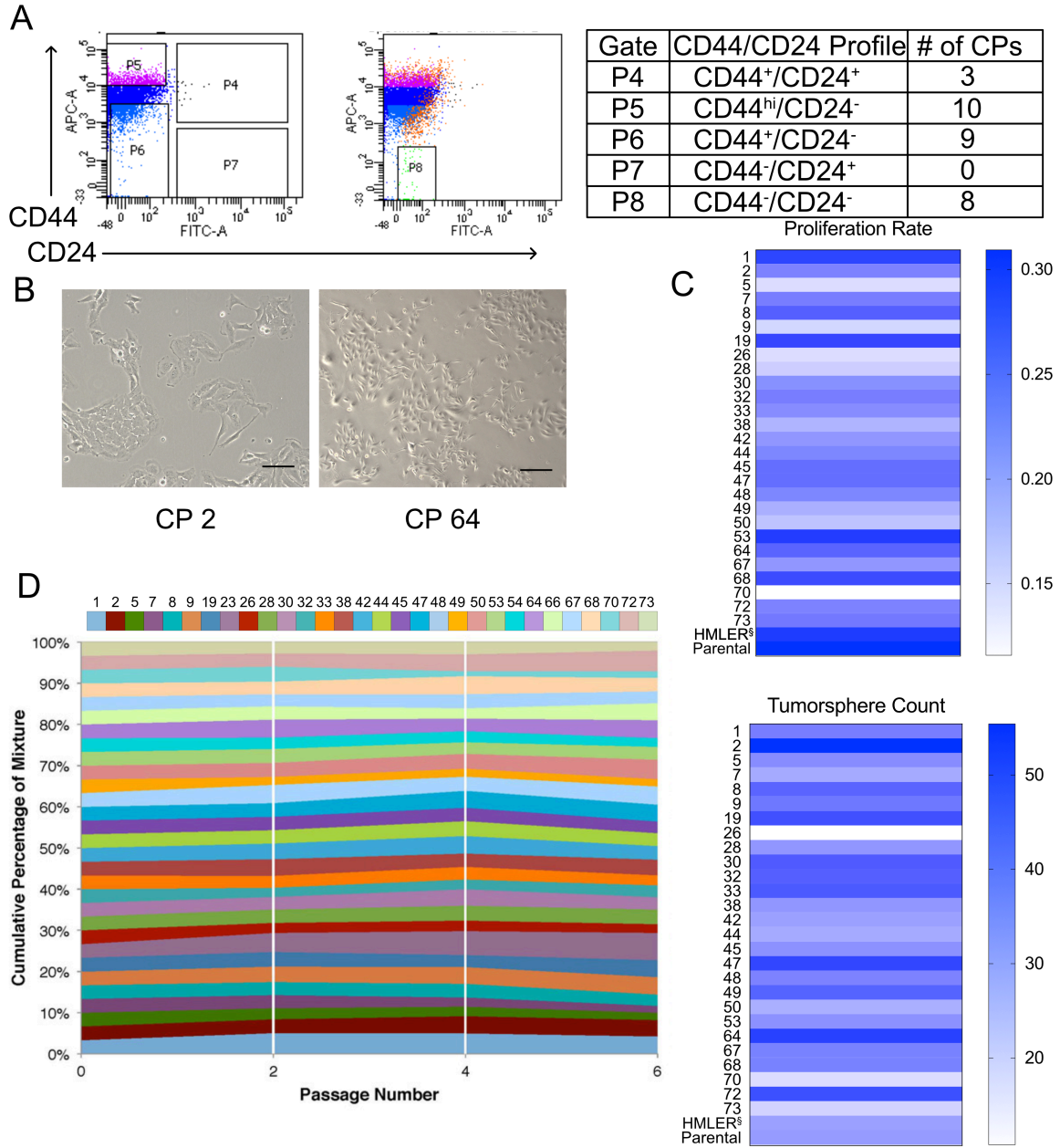


Figure 3.1. HMLER clonal populations are functionally heterogeneous. (A) CD44/CD24 gating strategy for FACS to isolate single cell clones that were used to generate thirty clonal populations from the HMLER-HR-tdTomato cell line. **(B)** Phase microscopy images of two CPs with varying degrees of epithelial and mesenchymal morphology. Scale bars = 100 μ m. **(C)** Heat maps representing range of proliferation rates and tumorsphere formation rates of individual CPs, HMLER^S, and the parental HMLER-HR-tdTomato (HMLER^P) cell line. **(D)** Sandplot showing clonal composition of HMLER^S over 6 passages *in vitro*.

Having established that the CPs were phenotypically diverse, we then mixed an equal number of each of the 30 barcoded CPs to generate a clonal population pool, referred to as HMLER[§]. We determined that HMLER[§] is stable in culture over time, with no CPs becoming dominant or extinct during six passages (**Figure 3.1D**). The advantage of this molecular barcoding approach is that by introducing single barcodes into clonal populations and then generating the pooled HMLER[§] rather than infecting the bulk parental population with a library of barcodes, we gain the ability to retroactively characterize CPs that are selected for from HMLER[§] in any given experiment. This approach also allows us to be confident that the same barcode is not unwittingly introduced into multiple unique clonal populations, thus confounding subsequent analyses.

3.4.2 The activated host-systemic environment is associated with enhanced HMLER[§] intratumoral heterogeneity

To evaluate how CPs within HMLER[§] responded to systemic influences, we evaluated its responses to an *in vivo* assay that models host systemic activation. Our lab previously identified particular tumors that are capable of activating the host systemic environment (through secretion of circulating factors, mobilization of pro-tumorigenic bone marrow cell populations, and modifications of distant microenvironments), and consequently generated a tumor permissive systemic environment in which normally indolent tumor cell populations can acquire malignant phenotypes [44-47]. These tumors' ability to modulate the host systemic environment can be leveraged to model host systemic activation, using

a contralateral tumor injection schema. In this model system, a normally indolent tumor cell line (in this case, HMLER^S) is injected contralaterally to either an activating tumor (here, the TNBC cell line (BPLER); referred to as the activated host systemic environment or A-HSE) or a Matrigel control injection (referred to as the naïve host systemic environment or N-HSE; **Figure 3.2A**). This system allows for the evaluation of the response of HMLER^S to systemic influences, as HMLER^S and BPLER cells: (1) do not physically contact one another; and (2) are unlikely to communicate via paracrine signaling due to their lack of physical proximity.

We injected HMLER^S cells into both N-HSE and A-HSE nude mice, and after a period of 90 days or at ethical end points (maximum volume 1.5 cm³), HMLER^S tumors were recovered (**Figure 3.2A, Figure 3.3**). Recovered tumors were characterized using immunohistochemical techniques and/or genomic DNA was extracted for barcode composition analysis. We found that, like HMLER^P, HMLER^S displayed unique histopathologies in the naïve-HSE and activated-HSE. For example, HMLER^S tumors recovered from A-HSE mice exhibited decreased levels of necrosis, increased cellularity, and increased stromalization compared to HMLER^S tumors recovered from N-HSE mice (**Figure 3.2B**). Additionally, HMLER^S tumors in the A-HSE exhibited higher levels of desmoplastic stroma formation (as measured by alpha-smooth muscle actin (α -SMA) positive

Figure 3.2. HMLER^S tumors recovered from the activated host systemic environment are more heterogeneous than those in the naïve host systemic environment. (A) Experimental schema for HMLER^S cell line injection into the naïve host systemic environment (N-HSE) and activated host systemic environment (A-HSE). **(B)** Representative images from hematoxylin and eosin (H&E) stained HMLER^S tumors recovered from N-HSE and A-HSE cohorts. Left panels imaged at 4x, right panels imaged at 20x. **(C)** Representative images from HMLER^S tumors recovered from N-HSE and A-HSE cohorts that were stained for α -SMA (brown) and counterstained with hematoxylin. Tumors imaged at 20x. **(D)** Representation of PRISM detected barcodes in individual HMLER^S tumors recovered from mice in the N-HSE and A-HSE cohorts. Individual tumors are represented across rows and barcode identity is represented along columns. **(E)** Number of detected CPs per HMLER^S tumor. Each point represents an individual tumor. Bars represent mean and SD (N-HSE n = 8, A-HSE n = 7; unpaired, two-tailed t-test).

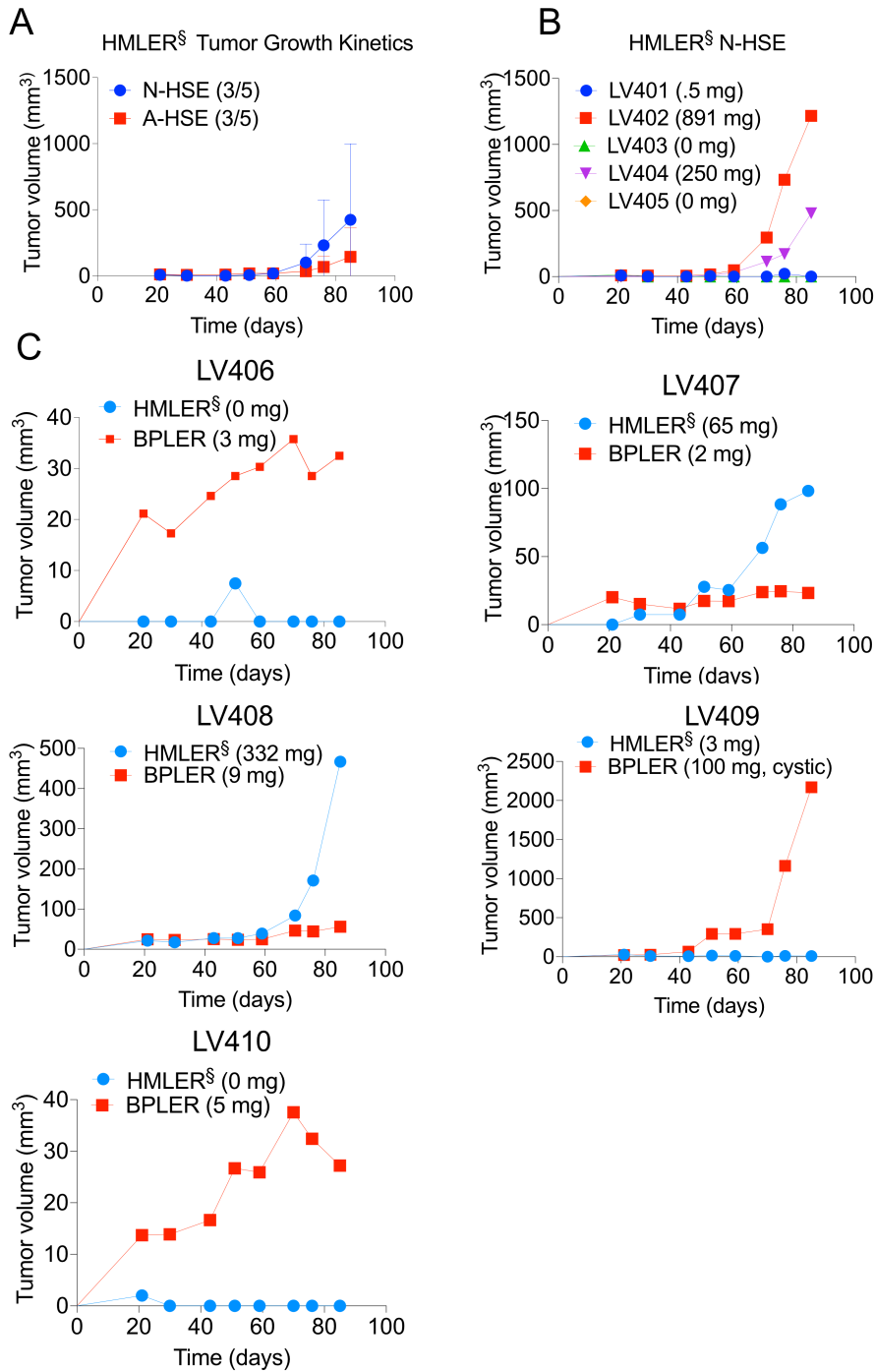


Figure 3.3. Tumor growth kinetics in N-HSE and A-HSE. (A) Average HMLER^s tumor kinetics in the N-HSE (blue) and A-HSE (red) cohorts. Incidence indicated in legend. Error bars represent SD. **(B)** Tumor kinetics of individual HMLER^s tumors in the N-HSE cohort. Final tumor mass indicated in legend. **(C)** Tumor kinetics of individual HMLER^s and paired BPLER tumors in the A-HSE cohort. Final tumor mass indicated in legend.

staining) compared to HMLER^S tumors in the N-HSE, in agreement with our previously published work (**Figure 3.2C**, [47]). Together, these data established that we had successfully captured the heterogeneity present in HMLER^P and that HMLER^S exhibited similar biology to the bulk parental cell line.

Next, we evaluated whether host systemic activation affected the patterns of intratumoral heterogeneity in HMLER^S tumors. Strikingly, a significantly higher number of CPs were detected in the HMLER^S tumors in the A-HSE compared to the N-HSE, with a per tumor average of 12 CPs and 4.5 CPs, respectively ($p=0.0001$, **Figure 3.2D,E**). The patterns of differential heterogeneity between the two cohorts, as measured by the number of detected CPs, occurred independent of tumor mass, as trends in the number of detected clones held across HMLER^S tumors with a wide range of masses (5 mg-891 mg) (**Figure 3.4**). One outlier HMLER^S tumor was present in the TNBC cohort, with only 3 clones detected (**Figure 3.2D**, LV409). We believe that this was the result of ineffective host systemic activation, as the contralateral TNBC tumor was cystic and exhibited growth kinetics that differed drastically from the others in that group (**Figure 3.3**).

A total of 6 CPs were detected in HMLER^S tumors recovered from the N-HSE, and replicable selection of 4 of these CPs (CPs 8, 19, 38, and 67) was observed across all tumors in this cohort (**Figure 3.2D**). Of the 6 CPs detected in the N-HSE, 5 of these were also detected in HMLER^S tumors in the A-HSE cohort (CPs 8, 19, 38, 44 and 67), along with a group of 9 additional CPs that appeared exclusively in the A-HSE (**Figure 3.2D**). These data suggested that the

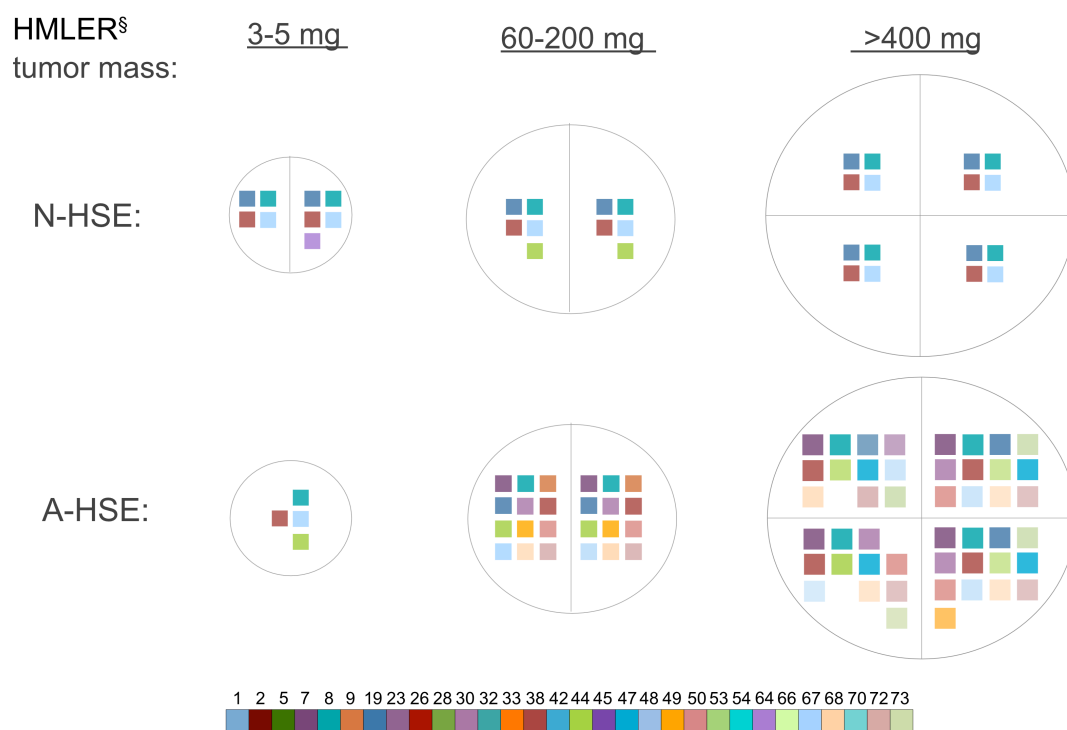


Figure 3.4. Differential levels HMLER^s intratumoral heterogeneity in N-HSE and A-HSE occurs independent of tumor mass. Clonal composition of roughly size-matched tumors in naïve and activated host systemic environments.

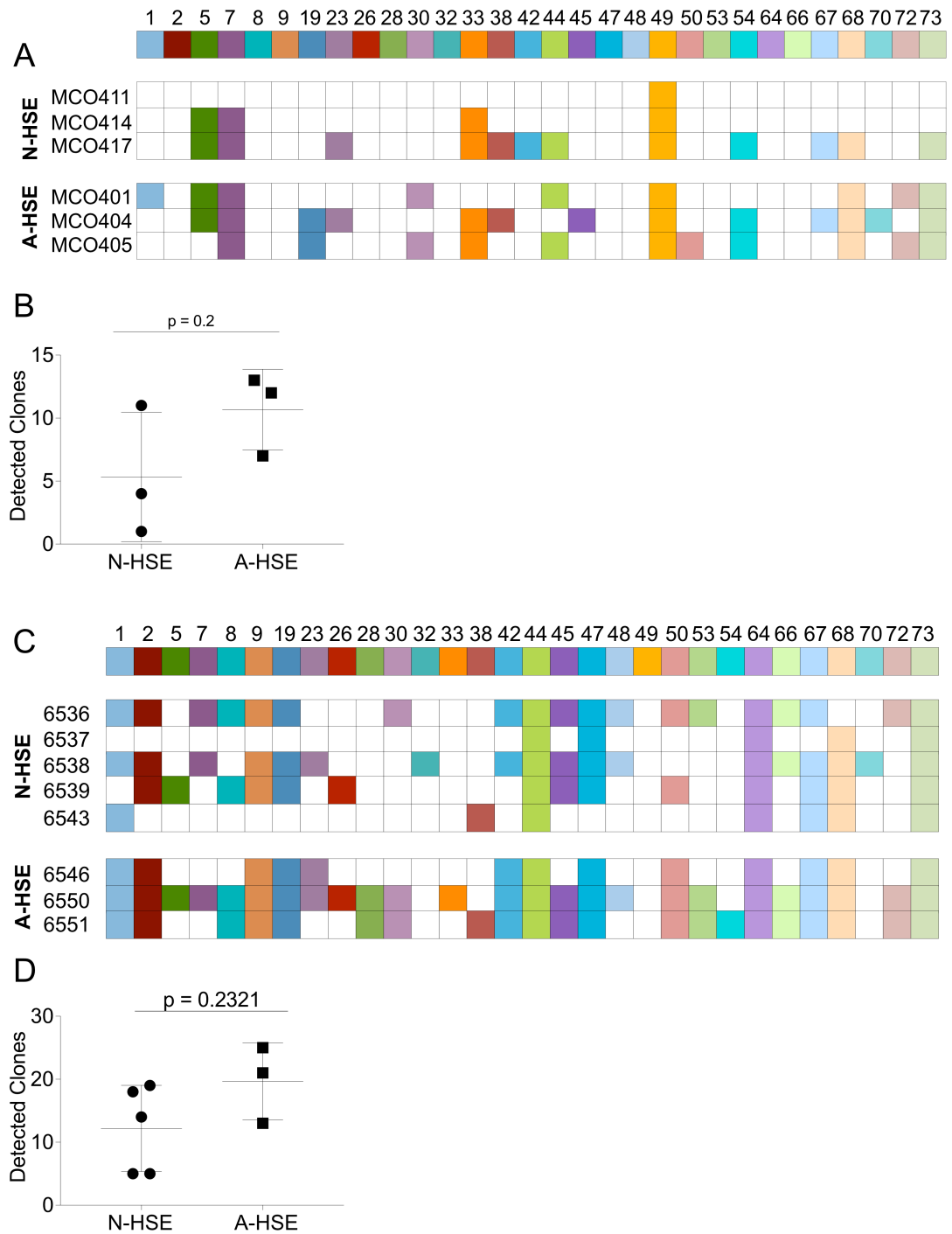
systemically driven selection was directed rather than stochastic. In two repetitions of this experiment, there were differences observed in the clonal composition of the HMLER^S tumors, however we consistently observed enhanced levels of heterogeneity in the tumors that responded to systemic activation (**Figure 3.5A,B**; average detected clones: N-HSE = 5.3, A-HSE = 10.7). The observation of enhanced heterogeneity in the A-HSE was independent of barcode detection method, with experiments using both the PRISM system and next-generation sequencing based barcode detection methods yielding similar results (**Figure 3.5C,D**; average detected clones: N-HSE = 12.2, A-HSE = 19.7). As noted in **Chapter 2**, regardless of the systemic environment, the average number of clones detected using the next-generation sequencing based barcode detection method was consistently higher than the average number of clones detected using the PRISM barcode detection method (**Figure 2.6C**).

3.4.3 Enhanced intratumoral heterogeneity in HMLER^S tumors is associated with differential innate immune cell infiltration

Previous work in our lab has demonstrated that the presence of a distant TNBC tumor generates an activated systemic environment that permits the outgrowth of normally indolent HMLER-HR tumors through cytokine secretion, modulations of the innate immune system (specifically granulins⁺ bone marrow progenitor cells), and CAF activation [45, 47]. We hypothesized that the enhanced heterogeneity that we observed in the A-HSE was another effect of

Figure 3.5. Enhancement of HMLER[§] intratumoral heterogeneity in A-HSE is replicable and independent of barcode detection method. (A) Representation of PRISM detected barcodes in individual HMLER[§] tumors recovered from mice in the N-HSE and A-HSE cohorts. Individual tumors are represented across rows and barcode identity is represented along columns. **(B)** Number of detected CPs per HMLER[§] tumor. Each point represents an individual tumor. Bars represent mean and SD (N-HSE: n = 3, A-HSE: n = 3; Mann-Whitney test). **(C)** Representation of next-generation sequencing detected barcodes in individual HMLER[§] tumors recovered from mice in the N-HSE and A-HSE cohorts. Individual tumors are represented across rows and barcode identity is represented along columns. **(C)** Number of detected CPs per HMLER[§] tumor. Each point represents an individual tumor. Bars represent mean and SD (N-HSE: n = 5, A-HSE: n = 3; Mann-Whitney test).

Figure 3.5 (Continued). Enhancement of HMLER^s intratumoral heterogeneity in A-HSE is replicable and independent of barcode detection method.



these systemic modulations. We posited that the A-HSE represents a permissive environment in which additional clones, which normally would not have become established within the HMLER^S tumors, were maintained. To examine this further, we began by characterizing the innate immune infiltrate, particularly neutrophils and macrophages, in HMLER^S tumors. Immunohistochemical staining of HMLER^S tumors for the neutrophil marker, MPO, revealed that the level of neutrophil infiltration was 6-fold higher in the N-HSE compared to the A-HSE ($p < 0.0001$, **Figure 3.6A,B**). Immunohistochemical staining of HMLER^S tumors for the macrophage marker, F4/80, revealed that macrophages were differentially localized in HMLER^S tumors recovered from the two cohorts. Specifically, macrophages were restricted to the periphery of all HMLER^S tumors recovered from the A-HSE, whereas 5/6 tumors recovered from the N-HSE setting exhibited intratumoral macrophage infiltration (**Figure 3.6C**).

3.4.4 A functional innate immune system is required for differential CP selection in N-HSE and A-HSE HMLER^S tumors

In order to further evaluate whether innate immune components played a role in shaping the unique clonal compositions observed in HMLER^S tumors in N-HSE and A-HSE cohorts, a repetition of the HMLER^S *in vivo* selection experiment was performed in which HMLER^S was injected into either the N-HSE or A-HSE in NSG mice (**Figure 3.7A**). Whereas nude mice have a functional innate immune system, NSG mice exhibit dysfunction of a number of innate immune cell components, including macrophages, dendritic cells, and NK cells [77].

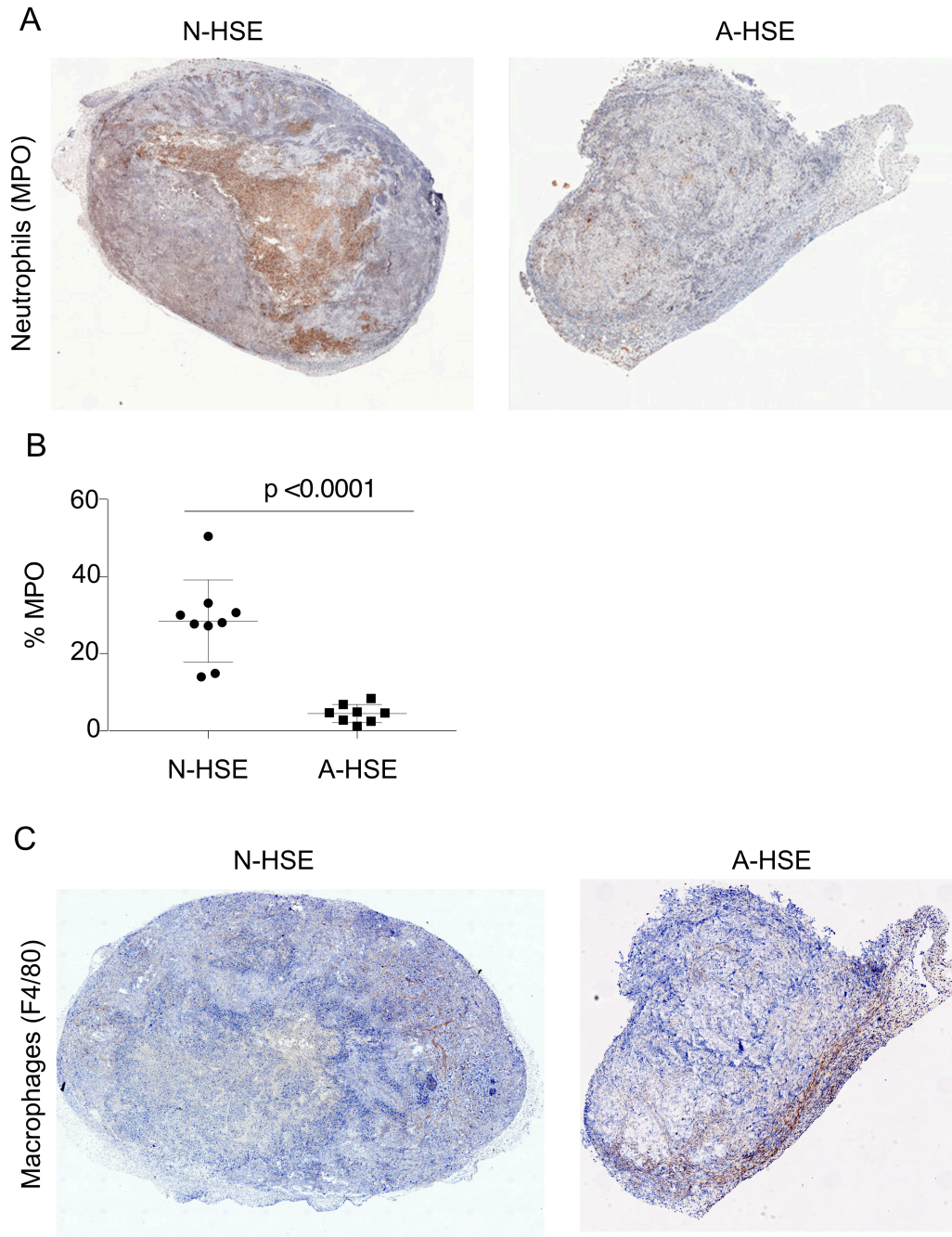


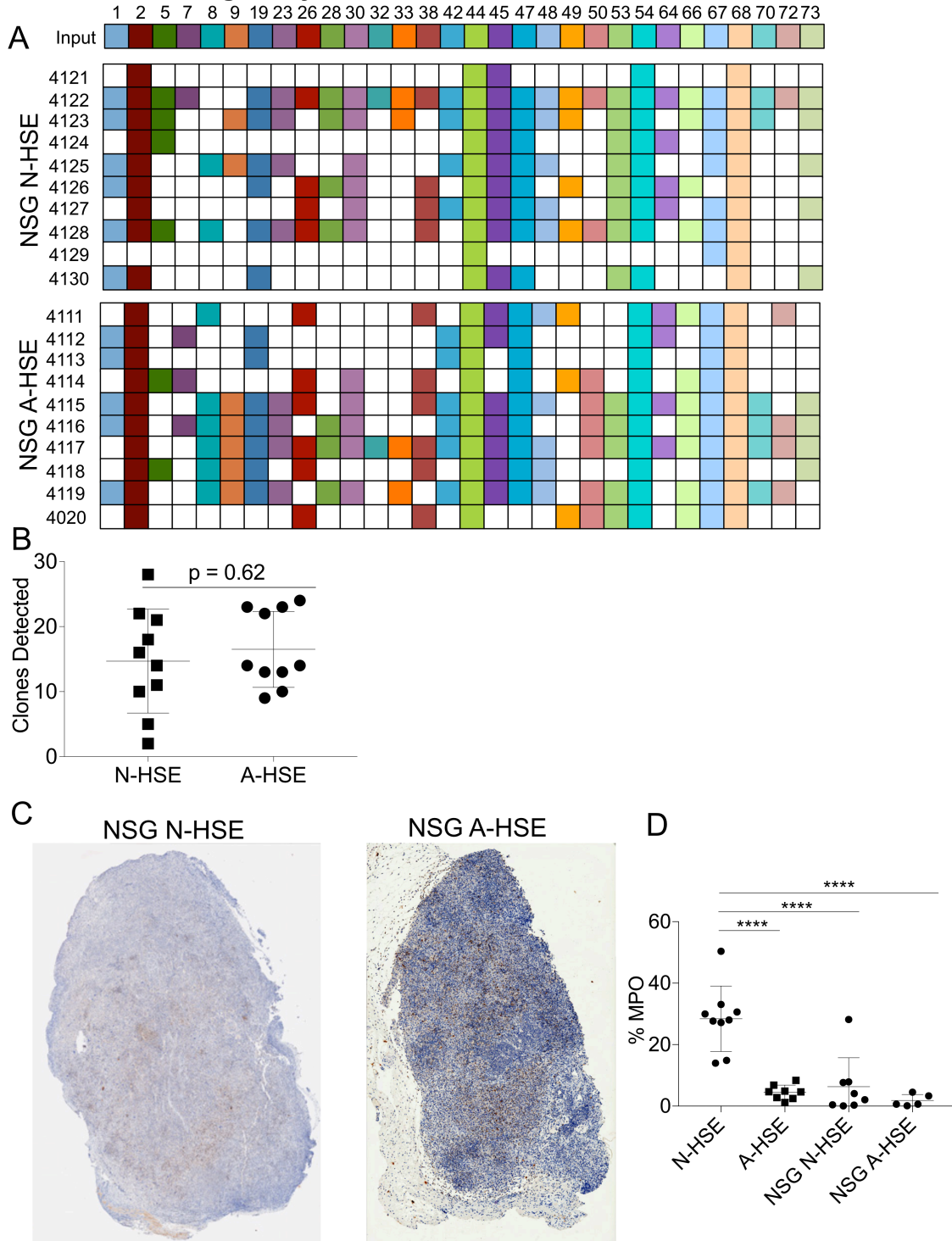
Figure 3.6. HMLER^S tumors in N-HSE and A-HSE have different patterns of innate immune infiltration. (A) Representative images of HMLER^S tumors recovered from N-HSE and A-HSE cohorts stained for MPO (brown) and counterstained with hematoxylin. Images were captured at 20x magnification. **(B)** Percent of cells that stained positively for MPO. Points represent individual tumors. Error bars represent mean and SD (N-HSE: n = 9; A-HSE: n = 8; unpaired, two-tailed T-test). **(C)** Representative images of HMLER^S tumors recovered from N-HSE and A-HSE cohorts stained for F4/80 (brown) and counterstained with hematoxylin. Images were captured at 20x magnification.

Therefore, if the innate immune system was playing a critical role driving the subclonal selection within HMLER^S tumors, then we expected to see an abrogation of the differential selection patterns between the N-HSE and A-HSE cohorts in NSG mice. In contrast to the nude mouse experiments, we saw that there was no significant difference between the number of detected CPs in N-HSE (average of 15.4 per HMLER^S tumor) and the A-HSE (average of 16.4 per HMLER^S tumor) cohorts when the HMLER^S tumors were allowed to form in NSG mice ($p=0.5721$, **Figure 3.7A,B**). In addition, the selection patterns appeared to be much more stochastic in NSG mice compared to nude mice (**Figure 3.7A**). Whereas in nude mice there were particular subclonal populations that were never detected in any HMLER^S tumors, in the NSG cohort every clone was detected in at least one tumor and there was a large amount of variability among mice within each systemic environment (**Figures 3.2D, 3.7A**). A repetition of this experiment yielded similar results (**Figure 3.8**).

Both the N-HSE and A-HSE NSG cohorts exhibited an enhancement of heterogeneity compared to that of the nude A-HSE cohort, with an average of 15.4, 16.4 and 12 clones detected, respectively. Strikingly, similar to the nude A-HSE cohort, tumors recovered from both cohorts of NSG mice also exhibited a reduction in neutrophil infiltration compared to the nude N-HSE cohort (**Figure 3.7C,D**). Together, these data suggest that a fully functional innate immune system is required to observe a reduction of heterogeneity in the N-HSE cohort compared to the A-HSE cohort and that reduced neutrophil infiltration appears to correlate with enhanced heterogeneity.

Figure 3.7. A functional innate immune system is required for enhanced heterogeneity in A-HSE HMLER^S tumors. (A) Representation of next-generation sequencing detected barcodes in individual HMLER^S tumors recovered from NSG mice in the N-HSE and A-HSE cohorts. Individual tumors are represented across rows and barcode identity is represented along columns. **(B)** Number of detected CPs per HMLER^S tumor. Each point represents an individual tumor. Bars represent mean and SD (N-HSE: n = 10, A-HSE: n = 10; Mann-Whitney test). **(C)** Representative images of HMLER^S tumors recovered from NSG N-HSE and NSG A-HSE cohorts stained for MPO (brown) and counterstained with hematoxylin. Images were captured at 20x magnification. **(D)** Percent of cells that stained positively for MPO in indicated cohorts. Points represent individual tumors. Error bars represent mean and SD (N-HSE: n = 9; A-HSE: n = 8; NSG N-HSE: n = 10; NSG A-HSE: n = 10; **** = p < 0.0001, Ordinary one-way ANOVA, Tukey's Multiple Comparisons Test).

Figure 3.7 (Continued). A functional innate immune system is required for enhanced heterogeneity in A-HSE HMLER^S tumors.



As the patterns of CP selection within HMLER^S tumors in the N-HSE and A-HSE nude mouse cohorts did not appear to be stochastic, we examined whether we could identify cell intrinsic properties of individual CPs that correlated with their presence or absence in HMLER^S tumors. We found that the *in vitro* proliferation kinetics rates or tumorsphere formation capacity of individual CPs did not correlate with the observed *in vivo* selection patterns (**Figure 3.8A,B**). For example, the most highly proliferative CP (CP 53) and the CP with the highest rate of tumorsphere formation (CP 2) both were only detected in 3/29 and 7/29 HMLER^S tumors, respectively (**Figures 3.2D, 3.5A,C**). The slowest proliferating CP (CP 70) and the CP with the lowest tumorsphere formation rate (CP 73) appear in HMLER^S at similar rates, and were detected in 2/29 and 16/29 tumor samples, respectively (**Figures 3.2D, 3.5A,C**).

We then used flow cytometry to evaluate the expression levels of two cell surface proteins that could have triggered innate immune clearance, HLA-1 and CD-47. We evaluated the expression level of both proteins on each CP in the presence and absence of IFN-gamma. We did not observe any trends in expression levels of either of these proteins that would account for the differential CP selection patterns that we observed *in vivo* (**Figure 3.8C,D and Figures 3.9-3.10**). Specifically, we did not see significantly higher or lower expression levels of either protein in CPs that were lost during tumor progression, compared to those that were maintained. We also found that all of the CPs were IFN-gamma responsive, suggesting that this characteristic could also not explain their differential behavior *in vivo*.

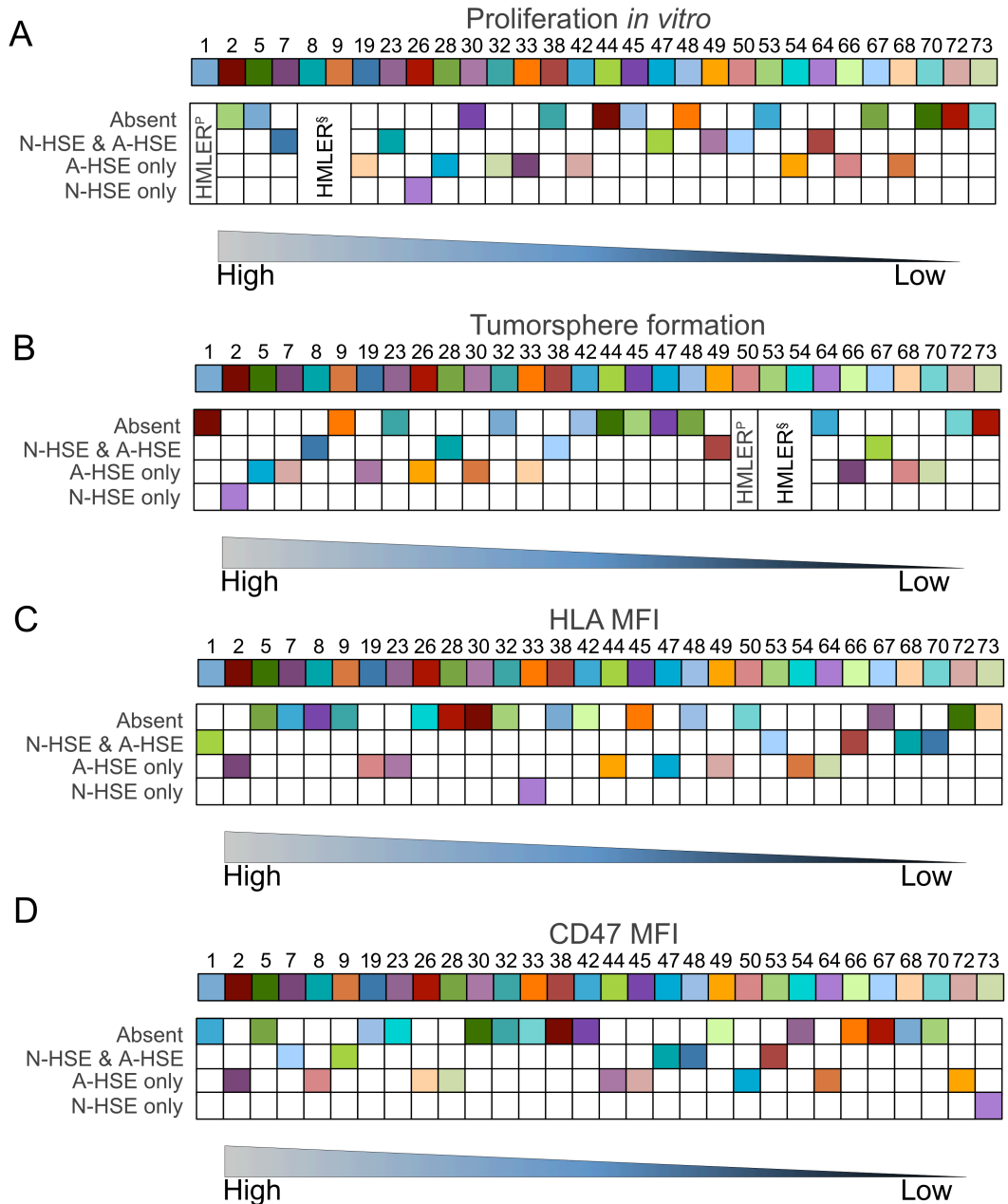


Figure 3.8. Cell intrinsic properties of individual CPs do not explain selection patterns observed *in vivo*. A-D: Individual CPs evaluated for their proliferation kinetics rates (A), tumorsphere formation rates (B), HLA-1 expression levels (quantified using median fluorescence intensity, MFI) (C), and CD47 expression levels (D). CP identities are represented using color and are placed in columns arranged from highest to lowest values from left to right. CPs were placed in the row that corresponds to their presence or absence from HMLER^s tumors in the N-HSE, A-HSE, or both environments in the *in vivo* selection experiment represented in **Figure 3.2**.

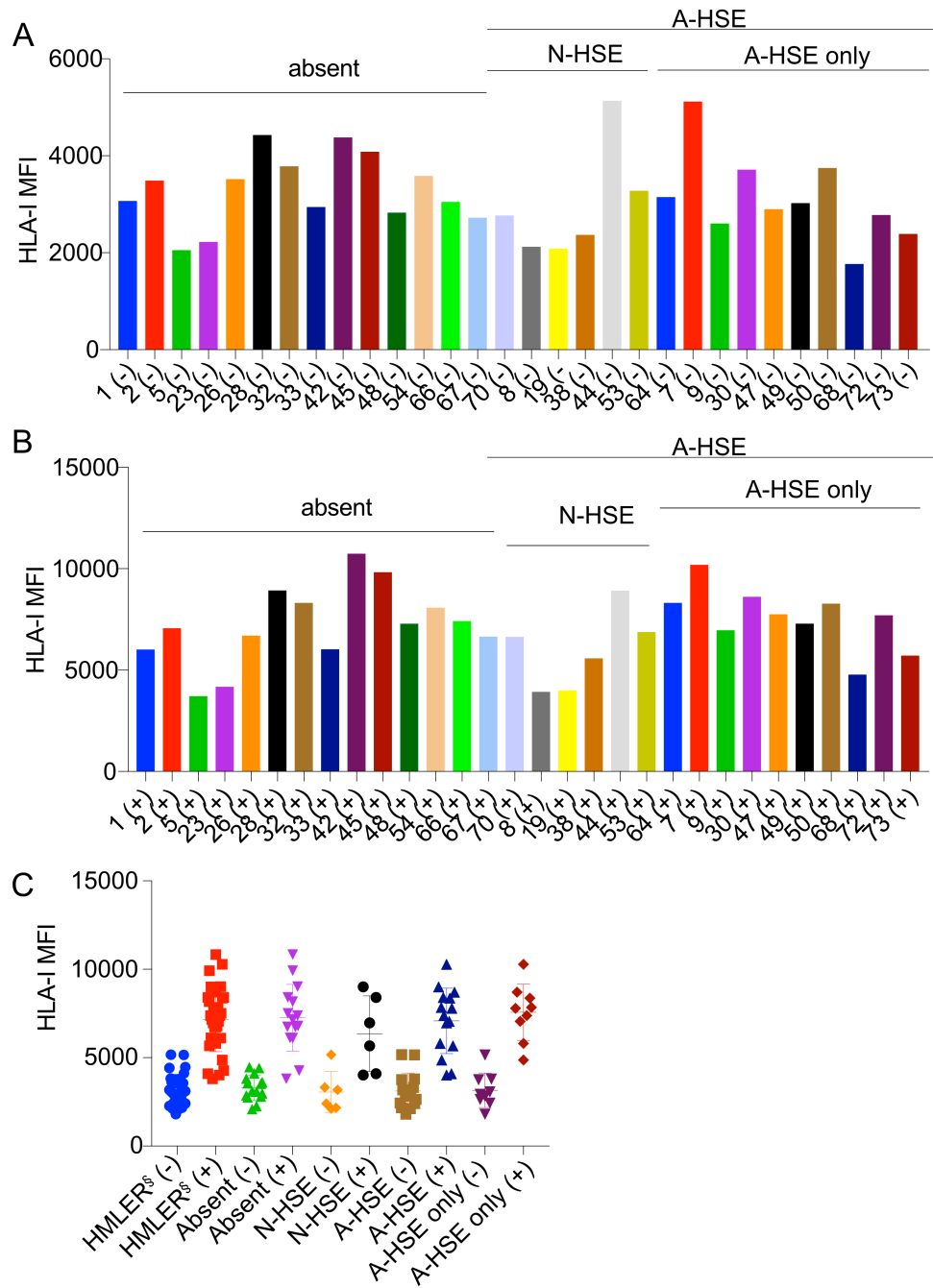


Figure 3.9. HLA-I expression levels on individual CPs do not correlate with *in vivo* selection patterns. (A-B) HLA-I median fluorescence intensity (MFI) values of CPs that had been cultured in the absence (A) or presence (B) of IFN-gamma. CPs are grouped based on whether they were detected in HMLER^S tumors in the N-HSE, A-HSE, or both environments in the *in vivo* selection experiment represented in **Figure 3.2**. (C) HLA-I MFI values of individual CPs that were cultured in the absence (-) or presence (+) of IFN-gamma. CPs are grouped based on whether they were detected in HMLER^S tumors in the N-HSE, A-HSE, or both environments in the *in vivo* selection experiment represented in **Figure 3.2**. Bar represents mean of that group.

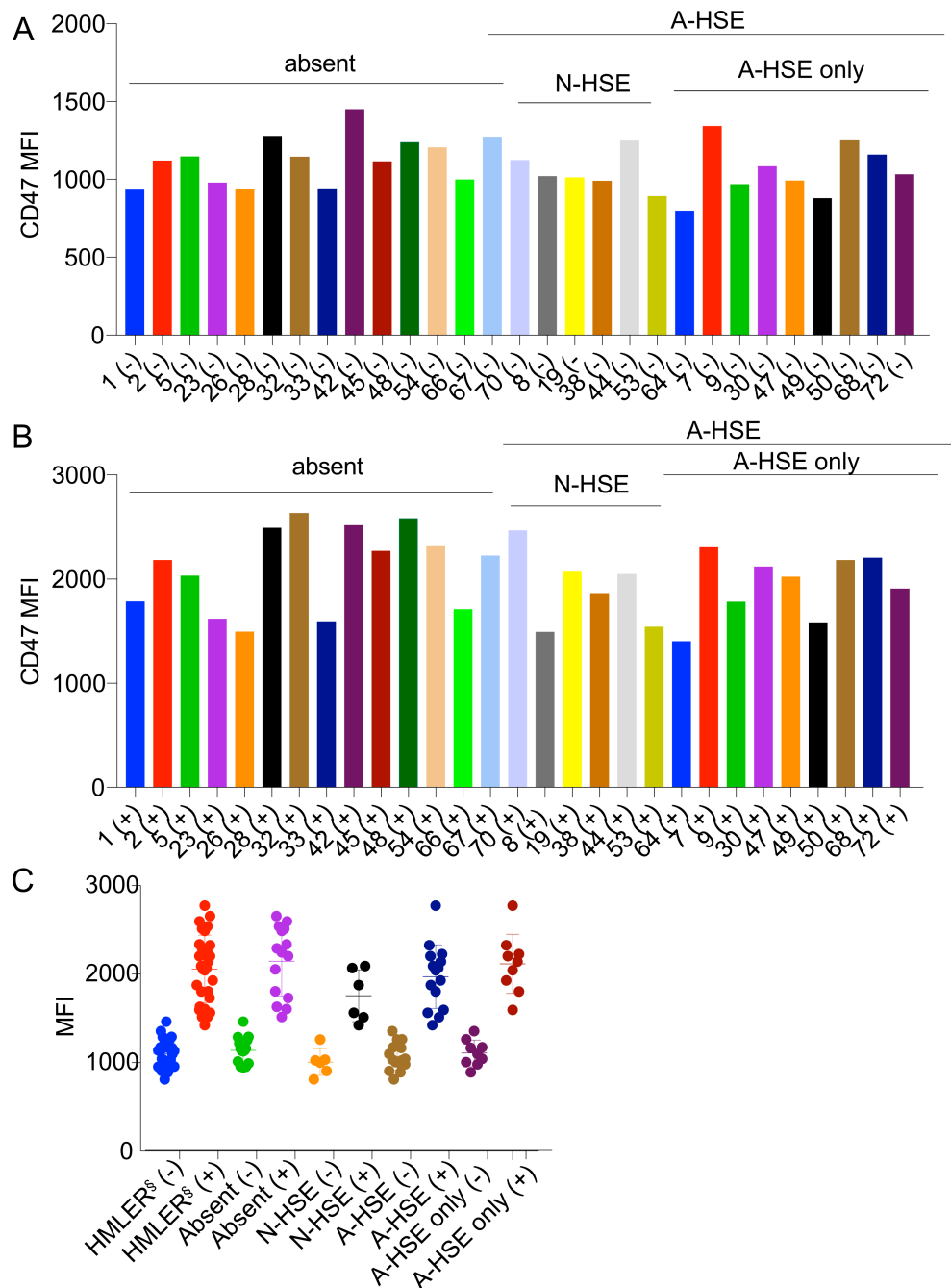


Figure 3.10. CD47 expression levels on individual CPs do not correlate with *in vivo* selection patterns. (A-B) CD47 median fluorescence intensity (MFI) values of CPs that had been cultured in the absence (A) or presence (B) of IFN-gamma. CPs are grouped based on whether they were detected in HMLER^S tumors in the N-HSE, A-HSE, or both environments in the *in vivo* selection experiment represented in **Figure 3.2**. (C) CD47 MFI values of individual CPs that were cultured in the absence (-) or presence (+) of IFN-gamma. CPs are grouped based on whether they were detected in HMLER^S tumors in the N-HSE, A-HSE, or both environments in the *in vivo* selection experiment represented in **Figure 3.2**. Bar represents mean of that group.

Finally, to test whether the CPs that had similar *in vivo* behaviors also shared common molecular features, we performed gene expression analysis of each CP using the LINCS L1000 profiling platform [75, 78]. Hierarchical clustering revealed that CP expression profiles did not correlate with whether or not CPs were selected for in any of the *in vivo* systemic environments (**Figure 3.11**). Collectively, these results indicated that none of the individual cell-intrinsic characteristics that we examined *in vitro* were capable of explaining the differential CP selection patterns that we observed in the N-HSE and A-HSE nude mouse cohorts. This is likely because the *in vivo* behavior of individual CPs is affected by its interactions with other CPs and the tumor microenvironment.

3.4.5 Subclonal populations can act cooperatively to generate unique cytokine and chemokine expression patterns

Previous studies have demonstrated the important role that clonal cooperation plays in breast cancer progression, including contributing to immune evasion [35, 36]. To evaluate whether the groups of CPs that were present in HMLER[§] tumors recovered from the N-HSE and A-HSE were able to cooperate to achieve unique biological behaviors, we generated CP subpools by creating mixtures containing equal numbers of each CP that was detected in HMLER[§] tumors in the N-HSE or A-HSE (**Figure 3.12A**, referred to as N-HSE[§] and A-HSE[§], respectively). We also generated a subpool that contained CPs that were found exclusively in the A-HSE HMLER[§] tumors, and were never detected in the

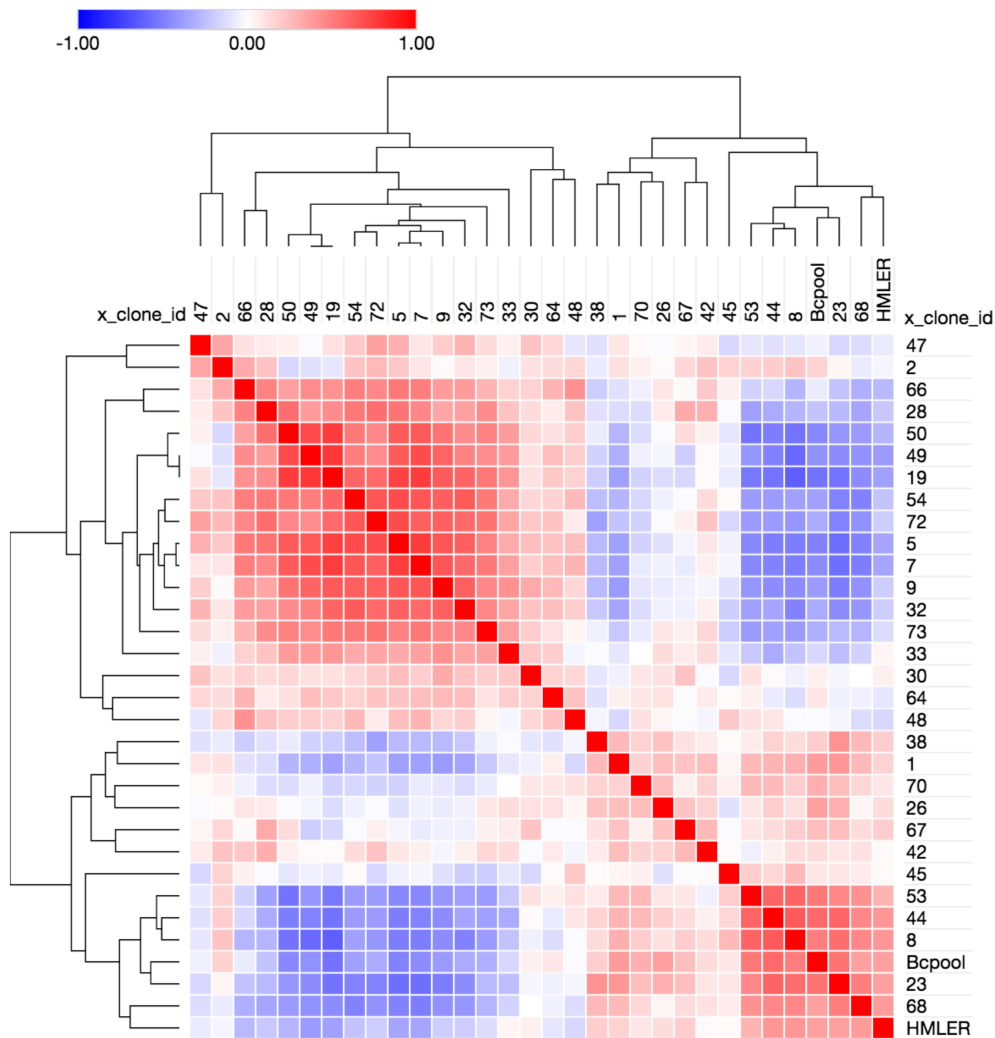


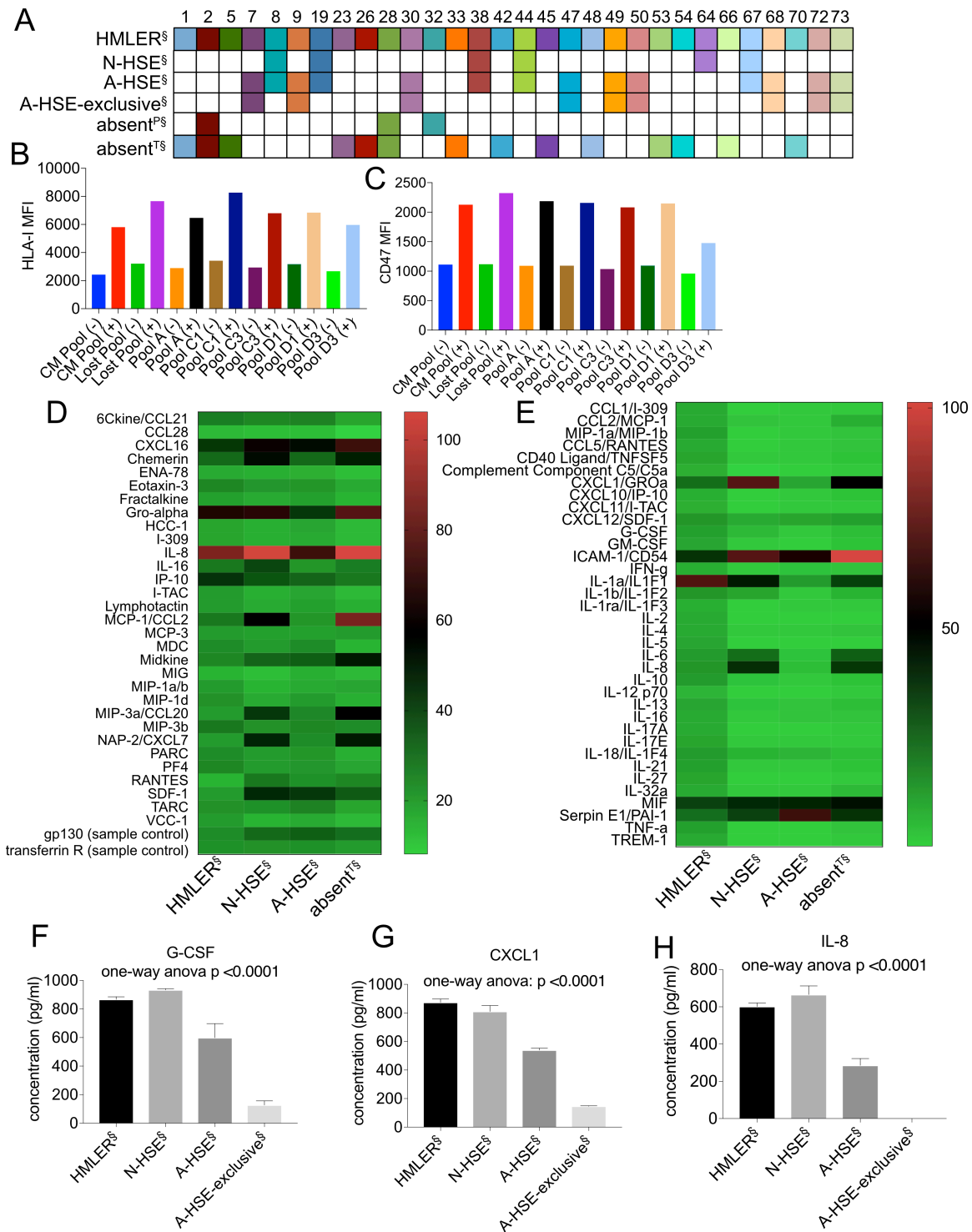
Figure 3.11. Hierarchical clustering of L1000 gene expression signatures of individual CPs. Hierarchical clustering of L1000 gene expression signatures was performed. Blue shading indicates lower levels of connectivity between gene expression signatures and red represents higher levels of connectivity. CP identities are indicated along rows and columns. HMLER^S is labeled as “Bcpool” and HMLER^P is labeled as “HMLER”.

naïve systemic environment (**Figure 3.12A**, A-HSE-exclusive[§]). Finally, we generated subpools that contained a subset of CPs or all CPs that were not detected in any HMLER[§] tumors (**Figure 3.12A**, partial-absent[§] (absent^{P§}) and total-absent[§] (absent^{T§})).

We did not observe any correlation between the *in vivo* behavior of CP subpools and their expression of either HLA-1 or CD-47 (**Figure 3.12 B,C**). However, cytokine and chemokine protein array analysis of conditioned media or cell lysates from CP subpools revealed that a number of proteins related to immune cell chemotaxis and function were differentially expressed and/or secreted by the HMLER[§] and CP subpools N-HSE[§] and A-HSE[§] (**Figure 3.12D,E**). Of particular interest to us was the observation that several factors involved in neutrophil mobilization and chemotaxis were downregulated in A-HSE[§] and A-HSE-exclusive[§] compared to the other subpools, as we observed decreased levels of neutrophil infiltration in HMLER[§] tumors in the A-HSE nude mouse cohort (**Figure 3.6A,B**). ELISA analysis of conditioned media samples confirmed that the A-HSE[§] and A-HSE-exclusive[§] subpools secrete significantly lower levels of G-CSF, CXCL-1 and IL-8 compared to both HMLER[§] and N-HSE[§] (**Figure 3.12F-H**). This suggests that the unique cytokine and chemokine secretion profiles of the CP subpools could help to shape the unique patterns of immune infiltration that were associated with the differential CP selection in the N-HSE and A-HSE HMLER[§] tumors.

Figure 3.12. HMLER[§] subpools exhibit unique patterns of cytokine and chemokine secretion. **(A)** HMLER[§] subpools that resembled HMLER[§] tumor clonal composition in the experiment represented in **Figure 3.2** were generated by mixing equal numbers of the indicated CPs. **(B)** HLA-I median fluorescence intensity (MFI) values of CP subpools that had been cultured in the absence (-) or presence (+) of IFN-gamma. **(C)** CD47 median fluorescence intensity (MFI) values of CP subpools that had been cultured in the absence (-) or presence (+) of IFN-gamma. **(D)** Heat map representing protein array quantifications of chemokine expression levels in conditioned media from the indicated HMLER[§] subpools. **(E)** Heat map representing protein array quantifications of cytokine expression levels in cell lysates of the indicated HMLER[§] subpools. **(F-H)** Expression levels G-CSF (F), CXCL1 (G), and IL-8 (H) in conditioned media of the indicated HMLER[§] subpools as measured by ELISA. Error bars represent SD (n = 3 per condition, one-way ANOVA).

Figure 3.12 (Continued). HMLER^S subpools exhibit unique patterns of cytokine and chemokine secretion.



3.4.6 HMLER[§] subpools have unique gene expression signatures

In addition to determining whether the systemic environment can affect the heterogeneity of responding tumors, we were also interested in whether there was functional significance to the particular CPs that were selected for in the N-HSE and A-HSE HMLER[§] tumors. To evaluate this, we performed L1000 gene expression profiling of the CP subpools and performed hierarchical clustering of the resultant gene expression signatures. Despite the fact that the clones contained within N-HSE[§] are also present in A-HSE[§], we found that these two subpools do not cluster together, suggesting that they have unique molecular profiles (**Figure 3.13A**). In contrast, the A-HSE-exclusive[§], which also contains CPs that are present in A-HSE[§], does cluster with A-HSE[§] (**Figure 3.13A**). This suggests that the addition of the CPs in A-HSE-exclusive[§] may contribute more strongly to the A-HSE[§] signature than the CPs in N-HSE[§]. Interestingly, when hierarchical clustering of the individual gene expression signatures of the CPs present within A-HSE[§] was performed, the clones within N-HSE[§] clustered together, and the clones within A-HSE-exclusive[§] clustered together (**Figure 3.13B**).

When the gene expression signatures of the CP subpools were queried for connectivity with gene expression signatures of a group of ~7,000 TCGA breast cancer samples and the connectivity of each pool signature to TNBC samples was examined, we found that A-HSE-exclusive[§] had notably more high ranking connections with TNBC patient samples than the other pool signatures

Figure 3.13. HMLER[§] subpools have unique gene expression signatures despite containing common CPs. (A) Hierarchical clustering of the HMLER[§] subpools L1000 gene expression signatures. **(B)** Hierarchical clustering of individual CP L1000 gene expression signatures within A-HSE[§]. **(C)** Tick plots showing the position of each TNBC sample in the ranked list of connectivities between all TCGA breast cancer samples (~7k) and the L1000 gene expression signature of each HMLER[§] pool. **(D)** Volcano plots showing Normalized enrichment score (Nes) and the corresponding $-\log(\text{FDR})$ for the indicated KEGG pathways for various HMLER[§] subpools.

Figure 3.13 (Continued). HMLER^S subpools have unique gene expression signatures despite containing common CPs.

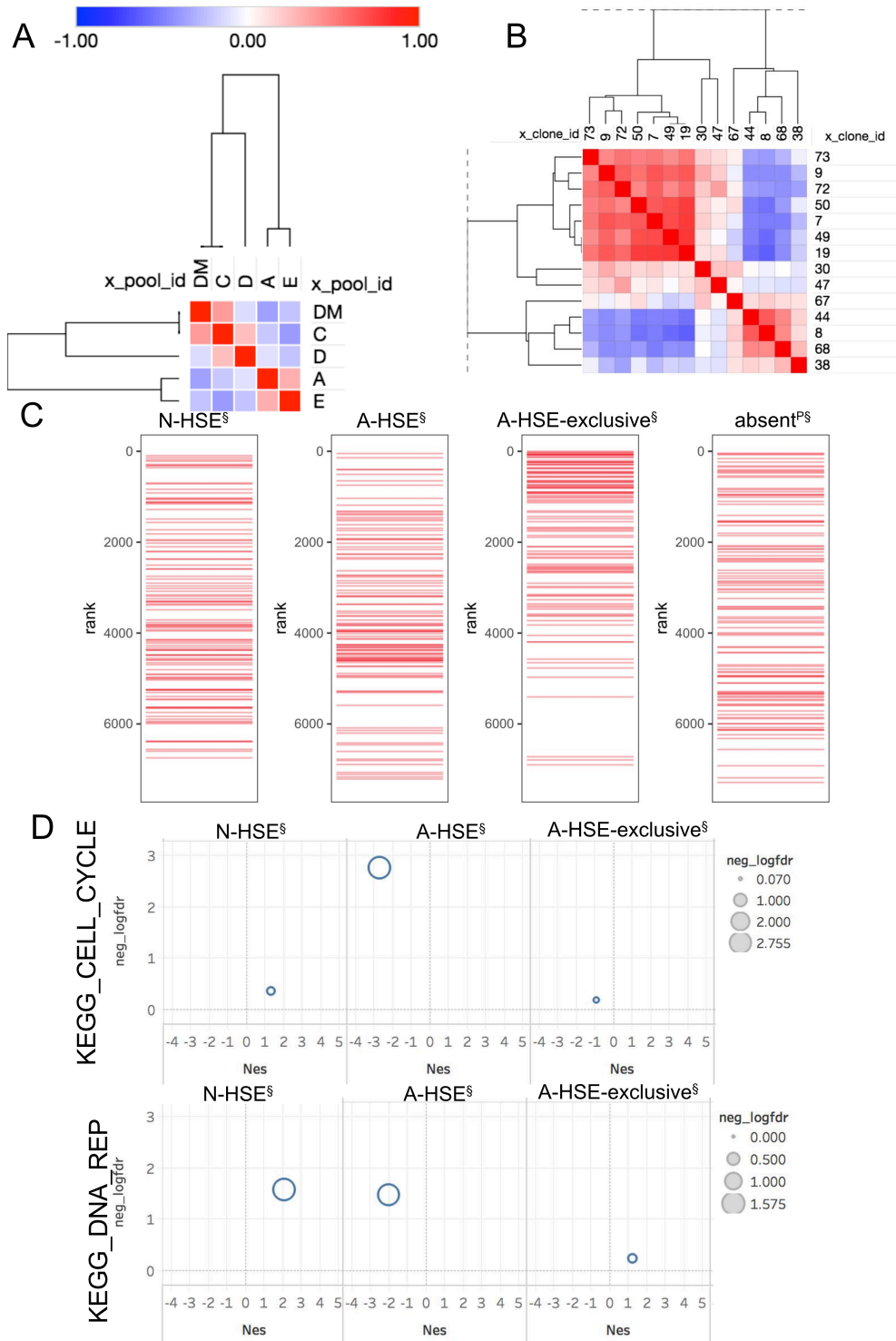


(Figure 3.13C). This suggests that A-HSE-exclusive[§], which contains CPs that exclusively appear in the TNBC tumor bearing A-HSE, more closely matches TNBC patient samples than the other pools.

Gene set enrichment analysis (GSEA) of the L1000 gene signatures revealed several instances where the A-HSE[§] and N-HSE[§] pool signatures revealed opposite patterns of connectedness to KEGG pathways that are relevant for cancer pathogenesis that were statistically significant **(Figure 3.13D)**. For example, whereas the N-HSE[§] pool signature exhibited significant connectivity to the KEGG Cell Cycle and KEGG DNA Replication pathways, the A-HSE[§] pool signature was negatively enriched for these pathway members **(Figure 3.13D)**. Also of interest was that the A-HSE[§] and A-HSE-exclusive[§] pool signatures differed from one another in these analyses, suggesting that these molecular profiles were the result of cooperation among all of the clones in A-HSE[§], and did not merely represent a majority contribution of the signaling pathways active in A-HSE-exclusive[§] CPs **(Figure 3.13D)**. Together, these data suggest that the unique patterns of clonal composition observed in HMLER[§] tumors in different systemic environments have unique molecular profiles that could have functional significance.

3.4.7 CPs selected in the A-HSE are less chemosensitive than those selected in the N-HSE

We next evaluated whether the unique gene expression patterns among the HMLER[§] subpools translated to differences in behaviors by evaluating in their

ability to respond to standard of care chemotherapeutics. The chemosensitivity of HMLER[§], N-HSE[§], and A-HSE[§] was evaluated by treating each pool with doxorubicin, 5-FU or paclitaxel for 72 hours and then evaluating the cell viability of each pool using the Cell Titer Glo assay. A-HSE[§] exhibited significantly higher rates of survival and decreased chemosensitivity compared to N-HSE[§] and this result was replicated in 4 separate repetitions of the experiment (**Figure 13.4A**). Strikingly, when the clonal composition of the surviving cells was analyzed, we found that all of the CPs were maintained during treatment with doxorubicin in HMLER[§], N-HSE[§], and A-HSE[§] at the IC50 dose. This suggests that the enhanced survival was not the result of the selection of particular chemoresistant CPs from among A-HSE[§], but that there is clonal cooperation taking place among the A-HSE[§] CPs that affords enhanced chemoresistance.

We examined whether this differential chemosensitivity was also relevant in an *in vivo* setting by injecting N-HSE[§] and A-HSE[§] into NSG mice and evaluating their response to treatment with doxorubicin. Treatment was initiated with either doxorubicin (1.5 mg/kg) or vehicle control (saline) when palpable tumors were observed in the majority of mice (**Figure 13.4B**). We found that while the final tumor mass in the N-HSE[§] cohort was significantly lower in the doxorubicin treated mice compared to the vehicle treated mice, there was no significant difference between the final tumor mass in the two A-HSE[§] cohorts (**Figure 13.4C**). This agrees with the *in vitro* observation that A-HSE[§] is less chemosensitive than N-HSE[§]. Together these results suggest that the directed selection that we observed in the A-HSE in nude mice was functionally

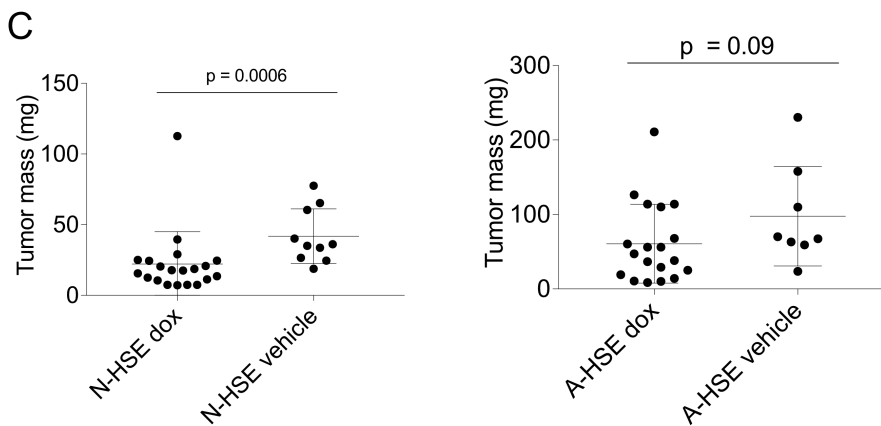
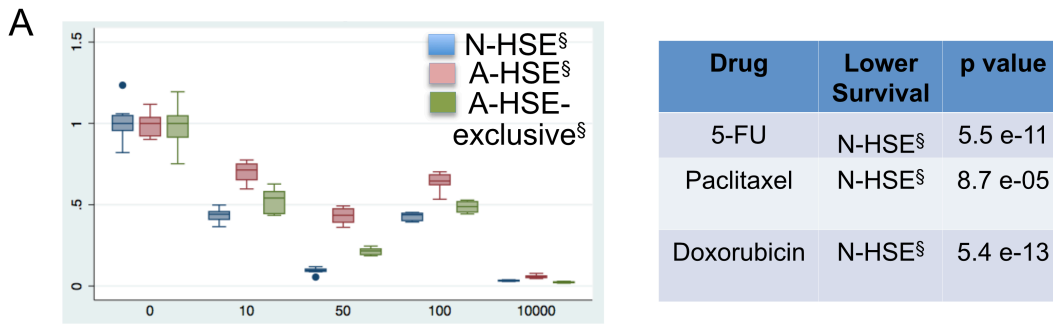


Figure 3.14. N-HSE[§] subpool is more chemosensitive than A-HSE[§] subpool both *in vitro* and *in vivo*. (A) Fractional survival (y-axis) of subpools following 72 hours of treatment with doxorubicin (concentrations along x-axis: 0 nM, 10 nM, 50 nM, 100 nM, and 10 μ M). A two-sided Wilcoxon rank sum test, stratified for dose, was used to compare fractional survival of N-HSE[§] to A-HSE[§]. (B) Experimental schema for *in vivo* doxorubicin study. (C) Final tumor mass for N-HSE[§] to A-HSE[§] tumors (N-HSE dox: n=20; N-HSE vehicle: n=10; A-HSE dox: n=19; A-HSE vehicle: n=8; Mann-Whitney test).

consequential and that the enhanced heterogeneity generated in this environment can lead to the development of a more aggressive TNBC tumor.

3.5 Discussion

The ability of the host systemic environment to drive cancer progression has become increasingly apparent in recent years [42-44, 46, 48, 52, 53, 79]. Numerous ways in which tumors are capable of activating the host systemic environment to perturb distant organs to generate pro-metastatic niches have been described. Our lab previously identified a model of host systemic activation, in which an aggressively growing BPLER tumor secretes osteopontin to trigger the outgrowth of distant, normally indolent breast cancer cell populations. This model system can be used to assay the response of a population of tumor cells to host systemic modulation. Osteopontin, which has been shown to be necessary for the host systemic activation in this model system, is used as a biomarker for tumor progression and is elevated in the serum of patients with metastatic disease, adding to the clinical relevance of this model [80-87]. Other models of host systemic activation, such as the systemic response to surgical wounding, have also been demonstrated to have clinical repercussions, such as an increase in observed metastases from around 6-18 months after surgical resection of the primary tumor [48, 88, 89].

Intratumoral heterogeneity, like host systemic activation, is known to contribute to disease progression and the formation of metastatic disease. Although heterogeneity has been well documented in the clinical setting, experimental systems to study it have been unavailable until recently and the mechanisms driving its generation and maintenance represent a gap in knowledge within the cancer biology field. Here we have shown that host systemic activation can shape intratumoral heterogeneity. This

represents the first demonstration, to our knowledge, of a mechanism through which functional heterogeneity is generated.

Our studies suggest that the innate immune system plays an important role in shaping intratumoral heterogeneity, but additional studies are necessary to decipher the exact mechanisms driving this phenomenon. The enhanced heterogeneity in the A-HSE environment was accompanied by a decrease in neutrophil and macrophage tumor infiltration, and the differential selection patterns were abrogated in NSG mice, which exhibit innate immune dysfunction. This lends the hypothesis that the BPLER tumor may be impairing innate immune function in the A-HSE, thereby generating patterns of intratumoral heterogeneity that resemble those seen in NSG mice. While neutrophils and/or macrophages could be directly involved in shaping the intratumoral heterogeneity, it is also possible that their interactions with other immune components (such as dendritic cells or NK cells, both of which are absent or defective in NSG mice) could be responsible.

A major strength of our molecular barcoding system is that after identifying populations of interest, we can extensively characterize those populations in both *in vitro* and *in vivo* settings. *In vitro* characterization of HMLER subpools suggested the CPs selected for in the A-HSE setting were able to act cooperatively in functionally consequential ways, including altered gene expression patterns and reduced chemosensitivity. Previous studies have demonstrated similar patterns of subclonal cooperativity within murine breast cancer models, and strikingly removal of a single cooperating population was enough to lead to tumor collapse [35, 36]. This has clinical implications for targeting intratumoral heterogeneity, as it may only be necessary to

target select critical clonal populations to disrupt the interactions that are required for malignant phenotypes.

As the causes of pathological host systemic activation become better understood, it also might be possible to interdict these processes, thereby decreasing heterogeneity and improving the associated patient outcome. For example, preclinical studies using the presence of a distant luminal tumor and surgery-induced systemic activation both demonstrated that the use of NSAIDs could temper the effects of systemic activation and slow disease progression [46, 48].

Together, this work provides a model for examining the causes of intratumoral heterogeneity and demonstrates that the systemic environment can drive clonal dynamics. The unique functional abilities that are acquired by groups of clonal populations that are selected for in an activated systemic environment highlight the importance of gaining a more thorough understanding of the functional consequences of intratumoral heterogeneity and identifying ways to target it therapeutically.

3.6 Conclusions

These studies demonstrate for the first time that host systemic activation can direct the selection of particular subclonal populations with functional relevance, highlighting the need for an increased understanding of heterogeneity and the processes that guide its formation. Biomarkers for patterns of host systemic activation that promote intratumoral heterogeneity, such as elevated cytokine levels or circulating immune cell populations, could be identified in the future, allowing for patient stratification. These findings may also be translatable to other instances of host systemic modulation, including the outgrowth of disseminated tumor cells in response to the surgical removal of a primary tumor or chemotherapy-induced inflammation. Importantly, previous studies have demonstrated that some dangerous types of host systemic activation can be reversed therapeutically, suggesting that future studies could yield pharmacological interventions that reduce intratumoral heterogeneity and improve patient prognosis.

Chapter 4

Generation of a molecular barcoding system to examine host systemic influences on heterogeneity in an immunocompetent model of breast cancer

*Some of the material described in this chapter may be submitted as part of a manuscript to a peer-reviewed journal.

Acknowledgements

This study was designed by Jessica Olive, with supervision from Dr. Sandra McAllister. Dr. Channing Yu and Aristotle Mannan (Golub Lab, Broad Institute) provided the lentiviral barcode vectors and performed barcode composition analysis using the PRISM system. Tyler Laszewski assisted with *in vivo* experiments. Andrea Clapp provided experimental assistance. The Harvard Biopolymers Facility performed next-generation sequencing. Dr. Rory Kirchner performed next generation sequencing data analysis. Jessica Olive performed all other experiments and data analysis.

4.1 Abstract

The innate and adaptive immune systems likely work together to direct clonal dynamics and shape intratumoral heterogeneity. Here we describe the development of a molecular barcoding system in an immunocompetent murine breast cancer model driven by transgenic overexpression of the *neu* gene. We demonstrate that the barcoded clonal populations are functionally heterogeneous and immunogenic. Preliminary *in vivo* selection experiments revealed differential patterns of clonal selection in wild-type mice and MMTV-*neu* transgenic mice that exhibit CD8⁺ T-cell tolerance towards the neu antigen. Interestingly, some clonal populations are replicably cleared in the transgenic systemic environment, suggesting that CD8⁺ T-cell independent mechanisms of immune editing are also active. Future studies using this barcoding system can be performed to uncover mechanisms driving intratumoral clonal evolution, including in the presence of therapeutic selective pressure.

4.2 Introduction

Human xenograft models are powerful tools for pre-clinical breast cancer studies, but they require the use of immunocompromised mouse models for tumor growth to occur [77]. By definition immunocompromised models do not have an intact immune system, with different immunocompromised strains lacking various combinations of immune functionality [77, 90]. The immune system has been shown to play an important role in disease development and progression, and the use of mouse models with compromised immune function is likely one of the reasons that preclinical discoveries often fail to ultimately achieve clinical success [40, 77].

We have demonstrated that innate immune components are involved in shaping intratumoral heterogeneity (**Chapter 3**), and we suspect that adaptive immune components also play an important role in this process. We previously developed molecular barcoding tools that allow for the tracking of clonal dynamics and the evaluation of intratumoral heterogeneity in human xenograft models (**Chapters 2-3**). Here, we sought to expand upon our previous discoveries by establishing a molecular barcoding system that was compatible for use in an immunocompetent murine breast cancer model and examining how a fully functional immune system is able to shape patterns of intratumoral heterogeneity.

Breast cancer can be modeled in an immunocompetent setting by utilizing transgenic models in which specific genetic perturbations lead to the formation of spontaneous mammary tumors. Additionally, murine breast cancer cell lines can be derived from these spontaneous tumors, which can then be used in murine allograft models. The McNeuA cell line was derived from a spontaneously arising breast tumor in

an MMTV-*neu* transgenic mouse, which overexpresses the HER2 oncoprotein [91].

Upon subcutaneous injection, McNeuA cells form tumors with 100% penetrance that are nearly identical to the MMTV-*neu* spontaneous tumors both structurally and histologically, but with significantly decreased latency [91].

Here we describe the generation of a collection of heterogeneous HER2⁺ clonal populations (HER2-CPs) derived from the McNeuA cell line. These HER2-CPs were stably infected with DNA barcodes to allow us to track the clonal dynamics of CPs in tumors recovered from wild-type (WT) FVB mice compared to FVB/N-Tg(MMTV-*neu*) mice, which have been previously reported to exhibit T-cell tolerance for the *neu* antigen and could therefore serve as a model of systemic immune modulation [92]. We found that tumors recovered from FVB-WT mice were less heterogeneous than those recovered from FVB/N-Tg(MMTV-*neu*) mice. Future work with this model system could help to delineate the unique roles that the adaptive and innate immune systems play in directing clonal dynamics and shaping intratumoral heterogeneity.

4.3 Materials and Methods

4.3.1 Cell lines

McNeuA cells ([91], a kind gift from Dr. Michael Campbell) were cultured in DMEM (Gibco) supplemented with 10% fetal bovine serum (FBS) and 1% Penicillin Streptomycin (Gibco) at 37C with 5% CO₂. To generate luciferase/GFP-positive populations (McNeuA-LucGFP), cells were infected with lentivirus generated from pLV-Luc-IRES-GFP viral plasmids (a generous gift from Dr. Robert Weinberg's lab) and then sorted for GFP-positive populations.

293T cells were cultured in DMEM (Gibco) supplemented with 10% FBS (Gibco) and 1% Penicillin Streptomycin (Gibco) at 37C with 5% CO₂. All cell lines were confirmed to be mycoplasma negative.

4.3.2 Single cell cloning

McNeuA-LucGFP cells were plated a density of 0.5 cells/well in a 96 well plate (Corning) to isolate single cells. The single cell seeding of each well was verified by tracking colony formation using a phase microscope during clonal expansion over the course of 1-3 weeks. Single cell clones that were confirmed to have expanded from single colonies were expanded in culture to establish the HER2-CPs.

A second round of single-cell cloning was performed for each HER2-CP to ensure that the number and location of the lentiviral insertion was clonal within each HER2-CP.

4.3.3 HER2-CP pooling

Equal numbers of 33 barcoded HER2-CPs were mixed to form the HER2-CP Pool (**Table 4.1**). Aliquots with 500,000 HER2-CP Pool cells were frozen down to serve as the starting point for future experiments.

4.3.4 Lentiviral infection

293T cells were transfected with 2.5 µg of lentiviral vector DNA (PLV-tdTomato was a generous gift from Dr. Robert Weinberg; barcode vectors were generous gifts from Todd Golub, Broad Institute, [68]), 2.5 µg PHR' (Addgene plasmid 8455), 1 µg VSVG (Addgene plasmid 8454) in Opti-MEM Reduced Serum Medium (Gibco) with Fugene HD (Promega). 48 and 72 hours following transfection, viral supernatants were collected and were filtered through a 40 micron syringe filter. Viral supernatants were stored at -80C and were mixed together prior to infection.

For lentiviral infection, McNeuA-CPs were infected with a 1:1 mixture of the appropriate viral supernatant in media with Polybrene (Sigma Aldrich). 72 hours after infection, selection with blasticidin was initiated to select for successful lentiviral barcode infections.

4.3.5 Genomic DNA preparations

Genomic DNA was extracted using the QiaAmp DNA Mini Kit (Qiagen) and was eluted in 200 µl of water. Final DNA concentration was quantified using a Nanodrop 8000 Spectrophotometer (Thermo Fisher).

Table 4.1. Barcodes present in HER2-CP Pool.

BC number	Barcode sequence
1	CTTTAATCTCAATCAATACAAATC
2	CTTTATCAATACATACTACAATCA
3	TACACTTTATCAAATCTTACAATC
4	TACATTACCAATAATCTTCAAATC
5	CAATTCAAATCACAATAATCAATC
7	CAATTCATTTACCAATTTACCAAT
8	AATCCTTTTACATTCACTTACTTAC
9	TAATCTTCTATATCAACATCTTAC
11	TACAAATCATCAATCACTTTAATC
12	TACACTTTTCTTTCTTTCTTTCTTT
13	CAATAAACTATACTTCTTCACTAA
15	ATACTTCATTCATTCATCAATTCA
17	CTTTAATCCTTTATCACTTTATCA
18	TCAAAATCTCAAATACTCAAATCA
21	AATCCTTTTCTTTAATCTCAAATCA
23	TTCAATCATTCAAATCTCAACTTT
24	TCAATTACCTTTTCAATACAATAC
26	TTACTCAAATCTCACTTTTTTCA
29	AATCTTACTACAAATCCTTTCTTT
30	TTACCTTTTATACCTTTCTTTTTAC
31	TTCACTTTTCAATCAACTTTAATC
32	ATTATTCACTTCAAATAATCTAC
33	TCAATTACTTCACTTTAATCCTTT
37	CTTTTCATCTTTTCATCTTTCAAT
38	TCAATCATTACACTTTTCAACAAT
40	CTTTCTACATTATTCACAACATTA
42	CTATCTTCATATTTCACTATAAAC
43	CTTTCAATTACAATACTCATTACA
44	TCATTTACCAATCTTTCTTTATAC
45	TCATTTCACAATTCAATTACTCAA
46	TACATCAACAATTCATTCAATACA
47	CTTCTCATTAACTTACTTCATAAT
48	AAACAAACTTCACATCTCAATAAT

4.3.6 Animal experiments

Experiments were performed in 6-8 week old female WT-FVB (referred to as the WT cohort) mice (Jackson) or FVB/N-Tg(MMTV-neu) (referred to as the transgenic cohort) mice (Jackson). All mouse cohorts received orthotopic mammary fat pad injections of 100,000 barcoded HER2-CP pool cells suspended in 20 μ l PBS. Tumors were measured using calipers once per week and tumor volume was calculated as $0.5 \times \text{length} \times \text{width}^2$.

Mice were euthanized via CO₂ inhalation when tumors reached 1.5 cm³. All mouse experiments were performed in accordance to federal laws and institutional guidelines and were approved by the Institutional Animal Care and Use Committee of Boston Children's Hospital and Brigham and Women's Hospital (Protocol 2017N000056).

4.3.7 Polymerase chain reaction

The barcode region of the lentiviral barcode vector was amplified using either primer set JO primer F/R (F: TGGAGCATGCGCTTTAGCAG; R: ATCGTTTCAGACCCACCTCC) or indexed primer sets (F: JH p05: ATC GTT TCA GAC CCA CCT CCC; R: JH p11-14 and JH p31-46, **Table 2.1**). PCR reaction mixtures contained 250 ng DNA, OneTaq 2x MasterMix (New England Biolabs), and 10 μ M each of F/R primers. The following PCR program was used to PCR amplify the template DNA: 94C for 30 seconds; repeat the following steps for 30 cycles: 94C for 20 seconds, 54C for 30 seconds, 68C for 20 seconds; final extension at 68C for 5 minutes). PCR products were purified using Agencort AMPure XP beads (Beckman Coulter) according

to the manufacturer's protocol and purified DNA was eluted in 20-40 µl water.

4.3.8 Illumina sequencing library preparation

Ligation-based Illumina library preparation was carried out by the Harvard Biopolymers Facility using an Integex Apollo 324 PrepX ILM using Kappa reagents, according to manufacturers' protocols. Ligation products were PCR amplified using primers against the P5/P7 Illumina adaptor regions.

For PCR-based Illumina library preparation samples that had been amplified using one of the barcode-indexed primer sets was amplified using an Illumina indexed primer set with regions that were complementary to the barcode lentiviral vector regions (F: JO p50, R: JO p65-p88, **Table 2.2**).

PCR reaction mixtures contained 100 ng DNA, OneTaq 2x MasterMix (New England Biolabs), and 10 µM each of F/R primers. The following PCR program was used to PCR amplify the template DNA: 94C for 30 seconds; Repeat the following steps for 15 cycles: 94C for 20 seconds, 54 C for 30 seconds, 68C for 20 seconds; final extension at 68C for 5 minutes. PCR products were purified using Agencort AMPure XP beads (Beckman Coulter) according to the manufacturer's protocol and purified DNA was eluted in 20-40 µl water.

4.3.9 Next generation sequencing data analysis

Next-generation sequencing data analysis was analyzed by Dr. Rory Kirchner by identifying index and barcodes in each read by searching for the pattern [8 base index]-

[17 bases]-ACGCGT-[24 base barcode]-CTGCAG and counting the index-barcode pairs.

4.3.10 Long-term proliferation kinetics assays

Individual HER2-CPs were plated in triplicate at a density of 100,000 cells/well in a 6-well plate (Corning). Cells were passaged and counted when they reached ~70% confluence (or approximately every 1-4 days) and were then replated in triplicate at a density of 100,000 cells/well. The assay was carried out for a total of 14 days.

Cell counts were used to extrapolate and estimate the overall proliferative capacity of each cell line at each passage point over the 14-day time period using the equation: $T_2 = (C_2/100,000) * C_1$, where T_2 is the extrapolated total number of cells, C_2 is the total cell count from passage 2, and C_1 is the total cell count from passage 1. This calculation was performed for T_3 through the final passage. The log of each total extrapolated cell count was plotted against time (days) and the slope of these lines were used to compare the proliferation kinetics rates of individual HER2-CPs.

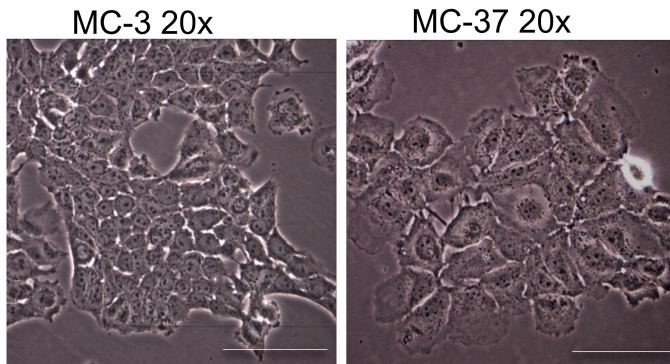
4.4 Results

4.4.1 Generation of a molecular barcoding system in an immunocompetent murine HER2⁺ breast cancer model system

In order to examine the role that the complete immune system plays in generating and influencing intratumoral heterogeneity, I established a molecular barcoding system in an immunocompetent murine model of HER2⁺ breast cancer. I generated a collection of 33 HER2-CPs from the McNeuA-LucGFP cell line, which was derived from a spontaneous breast tumor in a transgenic FVB/N-Tg(MMTV-neu) mouse [91]. The HER2-CPs exhibited morphological heterogeneity, presenting with a range of epithelial to mesenchymal phenotypes (**Figure 4.1A**). A unique, heritable molecular barcode was introduced to each HER2-CP using lentiviral infection. I confirmed the presence and identity of the barcode in each HER2-CPs using Sanger sequencing. The barcoded HER2-CPs exhibited functional heterogeneity in respect to their *in vitro* proliferation kinetics rates (**Figure 4.1B**).

Based on our preliminary analyses, I was satisfied that I had captured a heterogeneous group of HER2-CPs from the McNeuA-LucGFP parental population. I therefore proceeded and generated a HER2-CP Pool by mixing equal numbers of each HER2-CP. The HER2-CP Pool would serve as the starting point for each of our *in vivo* experiments.

A



B

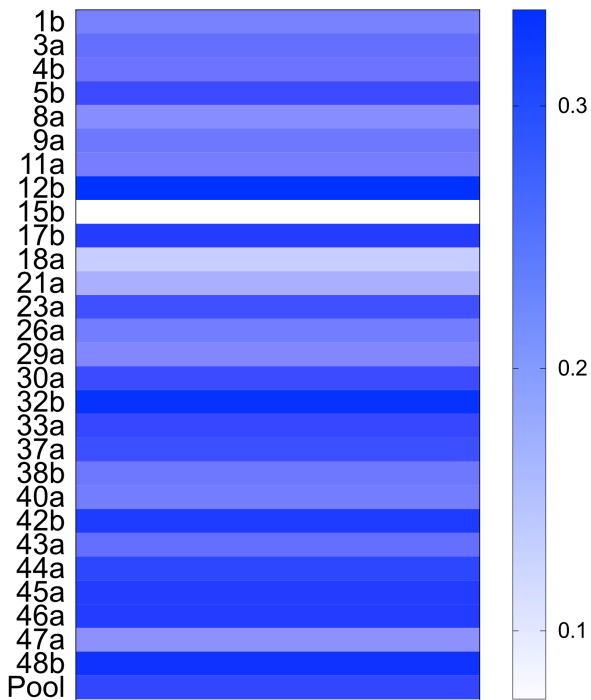


Figure 4.1. Generation of a functionally heterogeneous collection of barcoded HER2⁺ clonal populations. (A) Representative images of HER2-CPs with varying degrees of epithelial and mesenchymal morphologies. Scale bars = 100 μ m. **(B)** Heat map representing the heterogeneous rates of proliferation kinetics of HER2-CPs (listed on the left) and the HER2-CP Pool, as measured by the slope of total extrapolated cell counts over a 14-day proliferation assay.

4.4.2 Investigating the effects of host systemic activation in an immunocompetent murine breast cancer model

Previous work in our lab demonstrated that host systemic activation can lead to the selection of functionally relevant subpopulations of breast cancer cells in a pre-clinical human xenograft model (**Chapter 3**). We wished to expand these studies in an immunocompetent setting to allow for the examination of how both innate and adaptive immune components contribute to this process. It was therefore necessary to identify a model for systemic activation/modulation in a syngeneic model of murine breast cancer.

It had been previously demonstrated that FVB/N-Tg(MMTV-*neu*) mice injected with the McNeuA cell line display immunogenic T-cell tolerance to tumor cells displaying the *neu* antigen, leading to relatively higher rates of tumor formation and tumor mass when compared to those in WT-FVB mice (9). We decided to leverage the naturally occurring differential immune tolerance for the McNeuA cell line in these two mouse strains to model host systemic activation. Here, the transgenic strain represents an activated host systemic environment, in which the expression of the *neu* gene in the mammary gland causes systemic changes to the host environment. I hypothesized that the reduced immunogenicity of the McNeuA cells in the FVB/MMTV-*neu* mice would lead to increased intratumoral heterogeneity in tumors that form in the transgenic mice compared to the wild type FVB mice, similar to the enhancement of heterogeneity that we observed with host systemic activation in the human xenograft model (**Chapter 3**).

To test this hypothesis, we injected the HER2-CP Pool into the mammary fat pad of either WT-FVB or FVB/N-Tg(MMTV-*neu*) mice (n=10 mice per group, 20 mice

total). Animals were sacrificed when tumor volume reached 1.5 cm³. Mice in the transgenic cohort exhibited increased rates of tumor growth and had higher incidence than those in the FVB wild-type cohort (**Figure 4.2A**). Genomic DNA was extracted from recovered tumors and barcode composition was analyzed in tumors recovered from the transgenic and WT cohorts. I observed significantly enhanced heterogeneity in the tumors recovered from MMTV-neu/FVB mice compared to tumors recovered from FVB WT mice as measured by the average number of clones detected per tumor (**Figure 4.2B,C**). This suggests that systemic modulation of immunocompetent models of murine breast cancer can affect the degree of intratumoral heterogeneity, similar to what we have previously observed in human xenograft models.

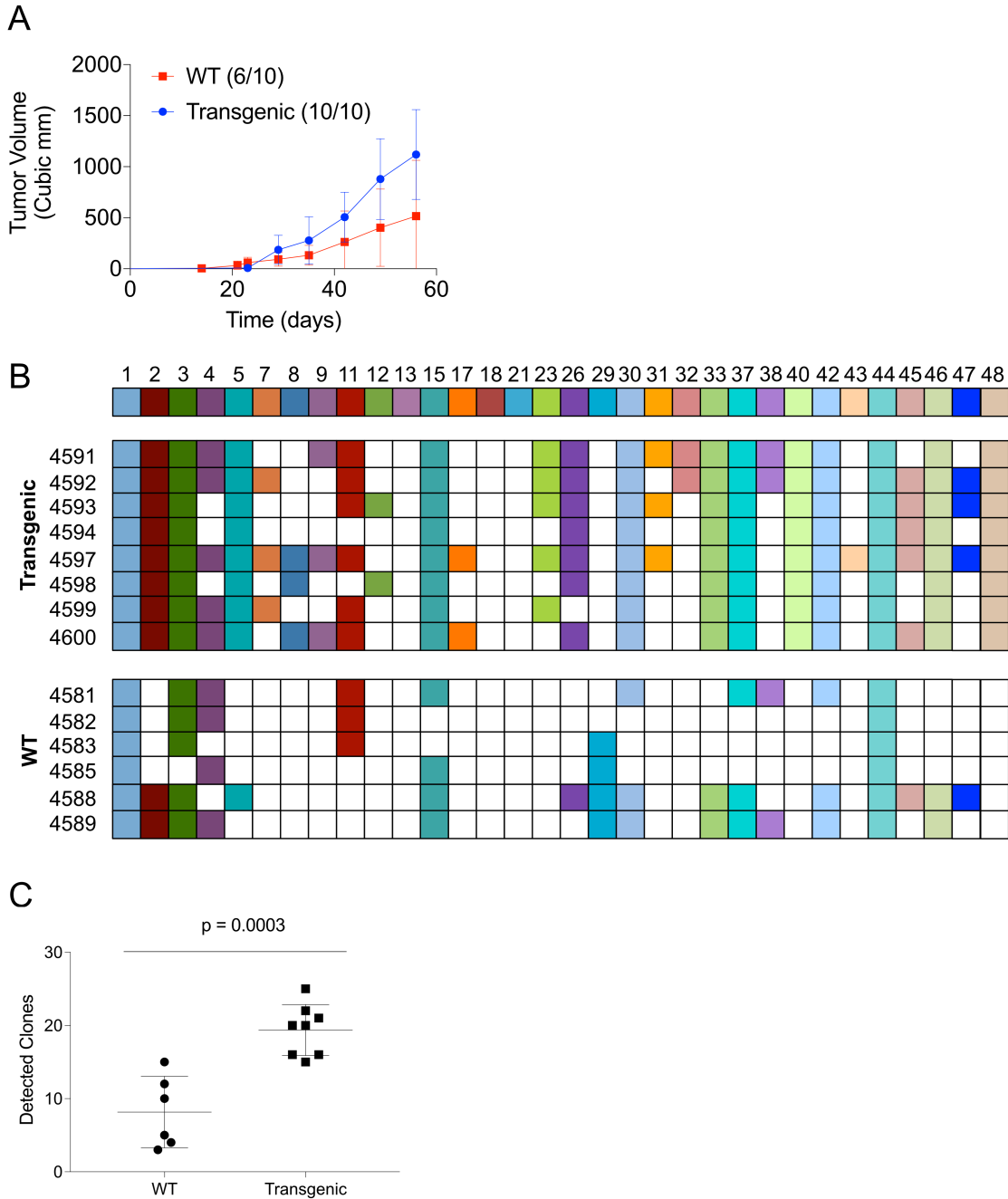


Figure 4.2. HER2-CPs form tumors with different incidence, growth kinetics, and levels of intratumoral heterogeneity in WT and MMTV-*neu* transgenic mouse strains. (A) Average tumor growth kinetics measurements from the WT and transgenic cohorts. Error bars represent SD. **(B)** Representation of HER2-CP composition of tumors recovered from mice in the transgenic and WT cohorts. Individual tumors are represented along rows and barcode identity is represented across columns. **(C)** Number of detected HER2-CPs per tumor. Each point represents an individual tumor. Bars represent mean and SD (WT: $n = 6$, Transgenic: $n = 10$; unpaired, two-tailed t-test).

4.5 Discussion

Human xenograft and syngeneic murine models of breast cancer both have strengths and weaknesses in their ability to model human breast cancer, and the synthesis of findings from the different modeling systems can provide valuable insights into human disease progression. Human xenograft models that use immunocompromised mouse strains have the advantage of employing human cancer cells that may serve as more accurate models of the cell intrinsic aspects of human breast cancer. However, they require the use immunocompromised hosts, which prevents accurate modeling of interactions between the tumor cells and the immune system, particularly adaptive immune components. Conversely, syngeneic models allow for the study of tumor models in hosts with full immune systems, but they utilize murine breast cancer cells, which may differ from human breast cancer cells.

Here we describe the establishment of a molecular barcoding system in a syngeneic model of murine breast cancer. This model system can be employed to complement and expand upon our studies of intratumoral heterogeneity in immunocompromised human xenograft models. We have demonstrated that the barcoded HER2-CPs generated from the McNeuA cell line (which was derived from a spontaneous MMTV-*neu*/FVB mammary tumor) are heterogeneous and able to be identified using a DNA barcode detection system.

In a pilot experiment in which we evaluated the clonal composition of tumors recovered from two strains of FVB mice (WT FVB and FVB/N-Tg(MMTV-*neu*)), we found that particular HER2-CPs that are typically cleared in orthotopic tumors in FVB-WT mice can be maintained in tumors recovered from transgenic mice (**Figure 4.2B**).

While this result is not unexpected based upon the T-cell tolerance against *neu* in the transgenic mice that has been previously described, the particular patterns of selection are very interesting. For example, there were some CPs whose pattern of representation did suggest a T-cell dependent clearance pattern (i.e. BC 48, which is present in all transgenic tumors and no WT tumors), but there were others that did not exhibit this same differential selection patterns.

There was a subset of HER2-CPs that were confirmed to be present at the time of injection that were not detectable in any tumors from either cohort (BCs 13, 18 and 21). It is possible that this represents a subset of clones that can be efficiently cleared by the innate immune system, which is believed to be unaffected by *neu* transgene expression. This could be explored in future experimentation by examining whether these HER2-CPs can be maintained in FVB transgenic models that lack specific components of the innate immune system.

Another interesting group of HER2-CPs are those that are present in every tumor in both cohorts (BCs 1 and 44). It would be interesting to evaluate whether these HER2-CPs have stably downregulated the expression of *neu*, suggesting that they are evading immune clearance in the WT setting by avoiding T-cell recognition of the corresponding antigen. Alternatively, these clones could be required for tumor formation and maintenance, and could be supported through mechanisms of clonal cooperativity [35, 36].

This barcoding system also has potential applications outside of investigations of tumor cell clonal dynamics in response to immune forces. For example, the barcoding system would be ideal for studying therapeutic resistance to chemotherapy and/or

HER2-targeted therapies. Future work could identify HER2-CPs that are maintained during treatment and that drive disease recurrence and progression. HER2-CPs that are identified as drivers of disease recurrence could then be characterized in order to identify the mechanisms that are driving resistance. This information could then be used to propose combinatorial therapies that may be used in future experiments to attempt to prevent the development of therapeutic resistance.

4.6 Conclusions

Here we describe the generation of a set of barcoded HER2⁺ clonal populations that can be used to examine intratumoral heterogeneity and clonal dynamics in an immunocompetent model of murine breast cancer. Initial characterizations of the HER2-CPs reveals that they are heterogeneous and can be identified both *in vitro* and *in vivo* using next-generation sequencing based detection methods. The HER2-CPs were used to demonstrate that modulations to the immune system, such as T-cell tolerance to tumor antigens, can affect the level of intratumoral heterogeneity of orthotopic tumors.

Future experimentation using this system could help to resolve the ways that the innate and adaptive immune systems work together to generate intratumoral heterogeneity. Additionally, this system could be used to examine clonal dynamics in response to other selective pressures, such as chemotherapy or targeted therapies.

Chapter 5

Accounting for tumor heterogeneity when using CRISPR-Cas9 for cancer progression and drug sensitivity studies

*The entirety of this chapter is under peer-review as a manuscript, on which Jessica Olive is co-first author, at the journal *PLOS One*.

Acknowledgements

This study was conceived and designed by Dr. Yuanbo Qin and Dr. Sandra McAllister. Dr. Yuanbo Qin developed the methodology. Experimental design and data acquisition were performed by Dr. Yuanbo Qin, Jessica Olive, and Dr. Molly DeCristo. Data analysis was performed by Dr. Yuanbo Qin and Jessica Olive. Jessica Olive wrote the manuscript. Tyler Laszewski, Frances Greathouse, and Dr. Hanna Starobinets provided technical assistance. We would like to thank Dr. Jessalyn M. Ubellacker and Dr. Jaclyn Sceneay for thoughtful discussion.

5.1 Abstract

Gene editing protocols often require the use of a subcloning step to isolate successfully edited cells, the behavior of which is then compared to the aggregate parental population and/or other non-edited subclones. Here we demonstrate that the inherent functional heterogeneity present in many cell lines can render these populations inappropriate controls, resulting in erroneous interpretations of experimental findings. We describe a novel CRISPR/Cas9 protocol that incorporates a single-cell cloning step prior to gene editing, allowing for the generation of appropriately matched, functionally equivalent control and edited cell lines. As a proof of concept, we generated matched control and osteopontin-knockout Her2+ and Estrogen receptor-negative murine mammary carcinoma cell lines and demonstrated that the osteopontin-knockout cell lines exhibit the expected biological phenotypes, including unaffected primary tumor growth kinetics and reduced metastatic outgrowth. Using these matched cell lines, we discovered that osteopontin-knockout mammary tumors were more sensitive than control tumors to chemotherapy in vivo. Our results demonstrate that heterogeneity must be considered during experimental design when utilizing gene editing protocols and provide a solution to account for it.

5.2 Introduction

CRISPR/Cas9 is a useful tool that has expanded our ability to define the role of particular factors in biological processes, including cancer biology [93, 94]. Oftentimes, studies employ the CRISPR/Cas9 system to generate loss- or gain-of-function mutations in a gene of interest and then look for a corresponding phenotypic change, indicating whether or not the targeted gene is necessary and/or sufficient for a particular behavior. Widely used protocols that employ CRISPR/Cas9 to generate genetically modified cell lines often require a subcloning and/or selection step in order to isolate a particular subpopulation in which the gene of interest was efficiently edited [95-99]. In order to correctly define the role that particular factors play, for example in cancer models, it is essential to use appropriately matched controls to compare to the edited subclone(s); however, such comparisons can be complicated by the widespread heterogeneity present in tumors and cancer cell lines derived from them.

The relevance and pervasiveness of genetic and functional heterogeneity within most cancer types has become particularly appreciated over the past decade [24, 30, 100]. It is now known that even supposedly clonal cancer cell lines are composed of subpopulations with widely differing phenotypes and functional characteristics [27, 101, 102]. Genetic and phenotypic heterogeneity has also been observed in other disease models, including bacterial antibiotic resistance and in the evolution of antiviral resistance [103-106].

Due to the inherent functional heterogeneity observed in most cancer cell lines, therefore, subcloning and selection steps employed in genetic editing

protocols can render the parental population an inappropriate control, as its behavior may differ from that of the selected subclonal population prior to gene editing. For example, if the aim of a study is to evaluate whether a particular gene product (protein) is relevant for primary tumor formation, it is common practice to compare the tumorigenicity of a knockout cell line with that of the parental cell line. However, if the selected subclonal population has an inherently different tumorigenic potential than the bulk parental population, it would be possible to incorrectly conclude that the knockdown of the gene of interest was responsible for any functional differences that are observed in any given biological assay.

Here we report a modified CRISPR/Cas9 targeting strategy to create appropriately matched knockout (KO) and wild-type (WT) control mammary carcinoma cell lines. We used these cell lines for both proof-of-concept and discovery studies. Our results demonstrate that it is critical to generate appropriately matched control and knockout cell lines in order to accurately evaluate the relevance of a protein of interest to cancer cell behaviors.

5.3 Materials and Methods

5.3.1 Cell lines

McNeu and Met-1 murine mammary carcinoma cells (kind gifts from Drs. Michael Campbell and Johanna Joyce, respectively) were cultured as previously described [91, 107]. Briefly, cells were cultured in DMEM (Gibco) media, supplemented with 10% fetal bovine serum (FBS) and 100 U/ml penicillin-streptomycin at 37°C under 5% CO₂. Human MDA-MB-435 cells were a generous gift from Dr. Robert Weinberg and were cultured in DMEM:F12 (1:1; Gibco), supplemented with 10% fetal bovine serum and 100 U/ml penicillin-streptomycin at 37°C under 5% CO₂. All cell lines were validated as mycoplasma-negative. Human cells were validated using short tandem repeat (STR) profiling (Molecular Diagnostics Laboratory at Dana-Farber Cancer Institute, Boston, MA). For mouse cells, the murine strain of origin was confirmed by short tandem repeat analysis (Bioassay Methods Group, NIST).

5.3.2 New gene editing protocol

Clonal subpopulations are generated from parental cell lines by sorting one single cell per well into 96-well plates using a FACSAria II cell sorter (BD Bioscience). Single cell-derived populations are subsequently allowed to proliferate for expansion. A single expanded clone is used for both control and co-transfection with the Cas9/GFP and sgRNA vectors. Select cell populations were seeded into 12-well plates overnight before transfection with 500ng pCas9_GFP and 500ng sgRNA expressing plasmids using FugeneHD (Roche).

48 hours after transfection, successfully transfected single cells are isolated by FACS sorting for GFP-positivity using a FACSAria II cell sorter (BD Bioscience) followed by recovery and expansion in 12-well plates for 2-3 days. At confluency, cells were collected for a second round of FACS sorting and single GFP-negative cells were sorted into individual wells in a 96-well plate to ensure that random Cas9/GFP integration did not occur. Following clonal expansion editing is validated using Sanger sequencing and phenotype verification is performed.

To generate luciferase/GFP-positive populations, cells were infected with lentivirus generated from pLV-Luc-IRES-GFP viral plasmids (a generous gift from Dr. Robert Weinberg's lab) and then sorted for GFP-positive populations.

5.3.3 Vector construction

The human codon-optimized Cas9 expression plasmid pCas9_GFP was a gift from Kiran Musunuru (Addgene plasmid # 44719). The sgRNA targeting mouse OPN exon 2 (5'-GTGATTTGCTTTTGCCTATT-3') driven by human U6 promoter was synthesized at Eurofin.

5.3.4 Evaluating target site modification by Sanger sequencing

OPN gene fragments were amplified with the primers OPN-F (5'-GACTTGGTGGTGATCTAGTGG-3') and OPN-R (5'-GCCAGAATCAGTCACTTTTCAC-3') using Phire Animal Tissue Direct PCR Kit (Thermo Scientific). The resulting PCR products were then submitted for Sanger sequencing (Macrogen USA).

5.3.5 Animals and tumor studies

Female FVB/NJ mice were purchased from Jackson Labs (stock no. 001800). NOD/SCID mice were maintained in-house under aseptic sterile conditions. All experiments were conducted in accordance with regulations of the Children's Hospital Institutional Animal Care and Use Committee (protocol 12-11-2308R) and the MIT committee on animal care (protocol 1005-076-08). All efforts were made to minimize animal suffering.

Murine mammary carcinoma cells were injected orthotopically, using a total of 10^5 or 10^6 McNeu cells, or 2.5×10^4 or 2.5×10^5 Met-1 cells implanted into the fourth mammary fat pad of 7-10 week old female FVB mice. Where indicated, either 1×10^5 or 1×10^6 cells of the McNeuA parental cell line were implanted subcutaneously. 2.5×10^5 human MDA-MB-435 cells were injected subcutaneously into 8-10 week old female NOD-SCID mice. Thereafter, tumors were monitored and measured using calipers with volume calculated as $0.5 \times \text{length} \times \text{width}^2$.

For the Met-1 metastasis assay, mice received tail vein injections with 1×10^6 cells of luciferase-labeled Met-1 cells suspended in 100 μl of sterile phosphate-buffered saline. Lung metastases were monitored weekly by bioluminescent imaging using the Spectrum Imaging System and Living Image software (Caliper Life Sciences, Inc.). Prior to imaging, mice were intraperitoneally administered 150 mg/kg D-luciferin (Perkin-Elmer) and were anesthetized using isoflurane inhalation. Luminescent signal was detected for the regions of interest as radiance (p/sec/cm²/sr) and analyzed using the Living

Image Software Version 4.1 (Caliper Life Sciences). Lungs were fixed and stained using Hematoxylin/Eosin and metastases were classified as multi- or single-focal and were counted manually on 3 separate sections spaced 50 microns apart per mouse. Total lung area was quantified using Cell Profiler and metastases counts were normalized total lung area.

5.3.6 Chemotherapy studies

For AC-T chemotherapy trials, 2.5×10^5 Met-1 Luc/GFP cells were injected into the mammary fat pad of 6–8-week-old female FVB mice. Doxorubicin (Teva), paclitaxel (Hospira), and cyclophosphamide (Sigma) were diluted in PBS for *in vivo* experiments. Mice were treated with two to four doses of 5 mg/kg doxorubicin, 10 mg/kg paclitaxel, and 120 mg/kg cyclophosphamide administered every two weeks. Doxorubicin was administered via retro-orbital injection, and paclitaxel and cyclophosphamide were administered via intraperitoneal injection.

For studies investigating the role of OPN in chemotherapeutic response, 2.5×10^4 WT or OPN KO tumor cells were injected into the mammary fat pad of 6–8-week-old female FVB mice. When established tumors reached 60–80 mm³ in volume, treatment was initiated. Four treatment arms were included: vehicle control (PBS) on WT or OPN KO cohorts or one dose of paclitaxel (10 mg/kg), doxorubicin (5 mg/kg) and cyclophosphamide (120 mg/kg) by intraperitoneal injection (paclitaxel and cyclophosphamide) and retro-orbital injection (doxorubicin) on WT or OPN KO cohorts. Tumor growth was monitored using

caliper measurements. Average tumor mass at sacrifice was measured and is presented as the average \pm standard error of mean.

5.3.7 Osteopontin ELISAs and western blotting

To assess circulating secreted murine osteopontin (mOPN) or human osteopontin (hOPN) protein levels, whole blood was collected in EDTA-coated tubes (VWR) and centrifuged at 1.5xg for 8 minutes to isolate plasma. mOPN and hOPN concentrations were determined by ELISA according to manufacturer's instructions (R&D) and analyzed using a plate reader (Molecular Device).

To quantify secreted mOPN levels in conditioned medium, cells were grown to 80–90% confluence in growth medium containing 10% FBS. Then the medium was replaced with serum-free medium and was collected 24 hours later. mOPN levels in conditioned media were quantified by ELISA or western blotting.

Whole cell lysates were prepared following culture in the presence or absence of brefeldin A (used to prevent the secretion of OPN and ensure detection of protein expression). Cell lysates or concentrated conditioned medium were subjected to SDS-PAGE on 12% gels and then transferred onto a polyvinylidenedifluoride membrane, which was incubated with mouse anti-OPN (final dilution: 1:200, Clone AKm2A1, Santa Cruz Catalog # sc-21742, mouse monoclonal antibody raised against recombinant OPN of mouse origin, references with validation available on manufacturer's datasheet) antibody at 4C overnight. After being washed, membranes were incubated with horseradish

peroxidase-conjugated anti-mouse IgG for 1 hour. The enzyme bound to OPN was visualized using the SuperSignal™ West Pico Chemiluminescent kit (ThermoFisher). The blot was then stripped and incubated with rabbit anti-mouse β -actin antibody as a loading control (final dilution: 1:1000, Rockland Catalog # 600-401-886, rabbit polyclonal antibody raised against human beta-actin,, references with validation available on manufacturer's datasheet).

5.3.8 Immunohistochemistry, immunofluorescence and microscopy

Formalin-fixed, paraffin embedded tissues were sectioned onto ProbeOn Plus microscope slides (Fisher Scientific) and immunohistochemistry was performed as described [47]. For the OPN immunohistochemistry studies, anti-OPN (final dilution: 1:200, Maine Biotechnology Services Catalog #, MAB197P, mouse monoclonal antibody raised against recombinant OPN of human origin, [108]) was used and was detected using the Vector ABC kit (Vector Laboratories, Burlingame, CA, USA). For immunofluorescence, anti-OPN (final dilution: 1:50, Clone AKm2A1, Santa Cruz Catalog # sc-21742, mouse monoclonal antibody raised against recombinant OPN of mouse origin, references with validation available on manufacturer's datasheet) was used and was detected using a goat anti-mouse IgG AF549 conjugated secondary antibody (final dilution: 1:1000, Invitrogen Catalog # A11032, polyclonal, references with validation available on manufacturer's datasheet). Nuclei were counterstained with DAPI (Invitrogen). Images were captured with identical exposure and gain using a Nikon Eclipse Ni microscope.

5.3.9 *In vitro* chemosensitivity studies

4,000 Met-1 cells were plated in quadruplicates in 96-well plates containing growth media. The next day, vehicle (PBS) or chemotherapy (doxorubicin: .33 nM - 2.2 μ M; paclitaxel: 14 μ M – 160 μ M) was added to the plate and incubated for 72 hours. ATP levels were quantified as a surrogate measure for viability (CellTiter-Glo, Promega) using a luminometer (Perkin-Elmer).

5.3.10 *Statistical analyses*

Data are represented as mean \pm SEM and analyzed by ANOVA, Student's t-test, and/or Mann-Whitney test as indicated using GraphPad Prism 7.0, unless otherwise stated. $P < 0.05$ was considered statistically significant. Error bars represent standard deviation unless otherwise indicated.

5.4 Results

5.4.1 Selection of Her2+ and Estrogen receptor-negative mammary carcinoma models

We aimed to design an approach that would enable us to generate appropriately matched control and CRISPR/Cas9 knockout cell lines, while taking into account the inherent functional heterogeneity present in nearly all breast tumors and tumor-derived cancer cell lines. We hypothesized that results from studies employing standard CRISPR/Cas9 approaches, which often require a subcloning and/or selection step, would be confounded by subclonal functional heterogeneity.

As a proof of concept, we chose to study Osteopontin (OPN), a protein that we have studied previously and that is relevant for breast cancer metastasis [47, 83, 109-114]. OPN plays an important role in metastasis and survival in many pre-clinical cancer studies, and is positively associated with metastasis as well as reduced progression-free and overall survival in breast cancer patients [83, 114, 115]. Additionally, OPN has been shown to play a role in chemoresistance in some cancer types [109, 111, 112, 116-118], but it is unclear whether this is also true of breast cancer.

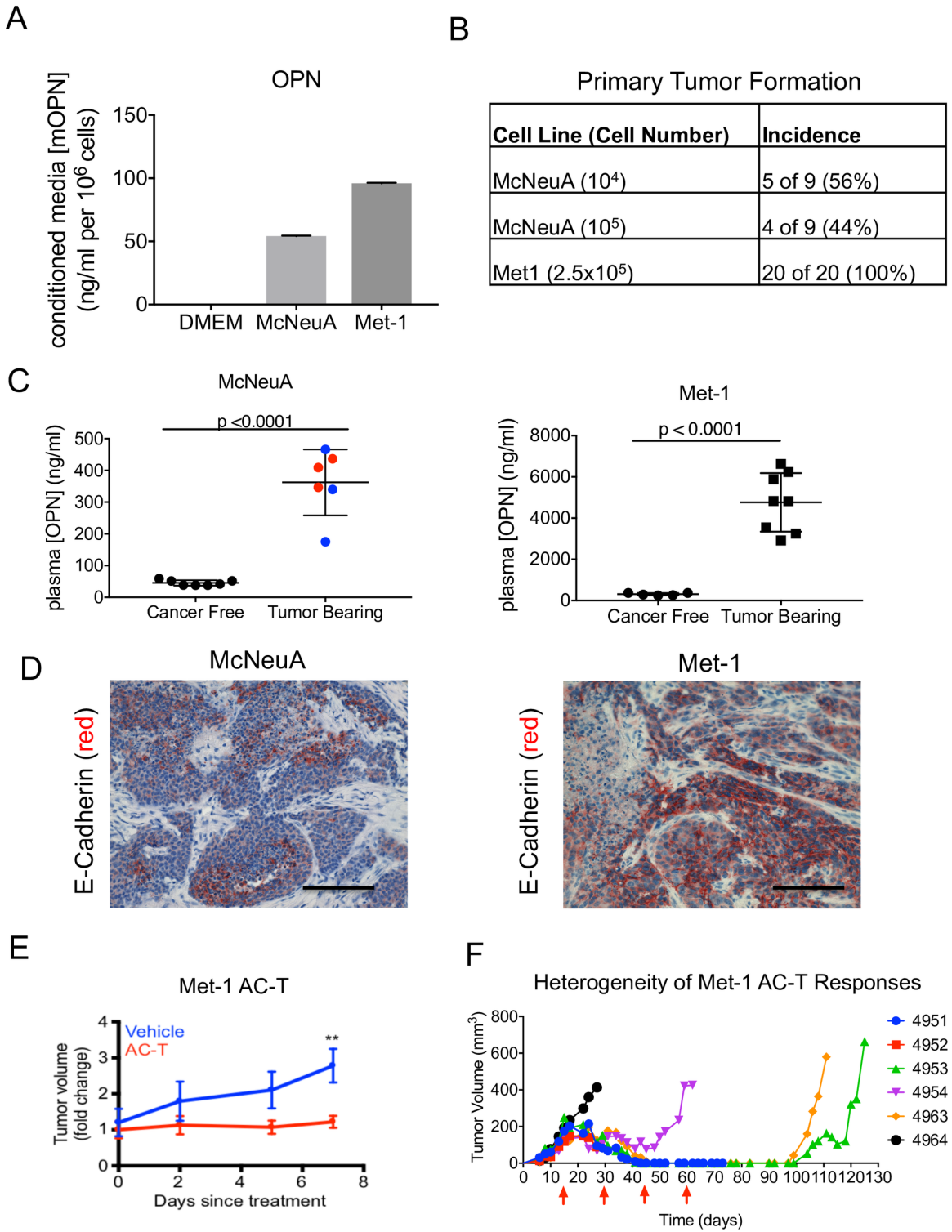
Hence, we determined that the breast cancer models that we would employ must meet the following criteria: secretion of detectable levels OPN both *in vitro* and *in vivo*, capacity to form primary and metastatic tumors *in vivo*, evidence of heterogeneity, and responsiveness to chemotherapy.

Transgenic mice that specifically overexpress oncogenic proteins in the mammary fat pad are commonly employed both for the study of spontaneous breast tumors and as a source for murine breast cancer cell lines that can be allografted orthotopically in immunocompetent animals. In this study, we utilized two such murine breast cancer cell lines: McNeuA, a HER2⁺ breast cancer cell line derived from a spontaneously arising mammary carcinoma in a MMTV-*neu* transgenic mouse [91], and Met-1, an estrogen receptor-negative (ER⁻) breast cancer cell line derived from a mammary carcinoma in a MMTV-PyMT transgenic mouse (FVB/N-Tg(MMTV-PyVmT) [107].

Characterization of McNeuA and Met-1 cell lines demonstrated their potential as models for this study, as they secreted detectable levels of OPN in culture as measured by ELISA (**Figure 5.1A**). Both cell lines efficiently formed primary tumors following injection into FVB mice (**Figure 5.1B, Figure 5.2A**). While both cell lines formed tumors that had an average mass of 2.3 g at the experimental end points (30 days for Met-1 and 90 days for McNeuA, or when tumors reached 1.5 mm³, **Figure 5.2B**), the McNeuA tumors exhibited more variability in both their tumor incidence and final tumor mass. Additionally, previous studies have demonstrated that both of these cell lines are capable of forming lung metastases [91, 107].

Figure 5.1. Phenotypic and functional heterogeneity of McNeuA and Met-1 breast cancer cells. **(A)** Concentration of murine OPN (mOPN; ng/ml per 10^6 cells) in 24-hr conditioned medium of McNeuA and Met-1 murine mammary carcinoma cells represented as mean \pm SD. There was no detectable mOPN in the control cell-free medium (DMEM) (2 technical replicates per group). **(B)** Incidence of tumor formation following injection of indicated numbers of McNeuA or Met-1 cells into cohorts of FVB mice. **(C)** Plasma mOPN concentration (ng/ml) in indicated cohorts of mice at experimental end points of 84 days (McNeuA) and 30 days (Met-1). For McNeuA tumor-bearing mice, blue data points represent 10,000 cells injected, red data points represent 100,000 cells injected; n=6-7 for McNeuA cohorts; n=5-8 for Met-1 cohorts. Error bars represent SD; statistical significance evaluated using unpaired, two-tailed Student's t-test. **(D)** Representative images of immunohistochemical staining for murine E-cadherin (red) on recovered McNeuA and Met-1 tumors. Cell nuclei were counterstained with hematoxylin (blue). Scale bars = 100 μ m. **(E)** Response of orthotopic Met-1 GFP/Luc tumors to single dose combination doxorubicin (5 mg/kg), paclitaxel (10 mg/kg) and cyclophosphamide (120 mg/kg) (AC-T), n=5-8 tumors/group. Ordinate represents time (days) following treatment. Error bars represent SEM; two-way ANOVA Sidak's multiple comparisons test; *p<0.01. Representative of 3 independent experiments. **(F)** Growth kinetics of individual orthotopic Met-1 Luc/GFP tumors in mice injected with 2.5×10^5 tumor cells at the experiment initiation, subsequently receiving 4 biweekly AC-T doses (red arrows). Numbers and colors represent individual mice.

Figure 5.1 (Continued). Phenotypic and functional heterogeneity of McNeuA and Met-1 breast cancer cells.



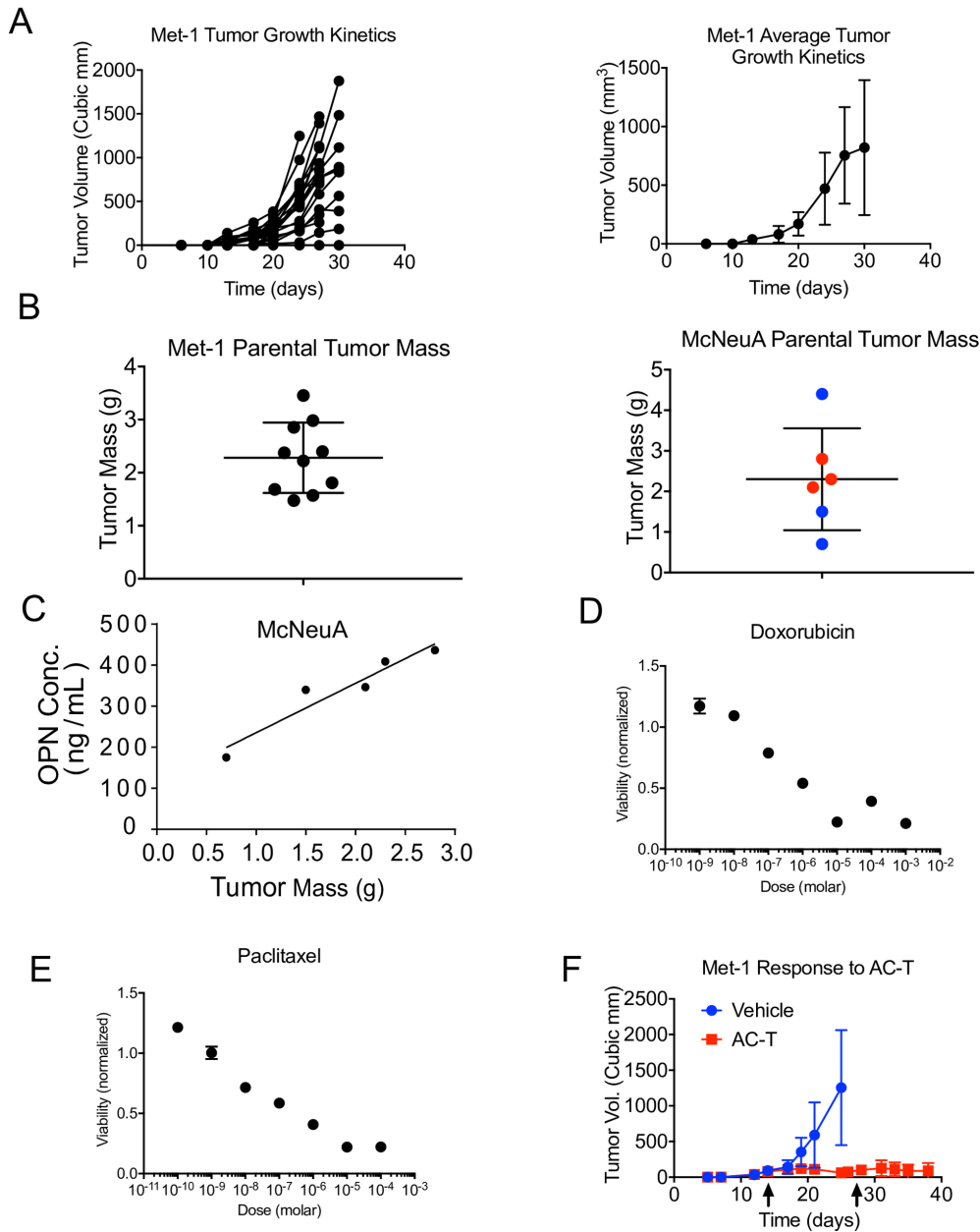


Figure 5.2. Met-1 and McNeuA Parental Tumor Characteristics. (A) Individual and average tumor growth kinetic rates from FVB mice orthotopically injected with 2.5×10^5 Met-1 cells. Error bars represent SD. (B) Endpoint tumor masses of mice injected with 10^5 (red) or 10^6 (blue) McNeuA cells or 2.5×10^5 Met-1 cells. Error bars represent SD. (C) Circulating plasma osteopontin (OPN) levels were measured using ELISA and were plotted against the primary tumor mass in the corresponding animal. (D,E) Viability of Met1 GFP Luc cells treated in vitro with various doses of doxorubicin and paclitaxel for 72 hours. Representative of three independent experiments. Error bars represent SEM. (F) Tumor growth kinetics of the Met-1 Luc/GFP parental cells injected orthotopically into FVB mice at 2.5×10^5 cells treated with two bi-weekly doses of either vehicle (blue, n=6) or AC-T (red, n=8). Error bars represent SEM.

In both models, the tumor bearing mice had significantly elevated plasma levels of OPN relative to cancer-free cohorts whereby average OPN levels were 8-fold and 15-fold higher in the McNeuA and Met1 tumor-bearing mice, respectively, at end stage (**Figure 5.1C**). Interestingly, plasma OPN levels positively correlated with the final tumor mass in mice bearing the McNeuA tumors (**Figure 5.2C**). Immunohistochemical analysis of the recovered tumors revealed intratumoral heterogeneity for the epithelial marker, E-cadherin (**Figure 5.1D**).

We next tested responsiveness of Met-1 mammary carcinoma to combination doxorubicin (A), cyclophosphamide (C), and paclitaxel (T) chemotherapy, AC-T, a standard of care chemotherapy regimen for breast cancer patients with ER-negative disease. We first tested the sensitivity of Met-1 cells to doxorubicin and paclitaxel in vitro and performed an initial in vivo experiment to identify a therapeutically relevant, well-tolerated combinatorial dose of AC-T.

Treatment with both doxorubicin and paclitaxel significantly decreased viability of Met-1 cells in vitro (**Figure 5.2D,E**). In vivo, a combination dose of doxorubicin (5 mg/kg), paclitaxel (10 mg/kg), and cyclophosphamide (120 mg/kg) was well tolerated (no weight loss; data not shown) and had a cytostatic effect on Met-1 tumor growth (**Figure 5.1E, Figure 5.2F**).

To more closely emulate the clinical dosing regimen of AC-T chemotherapy, mice with Met1 mammary carcinoma were administered AC-T every 2 weeks for 4 cycles. Interestingly, individual mice bearing Met-1 tumors

exhibited differential responses to treatment, and in some cases, mice that initially experienced complete tumor regression eventually recurred (**Figure 5.1F**).

Collectively, our analyses indicated that the McNeuA and Met-1 cell lines met our criteria of OPN secretion *in vitro* and *in vivo*, efficient formation of primary orthotopic tumors, metastatic capacity, chemosensitivity, and evidence of phenotypic and functional heterogeneity *in vivo*. Hence, the McNeuA and Met-1 cell lines were ideal for our investigation into the effect of tumor heterogeneity on the generation of appropriately matched control and OPN-KO cell lines.

5.4.2 Heterogeneity between subclonal populations derived from McNeuA and Met-1

In order to better understand whether the inherent phenotypic heterogeneity of the McNeuA and Met-1 cells lines would potentially confound the results of an OPN-knockout study, we generated single cell-derived subclonal populations from both the McNeuA (50 clones) and Met-1 (42 clones) parental cell lines (**Figure 5.3A**). The various subclonal populations exhibited morphological heterogeneity, displaying a range of epithelial and mesenchymal phenotypes in culture (**Figure 5.3B,C**). Cell size also appeared to vary between subclones for each given cell line (**Figure 5.3B,C**).

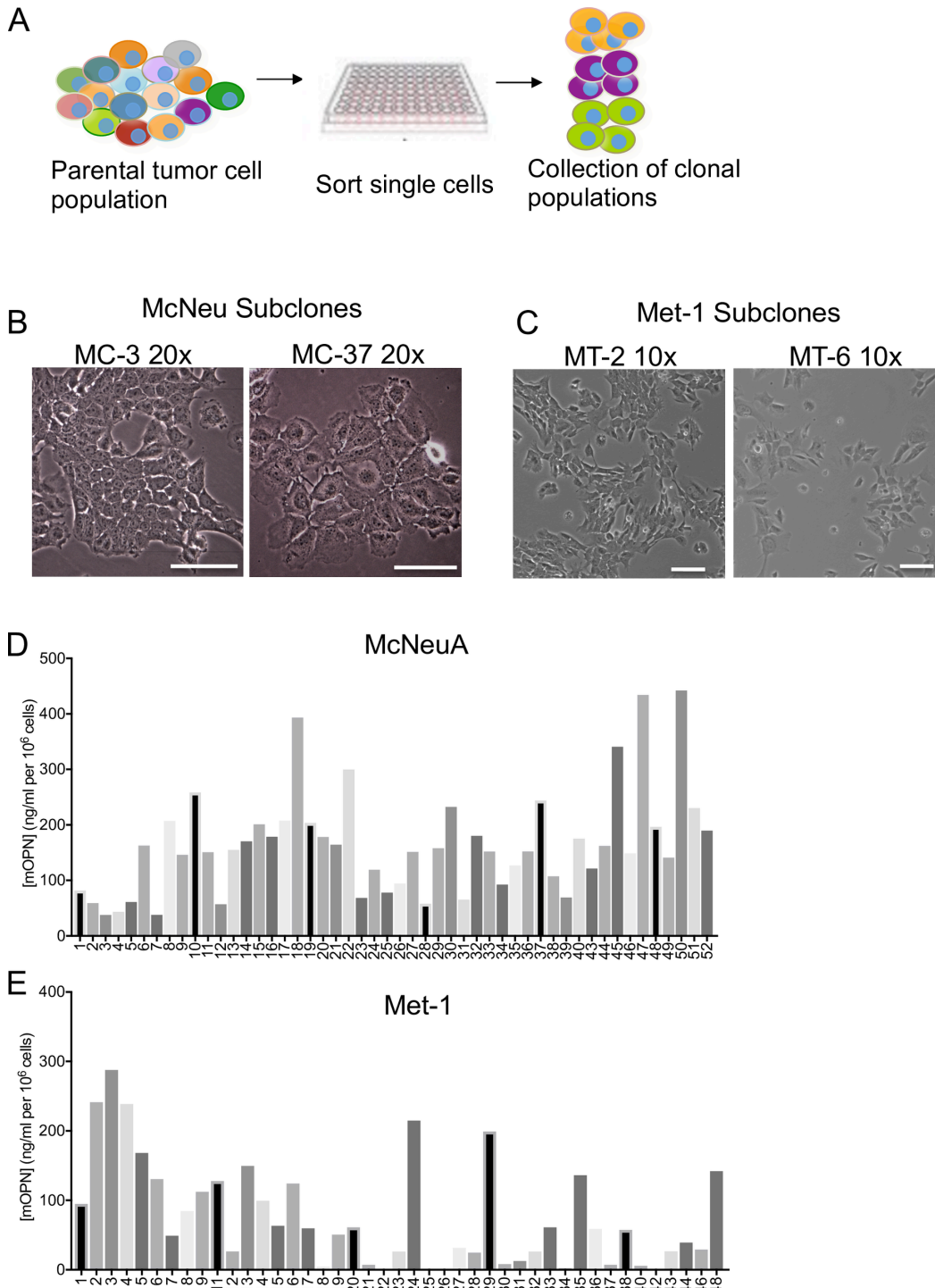


Figure 5.3. Phenotypic heterogeneity of McNeuA and Met-1 subclonal populations. (A) Schematic of subclone derivation from breast cancer cell lines. **(B,C)** Phase contrast images of representative McNeuA (B) and Met-1 (C) subclones to demonstrate morphologic variability. Scale bars = 100 μ m. **(D,E)** Concentration of murine osteopontin (mOPN; ng/ml per 10^6 cells) in 24-hr conditioned media from McNeuA (MC) subclones (D) and Met-1 (MT) subclones (E).

Levels of OPN secreted *in vitro* by the McNeuA and Met-1 subclones varied considerably. The McNeuA subclones secreted a range of OPN from 37.5-442.1 ng/ml per 10^6 cells (**Figure 5.3D**), while the Met1 subclones exhibited a range from no detectable OPN to 287.6 ng/ml per 10^6 cells (**Figure 5.3E**). Importantly, a number of individual subclones secreted levels of OPN that differed significantly from their respective parental population. For example, OPN was 6-8-fold higher in some McNeuA subclones (MC-18, MC-22, MC-45, MC-47, MC-50) and 2.5-3-fold higher in some Met1 subclones (MT-2, MT-3, MT-4) than the parental populations (**Figure 5.1A and 5.3D,E**). Likewise, OPN was undetectable in some of the Met1 cells (MT-18, MT-22, MT-25, MT-26, MT-40, MT-42) (**Figure 5.3E**). We observed similar heterogeneity of OPN secretion from clonal populations that we derived from a human melanoma cell line, MDA-MB-435 (**Figure 5.4A**), suggesting that this phenomenon is not limited to murine cell lines or cancer type.

Taken together, these results highlighted the phenotypic heterogeneity that exists within tumor-derived breast carcinoma populations *in vitro*. We therefore wondered if different clones would perform differently *in vivo* as well.

5.4.3 McNeuA and Met-1 derived clonal populations behave differently *in vivo*

To understand whether various subclones that displayed different phenotypes *in vitro* would also display functional heterogeneity with respect to tumorigenesis, we injected cohorts of FVB mice orthotopically with various

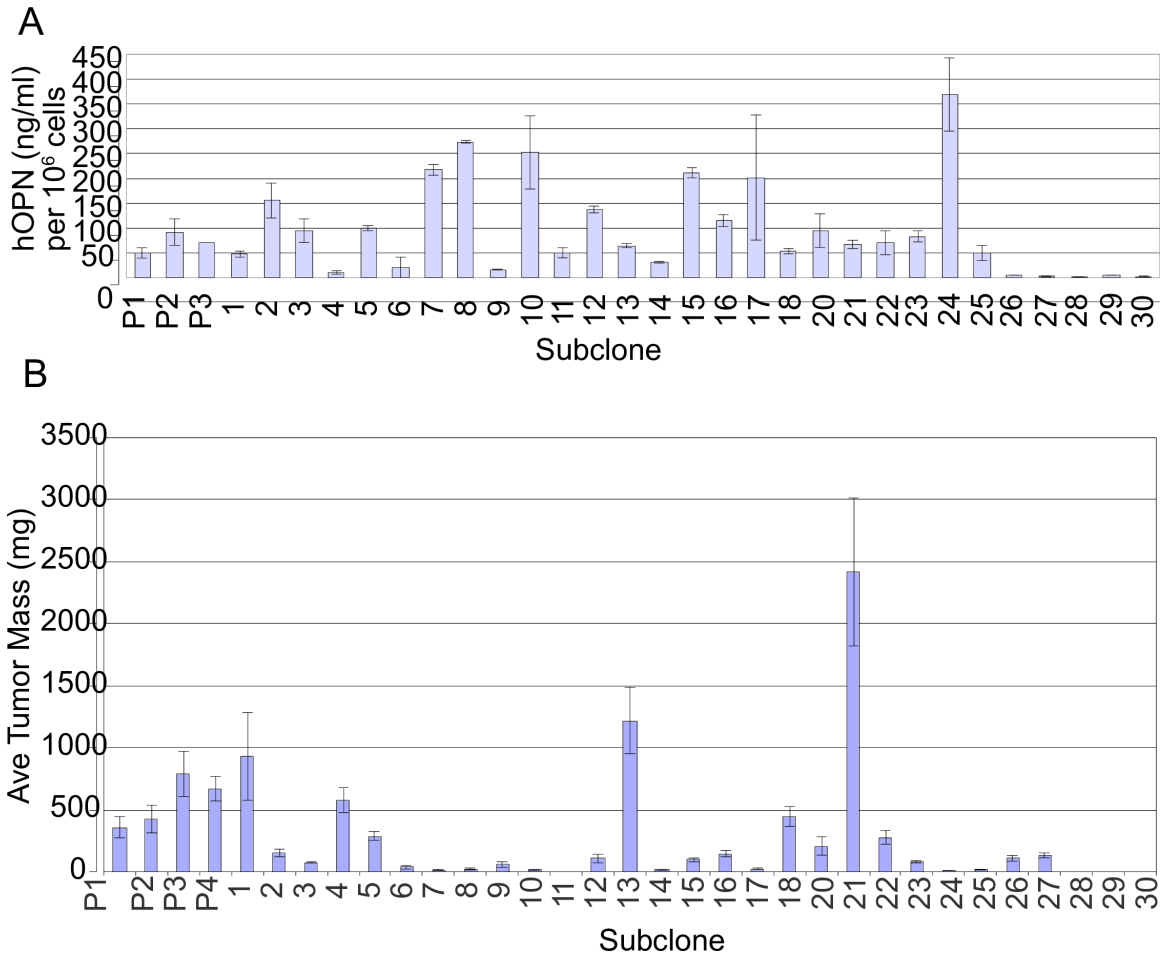


Figure 5.4. MDA-MB-435 subclonal populations are heterogeneous. (A) Human osteopontin (hOPN) secreted into culture medium by MDA-MB-435 parental cells (P1-3) and single cell clones after 24h, normalized for the number of cells in each well (n=3 replicates per cell line). **(B)** Average mass (mg) of tumors 60 days after subcutaneous injection of 2.5×10^5 MDA-MB-435 parental cells (P1-4) or indicated subclones into NOD-SCID (n= 5 mice per cohort).

McNeuA or Met-1 subclonal populations and monitored tumor growth parameters over a course of 64 or 49 days, respectively. We chose to use five subclones from each cell line that secreted the highest levels of OPN (MC-18, MC-22, MC-45, MC-47, MC-50 and MT-2, MT-3, MT-4, MT24, MT-29) (**Figure 5.3D,E**). We injected either 10^5 or 10^6 cells of each McNeuA subclone and 2.5×10^4 or 2.5×10^5 cells of each Met-1 subclone.

Among the McNeuA subclones, a subset of clones (MC-22 and MC-50) formed tumors with 100% incidence, while another (MC-47) failed to form tumors in any mice, and incidence was only slightly higher when more cells were injected (**Figure 5.5A**). Similarly, Met-1 subclones also exhibited variable tumor incidence with 4 of 5 subclones (MT-2, MT-4, MT-24, and MT-29) forming tumors with ~100% incidence while one subclone (MT-3) had reduced incidence to 50-66%, depending on the numbers of cells injected (**Figure 5.5B**).

Those clones that formed tumors displayed variability in latency and growth kinetics. For example, latency and growth kinetics were not statistically different between MC-22 and MC-50 when 10^6 cells were injected (**Figure 5.5D**); however, growth kinetics differed significantly between these clones at 10^5 ($p < 0.0001$, **Figure 5.5C**). The subclonal populations also exhibited differences in latency. For example, when 10^6 cells were injected, MC-22 and MC-50 had latencies of ~20 days, MC-18 and MC-45 had latencies of ~40 days, and MC-47 had a latency of ~60 days (**Figure 5.5D**).

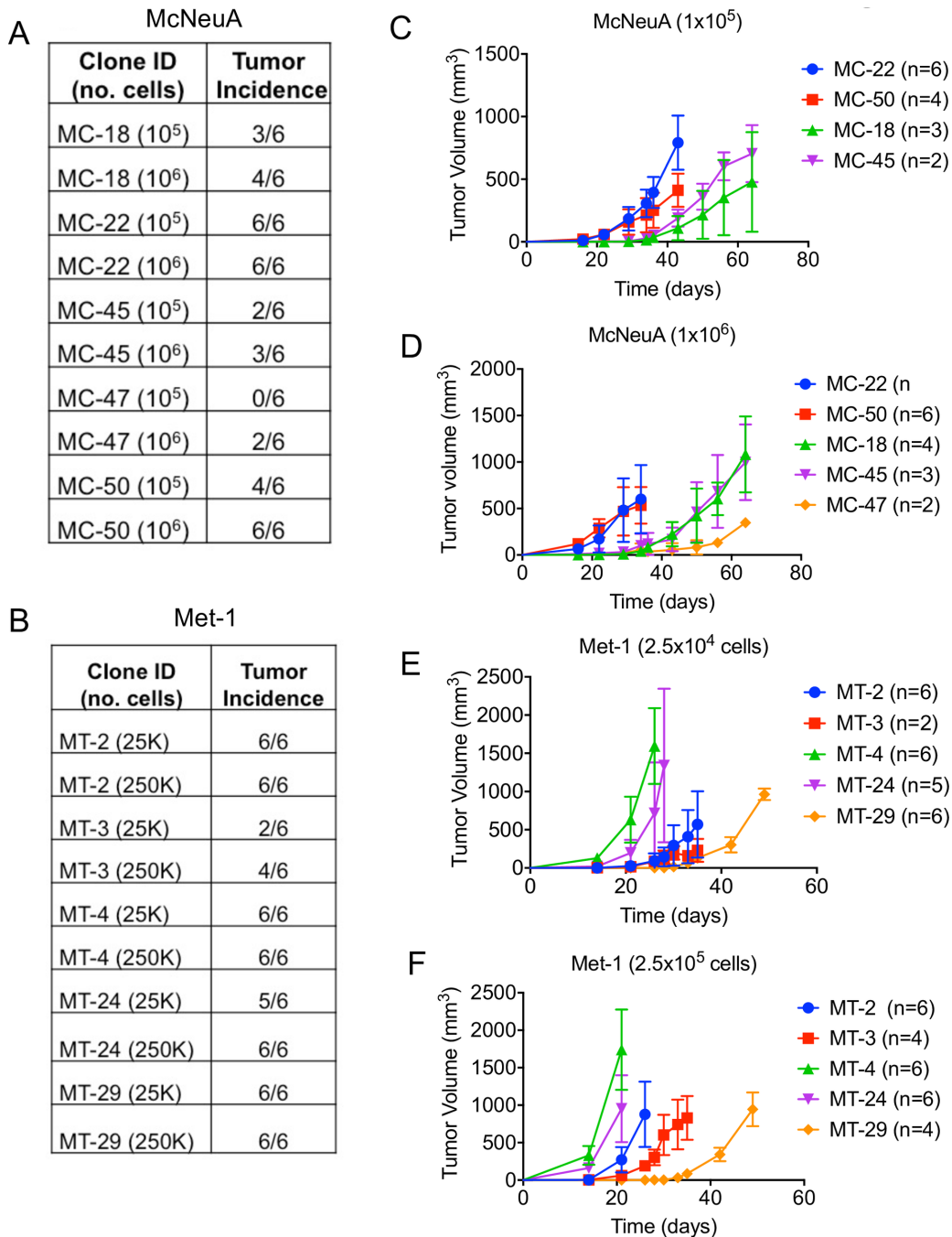


Figure 5.5. McNeuA and Met-1 subclonal populations are functionally heterogeneous in tumor incidence, latency and growth kinetics. (A,B) Primary tumor incidence of indicated McNeuA (10^5 or 10^6 cells; A) and Met-1 (2.5×10^4 or 2.5×10^5 cells; B) clonal populations that were injected orthotopically into FVB mice. **(C,D)** Tumor growth kinetics of indicated McNeuA clones that were orthotopically injected into FVB mice at 10^5 (C) or 10^6 (D) cells. Error bars represent SD; statistical significance evaluated using 2way-ANOVA. **(E,F)** Tumor growth kinetics of indicated Met-1 clones that were orthotopically injected into FVB mice at 2.5×10^4 (E) or 2.5×10^5 (F) cells. Error bars represent SD; statistical significance evaluated using 2way-ANOVA.

Similarly, the growth kinetics of the Met-1 subclonal populations was also variable. When 2.5×10^4 cells were injected, at the 28 day time point (when the MT-4 cohort had reached its endpoint), its growth kinetics were significantly different from the MT-2, MT-4, MT-24 and MT-29 subclones ($p < 0.0002$, **Figure 5.5E**). The Met-1 subclones also had different latencies, with the MT-4 and MT-24 clones having shorter latencies than the other subclonal populations when either 2.5×10^4 or 2.5×10^5 cells were injected (**Figure 5.5E,F**).

The subclones derived from the human melanoma cell line also varied in incidence of subcutaneous tumor formation in NOD-SCID mice, with some clones (i.e. 11, 28, 29, 30) unable to form tumors in vivo (**Figure 5.4B**). Moreover, tumor mass at the experimental end point varied considerably among these subclones (**Figure 5.4B**).

Critically, a number of individual subclonal populations from each tumor model exhibited different tumor formation capabilities than the respective bulk parental population from which they were derived. For example, while the parental Met-1 tumor cell line formed orthotopic tumors with 100% incidence, the MT-3 subclonal cell line formed tumors with only 60% incidence when the same number of cells was injected (**Figure 5.1B and 5.5B**). This was also true of the human xenograft model (**Figure 5.4B**).

These observations revealed the considerable subclonal heterogeneity that exists within human and murine mammary carcinoma cell lines and that the behavior of individual subclones differs from their respective parental populations.

5.4.4 Evidence that identification of proper controls is necessary for correct interpretation of experimental findings

Traditional CRISPR/Cas9 editing protocols begin with infection or transfection of the bulk parental population [95-99]. For this reason, the unedited or mock-infected parental cell line is typically used as a control. Due to the inefficiency of infection and/or editing in certain cell lines (especially tumor cell lines that are hyperploid), there is often a subclonal selection step that follows the initial infection and then a validated, edited subclone is used for subsequent experimentation. Our initial characterizations of the McNeuA and Met-1 parental and subclonal populations demonstrate why one must use caution when considering this commonly used approach.

In some scenarios, subclonal heterogeneity could confound interpretation of knockout efficiency. For example, 23% of the Met-1 subclones have low or no detectable secreted OPN (**Figure 5.3E**). Hence, if one randomly selected one of these clones (e.g. MT-42) and evaluated the functional success of the OPN KO by comparing its OPN secretion levels to that of the parental Met-1 cell line, a failed knockout attempt or false positive result could be overlooked.

In another scenario, if the clonal population that was selected after CRISPR/Cas9 OPN-knockout happened to be clone MT-3 and its orthotopic tumor penetrance was compared to that of the parental Met-1 population, then one could erroneously interpret the necessity of OPN for primary tumor formation, when in fact this clone, prior to OPN knockout, already inherently

forms tumors with lower incidence (~66%) than the parental population (100%) (**Figure 5.1B and 5.5B**).

Likewise, comparing two subclonal populations, even those that secrete similar levels of OPN and form tumors with the same incidence, could also lead to spurious results. For example, if one randomly selected MT-29 as an OPN KO clone and MT-4 as a control, then incorrect conclusions could be drawn about the role of OPN in tumor growth. This is because prior to OPN KO, both clones express similar levels of OPN (~225 ng/ml; **Figure 5.3E**) and form tumors with similar incidence (**Figure 5.5B**) but MT-29 inherently exhibits significantly longer latency and reduced growth kinetics than MT-4 (**Figure 5.5E,F**). The same holds true for MC-18 and MC-50, which secrete similar levels of OPN (~400 ng/ml; **Figure 5.3D**), but incidence of tumor formation after injecting 10^6 cells is ~17% for MC-18 and 100% for MC-50 (**Figure 5.5A**). Hence, the chances of randomly selecting functionally equivalent clones – such as MC-22 and MC-50, which secrete similar levels of OPN (>250 ng/ml; **Figure 5.3D**), form tumors with similar incidence (100%; **Figure 5.5A**), and display similar growth kinetics (**Figure 5.5B**) – are low without extensive characterization of individual clones prior to gene editing.

Our results provided evidence that neither the parental population nor other subclones would represent an appropriately matched wild-type control for a CRISPR/Cas9 knockout cell line that was selected after the gene editing step. The only appropriate control would be to compare the behavior of edited and unedited cells derived from the same clonal population. We therefore concluded

that a modified strategy should be developed to account for heterogeneity and enable the generation of appropriately matched cell lines.

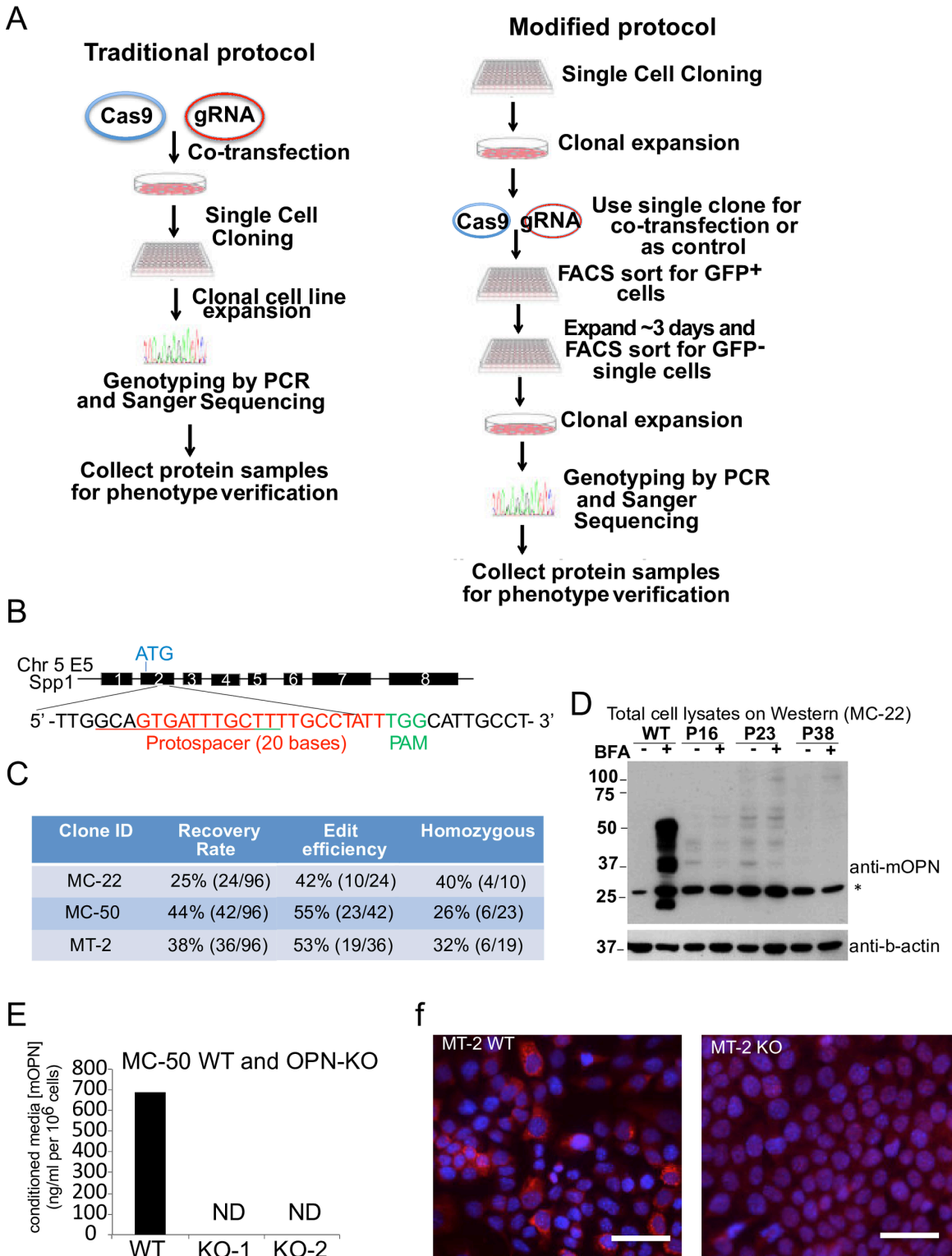
5.4.5 Generating *spp1* knockout clonal populations via CRISPR/Cas9

One would not have known *a priori* about differences in subclonal biological phenotypes and experimental outcomes by taking traditional approaches to gene editing. Therefore, we developed a modified CRISPR-Cas9 editing protocol for generating matched control and knockout cells. Appropriate subclonal populations that we had generated and characterized were chosen for CRISPR/Cas9 gene targeting based on desired biological properties of high intrinsic levels of OPN secretion and orthotopic tumor incidence of 100%. We identified three clonal populations that fit these criteria: MC-22, MC-50, and MT-2 (**Figures 5.3D,E and 5.5A,B**). Hence, in contrast to traditional CRISPR/Cas9 protocols, we used single cell-derived subclonal populations that we had generated prior to CRISPR/Cas9 gene targeting (**Figure 5.6A**).

We used our modified CRISPR/Cas9 editing strategy to delete the *spp1* gene (which encodes Osteopontin) in each subclonal population in order to generate OPN KO cell lines. To do so, the individual subclonal populations were transiently co-transfected with a human codon-optimized spCas9-2A-GFP fusion protein expression plasmid (Addgene plasmid #44719) and a plasmid harboring a sgRNA targeting exon 2 of *spp1* (**Figure 5.6B**). After 24 hours, the GFP-positive (and therefore successfully transfected) Cas9-expressing cells from each subclonal population were collected by FACS and allowed to expand in culture

Figure 5.6. Generation of appropriately matched wild-type and OPN knockout cell lines using CRISPR-Cas9 mediated gene editing. (A) Schematic of traditional and modified CRISPR/Cas9 based gene editing protocols. **(B)** Schematic diagram of sgRNA targeting the *spp1* gene loci. Protospacer sequence is highlighted in red. Protospacer adjacent motif (PAM) sequences are presented in green. **(C)** Recovery rates, gene editing efficiency, and rate of homozygous targeting of the OPN gene in indicated subclones. **(D)** Western blot for OPN protein in MC-22 WT and edited clones (P16, P23, and P38) cultured in the presence or absence of brefeldin A (BFA). Expected multiple Osteopontin isoforms were detected between ~37-50 kD. A non-specific band was detected in each sample, indicated by an asterisk. **(E)** Concentration of murine osteopontin (mOPN) in 24-hr conditioned media from MC-50 WT and edited clones (MC-50-KO1 and MC-50-KO2). mOPN levels were normalized to final cell count. Osteopontin was undetected (ND) in conditioned media collected from both edited subclones. **(F)** Immunofluorescence cytochemical staining for mOPN (red) in MT-2 WT and a validated MT-2 OPN-KO clone. Nuclei are counterstained with hematoxylin (blue). Scale = 100 μ m.

Figure 5.6 (Continued). Generation of appropriately matched wild-type and OPN knockout cell lines using CRISPR-Cas9 mediated gene editing.



for at least six doublings (~3 days) (**Figure 5.6A**). By giving transfected cells more time to recover from FACS sorting, we observed improved single cell cloning recovery rates for the MC-22, MC-50, and MT-2 subclones (respectively 42%, 55%, and 53%, **Figure 5.6C**) compared to transfected cells that were directly sorted as single cells, in which the recovery rate was ~5% in an initial trial (data not shown). The higher colony recovery rate and enrichment of Cas9 expressing cells during the first sorting step allowed us to achieve both higher editing efficiency and more homozygously edited clones (**Figure 5.6C** and **Figure 5.7**).

Due to the transient nature of our transfection protocol, only cells in which the Cas9-GFP fusion protein had been randomly integrated would maintain GFP expression past this point. In order to avoid random integration of the Cas9 expression plasmid into the genome, a second round of single-cell sorting by FACS was employed to isolate cells that had not undergone a Cas9 integration event by sorting and selecting for GFP-negative cells (**Figure 5.6A**). Single cell-derived subclones were then expanded in culture.

We next employed Sanger sequencing to identify the edited subpopulations from among the recovered subclones (**Figure 5.7A**). Of the recovered subclones from the MC-22, MC-50, and MT-2 lines, a subset of the single cell clones contained either a hemizygous or homozygous mutation in the *spp1* gene, representing editing efficiencies of 42%, 55%, and 53%, respectively (**Figure 5.6C**). We found that MC-50 clone is hyperploid for the chromosome region containing *spp1* based on partially edited clones' sequencing result

(**Figure 5.7B**) and this observation was further validated by genotyping these clones using TA cloning and Sanger sequencing (data not shown). Between 26-40% of the successfully edited clones contained homozygous mutations (**Figure 5.6C**).

We validated loss of OPN protein expression in each of the OPN KO clones compared to its appropriately matched control using western blotting, ELISA of conditioned media, or immunocytochemistry. We observed no detectable OPN protein (**Figure 5.6D-F**), demonstrating that our CRISPR/Cas9 editing strategy was successful and we had generated authentic OPN KO subclonal cell lines.

5.4.6 Osteopontin is dispensable for primary tumor growth

Most studies, including our own, report that OPN is dispensable for primary tumor growth, but is critical for metastasis due to its effects on tumor cells, the host systemic environment, and the tumor microenvironment [47, 110, 113]. Therefore, successful generation of appropriately matched KO and WT cell lines should also reflect these properties (e.g., loss of OPN should have no effect on primary tumor growth, but should alter metastatic ability). This makes OPN an ideal protein to test our concept because its dispensability for primary tumor growth means that WT and OPN KO clones should exhibit similar primary tumor growth kinetics and incidence. Therefore, we tested the tumor formation capabilities of the matched clones.

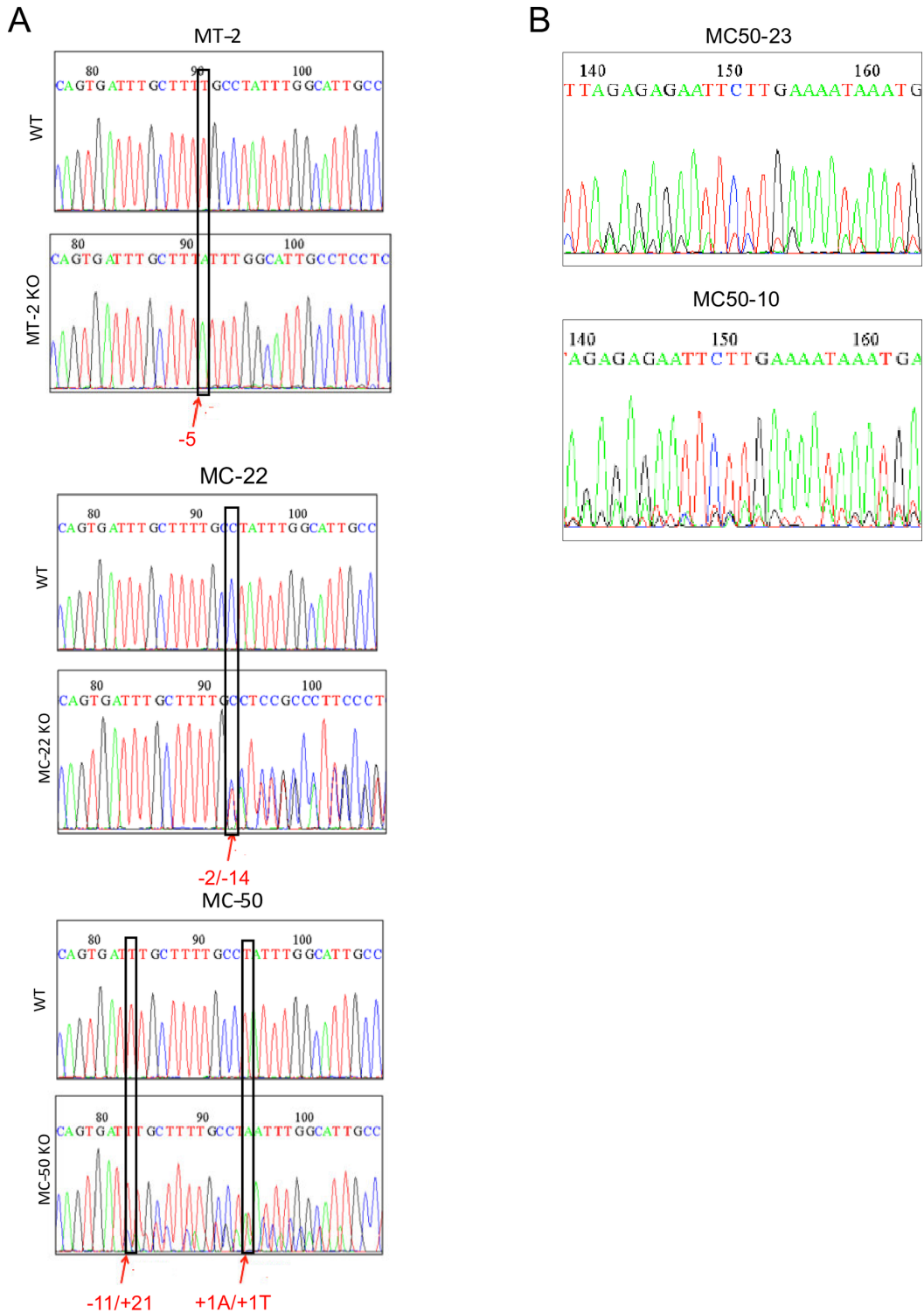


Figure 5.7. Sanger sequencing of matched wild type and CRISPR-Cas9 OPN knockout cell lines. (A) Examples of coding-frame shift confirmed to be homozygous in MT-2, MC-22 and MC-50 clones by Sanger sequencing as reported in Figure 4C. **(B)** Example of coding-frame shift confirmed to be heterozygous as reported in Figure 5.6C.

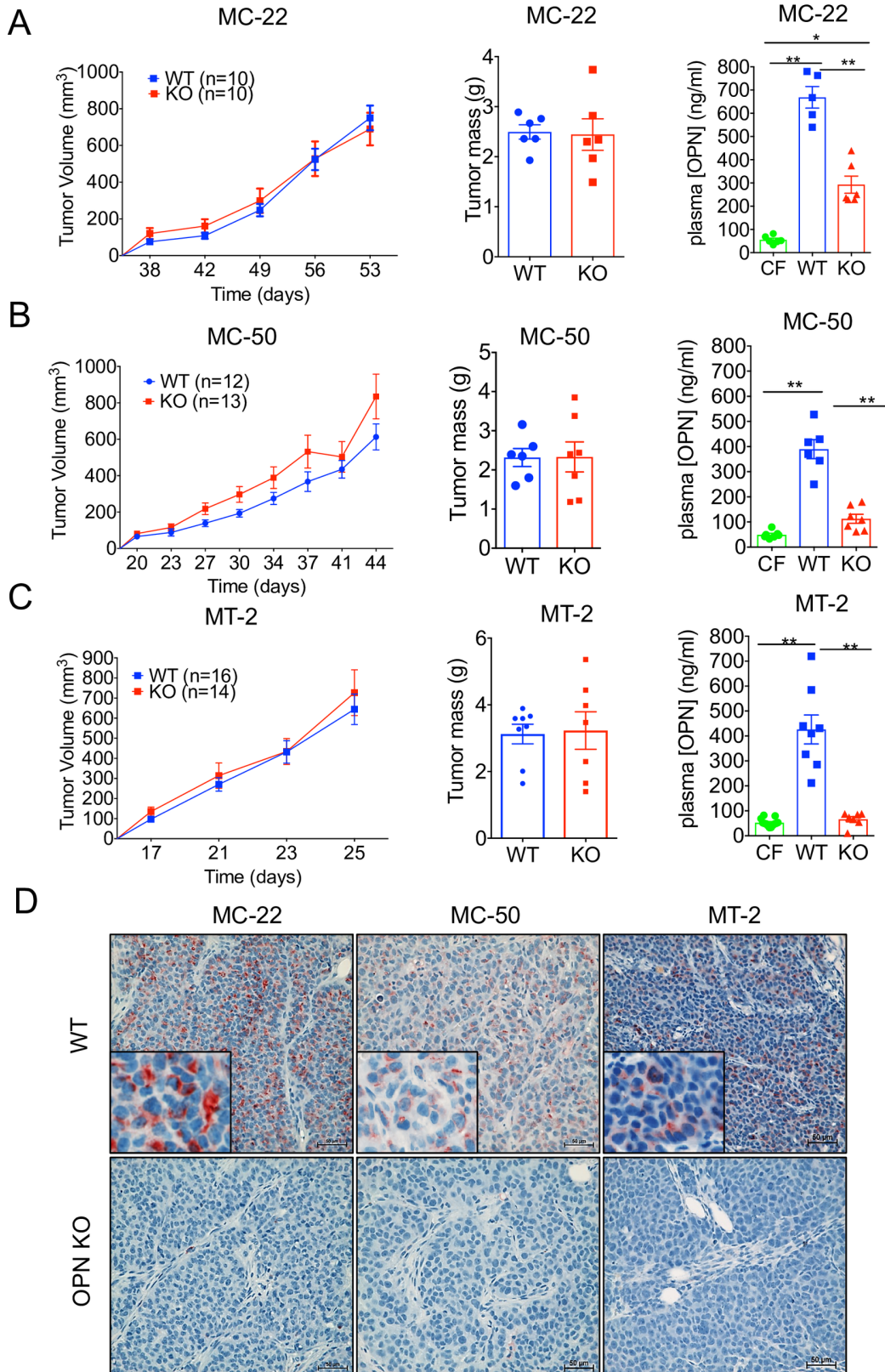
WT and OPN KO MC-50 cells (2×10^5), MC-22 cells (1×10^5) or MT-2 cells (2.5×10^4) were orthotopically injected into FVB mice and were allowed to grow until tumors reached $\sim 1 \text{ cm}^3$. Loss of tumor-derived OPN did not significantly affect growth kinetics or the final mass of any of the tumors derived from matched subclonal cell lines (**Figure 5.8A-C**). In fact, there were no significant differences in any other tumor growth parameters (**Figure 5.8A-C**) or spleen mass (**Figure 5.9**) between cohorts bearing WT and the respective matched OPN KO tumors.

As a control, we tested the concentration of circulating plasma mOPN in the tumor-bearing mice and cancer-free controls. As expected, mOPN plasma levels were elevated in the mice bearing WT tumors relative to the cancer-free cohort, and plasma OPN levels were significantly reduced in the mice bearing KO tumors relative to WT (**Figure 5.8A-C**). Plasma OPN levels from the cohorts of mice bearing MC-50 and MT-2 OPN KO tumors were not significantly different from their respective cancer-free cohorts (**Figure 5.8A-C**). However, plasma OPN from mice bearing MC-22 KO tumors was significantly higher than the cancer free controls (**Figure 5.8A**), suggesting that clone MC-22 may in fact induce an elevation in host-derived OPN.

It is important to note that if we had used the parental McNeuA cell line as a WT control rather than the appropriately matched WT MC-22 cell line, we would have failed to see a significant difference in the circulating OPN levels between cohorts (**Figure 5.9B**). This observation would not have been possible

Figure 5.8. OPN depletion does not affect primary tumor formation in murine models of HER2⁺ and ER⁻ breast cancer. (A-C) FVB mice were orthotopically injected with 10⁵ MC-22 (A), 10⁵ MC-50 (B), or 2.5 x 10⁴ MT-2 (C) cells. Growth kinetics (mm³) of orthotopic tumors of WT (blue lines) and validated OPN-KO clones (red lines). Mass of primary tumors from WT (blue) or OPN-KO (red) cohorts at experimental end points. No statistically significant differences determined by 2way ANOVA (tumor growth kinetics) or unpaired, two-tailed Students' t-test (tumor mass) statistical analyses. Circulating plasma murine osteopontin (mOPN) levels from cancer-free (green) or tumor bearing mice from the MC-22, MC-50, or MT-2 WT (blue) or OPN-KO (red) cohorts (One-way ANOVA: *** p = 0.0003, **** p < 0.0001). Error bars represent SD. **(D)** Representative immunohistochemical staining for mOPN (red) in tumors derived from MC-22, MC-50 and MT-2 WT and validated OPN-KO cell lines. Cell nuclei counterstained with hematoxylin (blue). Scale bar = 50 μm.

Figure 5.8 (Continued). OPN depletion does not affect primary tumor formation in murine models of HER2⁺ and ER⁻ breast cancer.



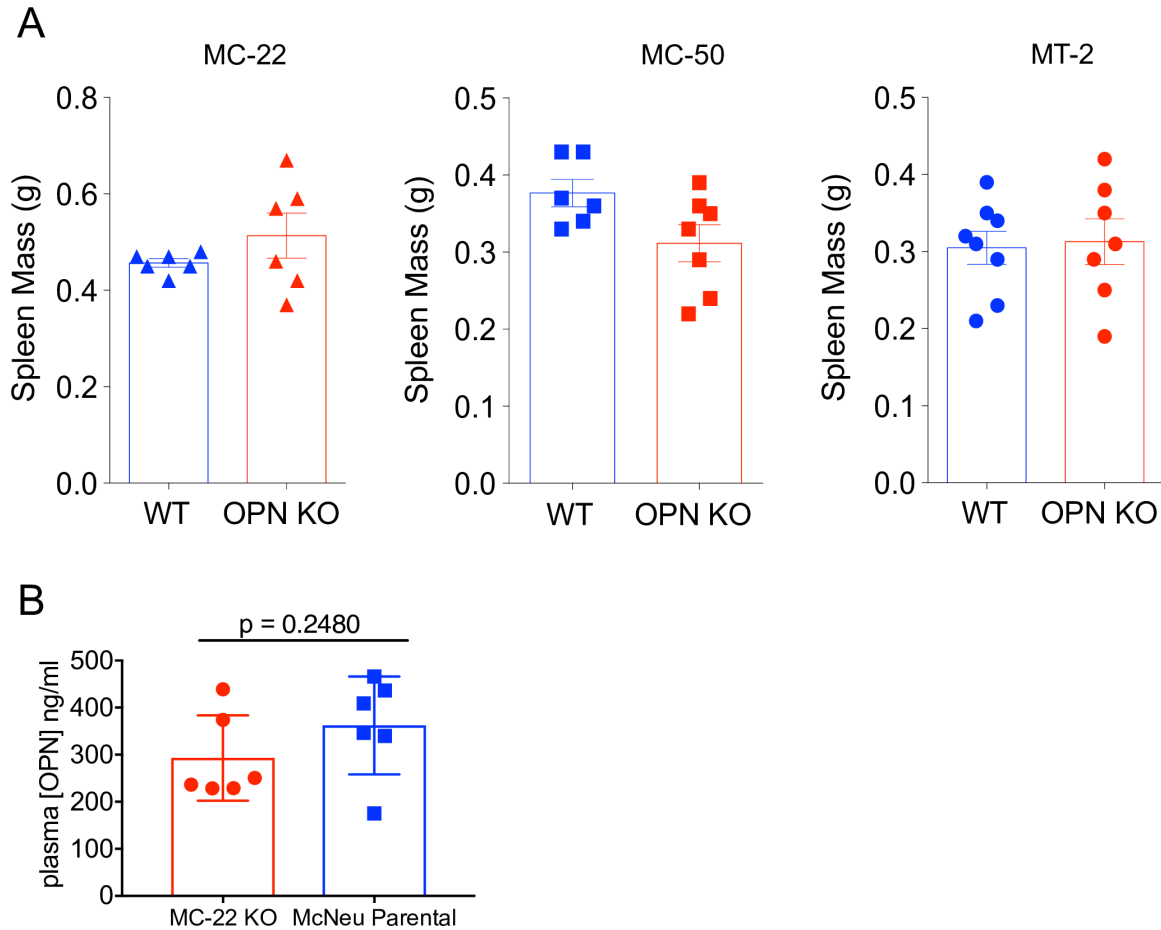


Figure 5.9. OPN depletion does not affect final primary tumor mass or spleen mass in murine models of HER2⁺ and ER⁻ breast cancer. (A) Final spleen mass was measured in mice injected with either MC-22, MC-50, or MT-2 WT or OPN-KO cell lines. No significant difference was observed between WT and KO cohorts for each clone (unpaired, two-tailed Student's t-test). **(B)** Circulating plasma mOPN levels were measured from mice bearing either McNeuA Parental or MC-22 OPN-KO primary tumors using ELISA (unpaired, two-tailed t-test, p=0.2480). Error bars represent SD.

using a traditional CRISPR/Cas9 gene editing protocol, highlighting once again the strength of our system and the necessity of using appropriately matched control cell lines in knockout studies.

Finally, we visualized OPN expression in the tumors that formed in each cohort using immunohistochemical staining. We observed positive staining for OPN in the WT MC-22, MC-50, and MT-2 tumors, but did not detect any OPN⁺ cells in the corresponding OPN KO tumors (**Figure 5.8D**), confirming that the OPN KO was successful. These observations provided further evidence that any circulating OPN detected in mice injected with the OPN-KO clones (**Figure 5.8A-C**) was host-derived rather than tumor derived.

Together, these results demonstrated that our modified CRISPR/Cas9 gene editing protocol can be successfully used for studies examining the role of a gene in primary tumor outgrowth.

5.4.7 Loss of osteopontin reduces multifocal metastatic outgrowth

Osteopontin is considered a biomarker for tumor progression and is detected at higher levels in more aggressive tumors than their low-grade counterparts, is elevated in the serum of patients with metastatic disease, and is included in gene lists predicting poor prognosis for many cancer types [80-87]. Although OPN is most often dispensable for primary tumor growth, OPN is necessary for metastasis [47, 119-121].

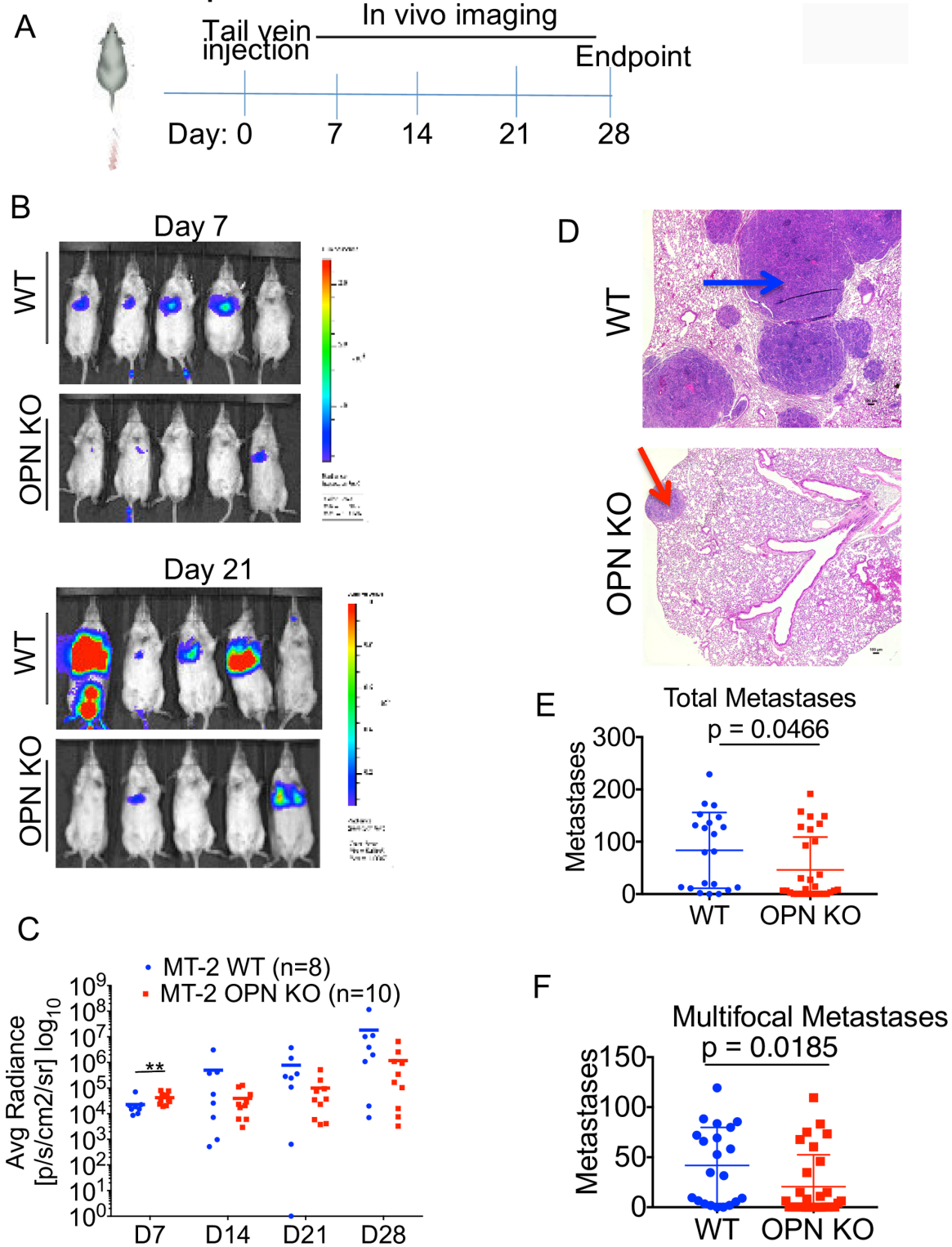
Met-1 cells are highly metastatic [107] and therefore serve as an ideal pre-clinical model of ER-negative disease to test whether our CRISPR/Cas9 system is useful for metastasis studies. To address this question, we labeled the MT-2 WT and MT-2 OPN KO cell lines with a dual GFP/luciferase reporter and injected the labeled cells intravenously via the tail vein into cohorts of mice (**Figure 5.10A**). Metastasis formation was monitored using bioluminescent *in vivo* imaging at weekly intervals.

Metastatic burden was decreased in the MT-2 OPN KO cohort relative to that of the MT-2 WT cohort, as indicated by reduced bioluminescent signal over the course of the experiment ($p=0.0085$ at day 7, $p>0.05$ for all other time points; **Figure 5.10B,C**). As further confirmation, we analyzed H&E lung sections at the experimental end point and quantified the numbers of single and multifocal metastases. There were significantly fewer total and multifocal lung metastases in mice that had been injected with the OPN KO cells compared to mice that had been injected with OPN WT cells (**Figure 5.10D-F**). Additionally, the average number of single-focus metastatic outgrowths was also reduced in mice in the OPN KO cohort compared to the WT cohort (**Figure 5.11**).

Collectively, our results established that by using appropriately matched cells, we could confidently conclude that OPN is necessary for metastatic colonization and that our CRISPR/Cas9 protocol is useful for pre-clinical metastasis studies.

Figure 5.10. Matched wild type and knockout OPN cell lines can be used for pre-clinical metastasis studies. (A) Experimental schema for metastasis assay. **(B)** Representative *in vivo* bioluminescent images of mice injected with MT-2 WT or MT-2 OPN KO after 7d and 21d. **(C)** Average bioluminescent signal (radiance, log₁₀) from mice with MT-2 WT (blue) or MT-2 OPN KO (red) at indicated time points. (Mann-Whitney: ** p = 0.0085). **(D)** Representative hematoxylin & eosin staining of lungs from mice that received tail vein injections of MT-2 WT or MT-2 OPN KO cells. An example of a multifocal metastasis is marked with a blue arrow and an example of a single focus metastasis is marked with a red arrow. Scale = 100 μm. **(E)** Quantification of total metastases in MT-2 WT (blue) and MT-2 OPN KO (red) cohorts (WT n = 21, KO n = 30; Mann-Whitney, p = 0.0466). Error bars represent SD. **(F)** Quantification of multifocal metastases in MT-2 WT (blue) and MT-2 OPN KO (red) cohorts (WT n = 21, KO n = 30; Mann-Whitney, p = 0.0185). Error bars represent SD.

Figure 5.10 (Continued). Matched wild type and knockout OPN cell lines can be used for pre-clinical metastasis studies.



5.4.8 Loss of osteopontin enhances chemosensitivity

Resistance to standard chemotherapies remains a significant clinical problem, particularly for triple-negative breast cancer [122]. In order to interrogate whether OPN contributes to chemoresistance in breast cancer models, we tested the MT-2 WT and KO cell lines for sensitivity to AC-T chemotherapy in vivo.

We injected 2.5×10^4 MT-2 WT or matched OPN KO tumor cells into the mammary fat pads of FVB mice. When established tumors reached $\sim 60\text{--}80 \text{ mm}^3$ in volume (14 days), animals were randomized based on tumor volume and enrolled into either vehicle control (PBS) or AC-T chemotherapy treatment cohorts (**Figure 5.12A**).

MT-2 WT and MT-2 KO tumors exhibited sensitivity to AC-T treatment relative to their respective vehicle-treated cohorts (**Figure 5.12B**). However, in response to AC-T, the MT-2 KO tumors exhibited reduced growth kinetics compared to their MT-2 WT counterparts in three independent trials (**Figure 5.12B**). Likewise, final tumor mass was significantly lower in the MT-2 KO treatment cohorts compared to the MT-2 WT treatment cohorts (**Figure 5.12C**). Sensitivity to chemotherapy was only apparent in vivo, as there were no differences between MT-2 WT and MT-2 KO cells in response to doxorubicin or paclitaxel in vitro (**Figure 5.13A,B**).

Together, these data established that elimination of OPN expression enhances chemosensitivity of the MT-2 breast cancer population.

Figure 5.12. MT-2 OPN-KO derived tumors exhibit enhanced chemosensitivity *in vivo*. **(A)** Experimental schema. 2.5×10^4 MT-2 WT or OPN-KO tumor cells were injected into the mammary fat pads of 6–8-week-old female FVB mice. A single dose of AC-T was initiated at 14 days, when tumors reached $\sim 60\text{--}80 \text{ mm}^3$ in volume, and tumor growth was monitored periodically until the end point of 44 days. Error bars represent SD. **(B)** Tumor growth kinetics for MT-2 WT vehicle (blue; n=5) and AC-T treated (green; n=4) and MT-2 OPN-KO vehicle (red; n=3) and AC-T treated mice (purple; n=2). Representative of 3 biological repetitions. Error bars represent SD. **(C)** Endpoint tumor mass for MT-2 WT and MT-2 OPN-KO AC-T treated mice from 2 separate experiments (Mann-Whitney, $p = 0.0037$; endpoint tumor mass was not measured during the first of the three experimental repetitions). Data points from individual repetitions are represented with different colors. Error bars represent SD.

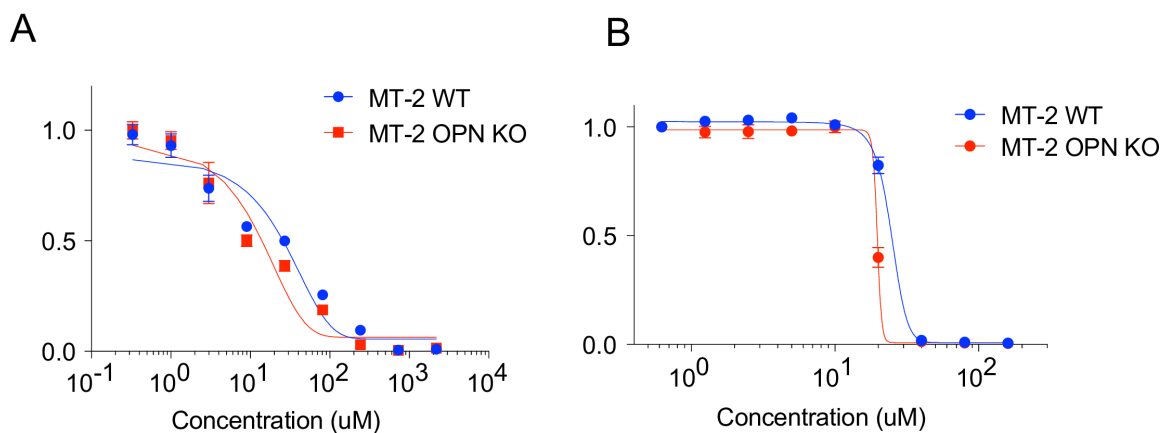


Figure 5.13. Enhanced Chemosensitivity of OPN-depleted cell lines is not observed *in vitro*. (A,B) MT-2 WT or MT-2 OPN-KO cells were plated in quadruplicate and were treated with various doses of doxorubicin (A) or paclitaxel (B) 24 hours after plating. ATP levels were quantified 72 hours after treatment as a surrogate measure for viability using Cell-Titer Glo and were normalized to vehicle treated. Error bars represent SD.

5.5 Discussion

The ability to genetically edit a cell line to either suppress, knockdown, induce, overexpress, knock-in, or mutate a protein of interest provides an indispensable tool for biological research. However, our work demonstrates that studies designed to test necessity or sufficiency of genes/gene products without choosing appropriately matched unedited controls run the risk of detecting false positive or false negative results due to inherent phenotypic differences in subclonal cellular populations that result from heterogeneity. Our alternative approach to generate subclones and screen for desired phenotypes prior to genetic manipulation provides one solution to this problem.

As we demonstrated through proof-of-concept studies, our approach works well for hypothesis-testing experimentation, when biological phenotypes to be tested are defined. Another benefit to our modified approach is that characterization of subclone phenotypes may enable one to select a range of biological properties that could be tested. Moreover, this approach enables discovery of novel properties for which mechanistic insight could be obtained in a straightforward manner. For example, one of our subclones (MC-22 KO) stimulated elevated host plasma OPN while another clone (MC-50 KO) did not, thereby enabling one to compare properties (e.g., gene expression) of related clones to yield mechanistic insights. While our approach takes added time and expense, it ensures that the real function of a specific protein of interest is uncovered during experimentation.

One caveat of our approach is that isolating particular subclonal populations removes the inherent heterogeneity of a cell line, which could have important biological consequences. This is particularly relevant in circumstances in which the biology is not

well understood. If heterogeneity is desirable, then one could employ a clonal pooling approach, thus ensuring that a given experiment is both properly controlled and that the heterogeneous nature of the parental cell line is not lost.

It has been reported that functional heterogeneity can arise even within a 'clonal' cellular population as a result of cell plasticity or epigenetic alteration [27]. Hence, although we did not test clonal plasticity in our system, it is reasonable to hypothesize that a high degree of cellular plasticity could cause differences between matched control and edited populations that may not be due to the target gene. Limiting the *in vitro* passage of the cell lines to minimize chances for additional selection and monitoring for unexpected functional changes in control cell lines may help to prevent this added complication.

Our new experimental approach led us to discover an important function of OPN in resistance to a standard breast cancer chemotherapy regimen. Use of our matched wild type and OPN-deficient subclones will enable future studies to determine the mechanism through which OPN acts to promote this chemoresistance in breast cancer. It appears that it may rely on a non-cell intrinsic mechanism, as the reduced chemosensitivity was only observed *in vivo* and not *in vitro*. The matched subclones we report here provide a valuable tool to expand such studies.

Chapter 6

Discussion

6.1 Summary of Findings

The main goals of my thesis work were to: (1) develop a molecular barcoding system that could allow for the tracking of intratumoral clonal dynamics using detection technology that was available in-house and could reliably detect barcode signal from *in vivo* samples; (2) examine whether the systemic environment is capable of shaping intratumoral heterogeneity; and (3) demonstrate why functional heterogeneity must be taken into consideration during experimental design.

In **Chapter 2**, I describe the development of a next-generation sequencing based detection method for the PRISM molecular barcodes that were developed by our collaborators [76]. The PRISM barcodes were not designed with sequencing-based detection in mind, and both the barcodes themselves and the common flanking sequences result in the need to sequence extremely low-diversity amplicons, which represented a technical hurdle that needed to be overcome. Additionally, in order for sequencing-based barcode detection to be cost effective, it was necessary to implement a sample multiplexing strategy that allowed for the sequencing of multiple samples in a single lane. The protocol that I developed addresses both of these issues and provides an adaptable system for clonal tracking using molecular barcodes and a sequencing-based detection system that could be applied by future investigators in a wide variety of experimental settings.

In **Chapter 3**, I generated a collection of barcoded, single-cell derived clonal populations that were used to demonstrate that modulations of the host systemic environment can affect the intratumoral heterogeneity of distantly located tumor cell outgrowths in an innate immune dependent fashion (**Figure 6.1**). Our unique molecular

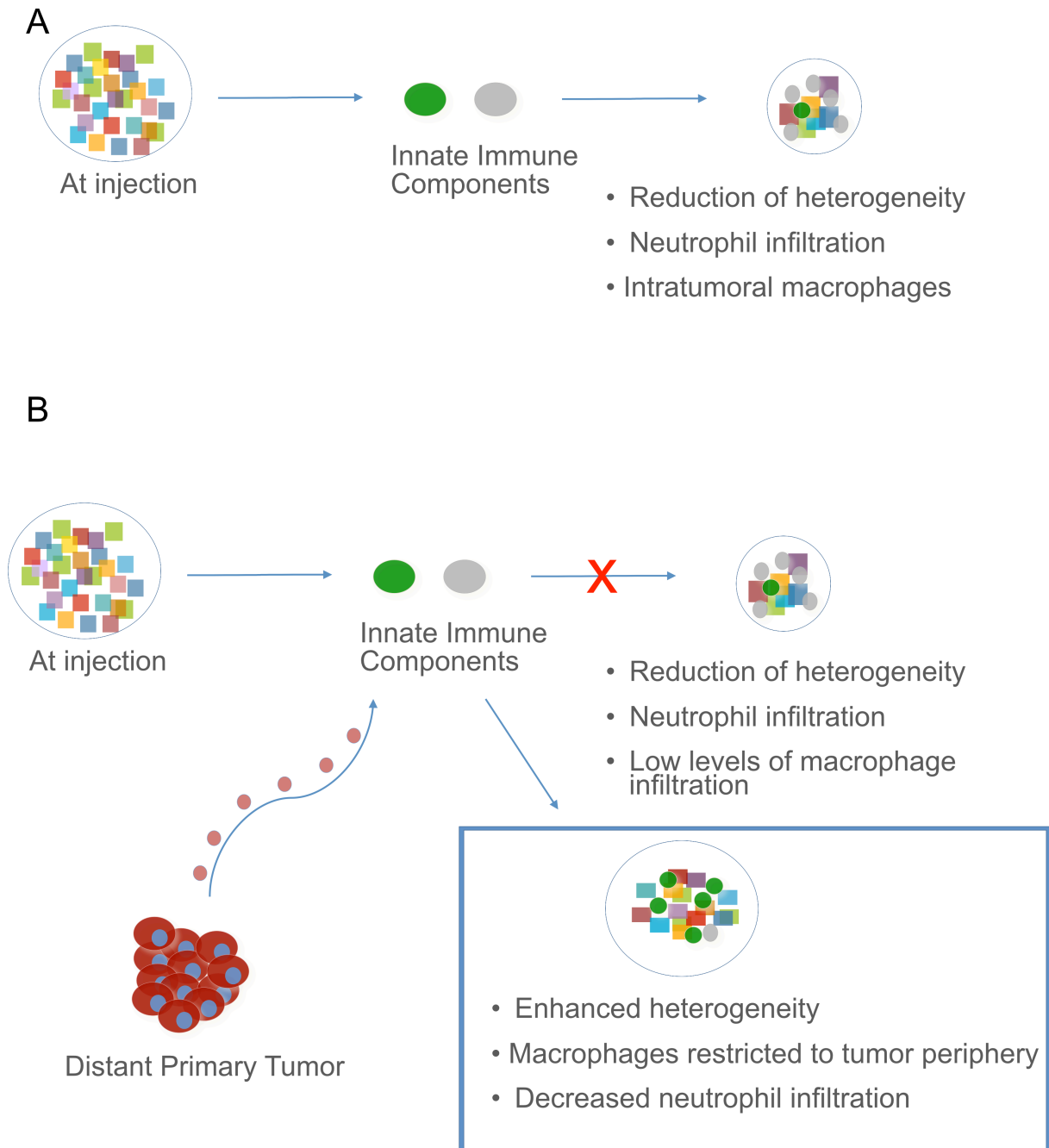


Figure 6.1. The systemic environment can modulate intratumoral heterogeneity.

(A) In the naïve host systemic environment, innate immune components infiltrate tumors that have undergone a reduction in clonal heterogeneity compared to the injected cell population. **(B)** In the presence of a distant tumor that secretes signals that generate an activated host systemic environment, a reduction in neutrophil infiltration is observed, macrophages are restricted to the tumor periphery, and an enhancement of heterogeneity is observed compared to the naïve host systemic environment.

barcoding system allows for the characterization of subpopulations that are identified as being biologically relevant, which allowed me to identify malignant phenotypes that were acquired among cooperating clonal populations present in tumors in the systemic activation setting, specifically chemotherapeutic resistance. To the best of our knowledge, this work represents the first time that a cause of functional heterogeneity has been identified. Our findings involving the functional consequences of enhanced heterogeneity highlight the need for an increased understanding of the mechanisms driving clonal evolution so that methods can be developed to prevent or disrupt heterogeneity, potentially reducing instances of therapeutic resistance and improving patient outcome.

In **Chapter 4**, I generated a set of barcoded clonal populations from a murine breast cancer cell line that allowed us to expand our studies of intratumoral heterogeneity into an immunocompetent setting. Preliminary studies suggested that both the adaptive and innate immune systems can shape intratumoral heterogeneity, and this model system will serve as a powerful tool to build on our observations from the immunocompromised human xenograft model employed in **Chapter 3**.

In the last part of this thesis, I describe a modified gene-editing protocol that provides appropriate controls for functional heterogeneity within the parental cell line. I employ this protocol in both proof-of-concept and discovery studies to demonstrate its usefulness. This work demonstrates the significant impact that functional heterogeneity can have upon the interpretation of experimental results and the protocol that we developed will serve as an important resource for the scientific community.

6.2 Discussion: Future directions and clinical implications

Tumor cell heterogeneity is a major driver of cancer progression and therapeutic resistance [123]. Correspondingly, increased heterogeneity is associated with worse prognosis in several cancer types, including breast cancer [124]. As sequencing technology has evolved and become increasingly sensitive, the patterns of subclonal heterogeneity in both primary tumors and metastases have revealed critical insights into how and why metastases and therapeutic resistance develops, providing hypothesis generating information for the creation of novel, more effective treatment strategies. However, many basic questions about the biology driving the generation and evolution of heterogeneity, particularly non-genetic heterogeneity, remain unanswered, making it difficult to incorporate information about patient tumor heterogeneity into rationally-designed treatment decisions. For example, despite the fact that genetic heterogeneity is much easier to detect and evaluate than non-genetic heterogeneity, it is still unknown whether genetic heterogeneity is more likely to be acquired through the slow, step-wise addition of individual mutations or through large, ‘marcoevolutionary’ events, such as the major genomic rearrangements associated with chromothripsis [30]. The majority of our knowledge regarding the generation of genetic heterogeneity has been obtained by looking backwards over time and using phylogenetic relationships between subclonal populations to infer the evolutionary progression of a tumor, and these types of gaps of knowledge make it extremely difficult to do so. Additionally, without a thorough understanding of how heterogeneity develops, it is difficult to predict the future evolutionary trajectory of tumors, making it difficult to identify particularly threatening subpopulations that it could be beneficial to pre-emptively target with combination

therapies. The development of novel experimental models, such as our molecular barcoding system, and rapidly advancing sequencing and gene expression technologies promise to greatly advance our understanding of the basic biology driving heterogeneity in the coming years.

Within a clinical setting, heterogeneity is particularly difficult to evaluate in solid tumor types, such as breast tumors. Characterization of primary tumors is frequently performed using one or a few small biopsy samples, and due to both regional heterogeneity and the low sensitivity of currently employed technology to detect genetic aberrations, subclonal (or even clonal) driver mutations can frequently go undetected [124]. A number of strategies have been suggested for overcoming this, but it has been difficult to rigorously evaluate which would be most effective. Some of these options include sampling a large number of tumor regions, employing more sensitive sequencing technologies, analyzing circulating tumor DNA (ctDNA), and analyzing circulating tumors cells (CTCs) [124, 125]. The analysis of ctDNA and/or circulating tumor cells are particularly attractive options because they do not require invasive procedures to obtain the relevant samples and they could provide information about difficult (or impossible) to sample regions, such as metastatic outgrowths. Both methods have benefits and drawbacks, as the isolation of CTCs is technically challenging, but ctDNA may provide overrepresentation of dying tumor cells [124]. Studies to evaluate the relative accuracy and utility of each of these methodologies could be complicated in rapidly evolving tumor cell populations that acquire new mutations during the course of a study, and undersampling of subclonal populations could also represent a technical barrier. However, our molecular barcoding system could be to address these questions

in a pre-clinical setting, providing valuable information about the best strategies to pursue in the more costly and high-risk clinical setting.

Non-genetic sources of heterogeneity are much more difficult to evaluate than genetic heterogeneity in both the clinical and pre-clinical setting. Several techniques have been proposed, mostly involving panels of immunohistochemical stains, analyses of morphological heterogeneity, or single-cell RNA sequencing [126, 127]. However, these methods are far from comprehensive and could be cost-prohibitive. Without a better understanding of how non-genetic heterogeneity evolves over time, it will be very difficult to try to limit it therapeutically. However, an alternative approach could be to identify processes that generate and support non-genetic heterogeneity and target those processes.

In this thesis, I demonstrated that the systemic environment can enhance the intratumoral heterogeneity of distantly located tumor outgrowths. Previous pre-clinical studies have demonstrated that some tumor supportive systemic processes can be reversed therapeutically, resulting in improved disease outcomes. For example, in both a model of primary-tumor driven systemic activation and in a study of surgery-induced systemic inflammation, NSAID use was effective in disrupting some of the systemic processes that promoted metastasis [46, 48]. This data agrees with clinical observations that aspirin use after breast cancer diagnosis correlates with decreased rates of metastasis and improved survival [128, 129]. This finding is particularly exciting because it both represents a potential method to intervene prior to the development of overt metastases, at which point curative treatment is not usually possible, and in contrast to many cancer therapeutics NSAIDs have few side effects and low morbidity.

The focus of these studies was tumor-induced systemic activation. Previous work has demonstrated that only a subset of tumors are capable of affecting changes to the systemic environment that promote the outgrowth of distant tumor cells [43, 47]. This suggests that there could be unique biomarkers, either characteristics of the primary tumors themselves or downstream indicators of systemic activation, which could be used to stratify patient risk. Several of the characteristic features of the pre-clinical models of tumor-induced systemic activation, such as high levels of circulating Osteopontin and granulin expression, have been previously associated with poor prognosis among patients with breast cancer [45, 47]. Further mechanistic study of the tumor-derived factors that are capable of modulating the systemic environment and promoting disease progression could identify additional biomarkers, making it possible to create a signature of systemic activation and to identify patients that are at increased risk for the development of metastases and/or therapeutic resistance in the future. These patients could be closely monitored to allow for therapeutic intervention prior to reaching an incurable disease state and their disease could receive more extensive characterization to allow for pre-emptive targeting of resistant tumor cell subpopulations that could cause therapeutic resistance.

Our model of tumor-induced systemic activation utilizes a bilateral injection scheme to evaluate the ways that one tumor can affect distant tumor cells with which they have no physical contact. This can model a number of situations, including a primary tumor's interactions with distantly located DTCs or bilateral breast tumors. Interestingly, a recent retrospective study found that patients with bilateral breast tumors had significantly lower rates of pathological complete response to neoadjuvant

treatment with anthracycline-taxane base chemotherapies than patients with unilateral breast tumors [130]. This observation is analogous to my observation that the clonal populations that were selected for in the bilateral injection setting (A-HSE) were less chemosensitive than those in the unilateral injection setting (N-HSE). This suggests that my observations of the functional consequences of enhanced heterogeneity in our pre-clinical model may be translatable to a patient setting. Additionally, this suggests that one bilateral breast tumor may be capable of activating the systemic environment in a way that can affect the distant tumor. Future studies could reveal whether patients with bilateral tumors exhibit signs of systemic activation and if it is possible to address the systemic perturbations to improve patient outcome in this setting.

6.3 Concluding remarks

The work presented in this thesis underscores the consequential role that intratumoral heterogeneity plays in breast cancer progression and therapeutic resistance. Additionally, it provides tools that can be used in future studies to further our understanding of the biology driving the formation and maintenance of heterogeneity and its functional consequences. I hope that this work will provide motivation and allow others to continue to investigate how heterogeneity develops and to eventually identify ways to interdict these processes. I believe that future therapeutic interventions that address and combat intratumoral heterogeneity could be a valuable tool to improve patient outcomes, both independently and when used in conjunction with other therapies.

References

1. Siegel, R.L., K.D. Miller, and A. Jemal, *Cancer statistics, 2018*. CA Cancer J Clin, 2018. **68**(1): p. 7-30.
2. Gerratana, L., et al., *Pattern of metastasis and outcome in patients with breast cancer*. Clin Exp Metastasis, 2015. **32**(2): p. 125-33.
3. Dawood, S., et al., *Survival differences among women with de novo stage IV and relapsed breast cancer*. Ann Oncol, 2010. **21**(11): p. 2169-74.
4. Bertos, N.R. and M. Park, *Breast cancer - one term, many entities?* J Clin Invest, 2011. **121**(10): p. 3789-96.
5. Hu, Z., et al., *The molecular portraits of breast tumors are conserved across microarray platforms*. BMC Genomics, 2006. **7**: p. 96.
6. Sorlie, T., et al., *Repeated observation of breast tumor subtypes in independent gene expression data sets*. Proc Natl Acad Sci U S A, 2003. **100**(14): p. 8418-23.
7. Perou, C.M., et al., *Molecular portraits of human breast tumours*. Nature, 2000. **406**(6797): p. 747-52.
8. Sorlie, T., et al., *Gene expression patterns of breast carcinomas distinguish tumor subclasses with clinical implications*. Proc Natl Acad Sci U S A, 2001. **98**(19): p. 10869-74.
9. Prat, A. and C.M. Perou, *Deconstructing the molecular portraits of breast cancer*. Mol Oncol, 2011. **5**(1): p. 5-23.
10. Slamon, D.J., et al., *Human breast cancer: correlation of relapse and survival with amplification of the HER-2/neu oncogene*. Science, 1987. **235**(4785): p. 177-82.
11. Dent, R., et al., *Triple-negative breast cancer: clinical features and patterns of recurrence*. Clin Cancer Res, 2007. **13**(15 Pt 1): p. 4429-34.
12. Goldhirsch, A., et al., *Personalizing the treatment of women with early breast cancer: highlights of the St Gallen International Expert Consensus on the Primary Therapy of Early Breast Cancer 2013*. Ann Oncol, 2013. **24**(9): p. 2206-23.
13. Gupta, G.P. and J. Massague, *Cancer metastasis: building a framework*. Cell, 2006. **127**(4): p. 679-95.
14. Lambert, A.W., D.R. Pattabiraman, and R.A. Weinberg, *Emerging Biological Principles of Metastasis*. Cell, 2017. **168**(4): p. 670-691.

15. Hosseini, H., et al., *Early dissemination seeds metastasis in breast cancer*. Nature, 2016.
16. Harper, K.L., et al., *Mechanism of early dissemination and metastasis in Her2(+) mammary cancer*. Nature, 2016.
17. Maltoni, R., et al., *Circulating tumor cells in early breast cancer: A connection with vascular invasion*. Cancer Lett, 2015. **367**(1): p. 43-8.
18. Lucci, A., et al., *Circulating tumour cells in non-metastatic breast cancer: a prospective study*. Lancet Oncol, 2012. **13**(7): p. 688-95.
19. Mohme, M., S. Riethdorf, and K. Pantel, *Circulating and disseminated tumour cells - mechanisms of immune surveillance and escape*. Nat Rev Clin Oncol, 2017. **14**(3): p. 155-167.
20. Bednarz-Knoll, N., C. Alix-Panabieres, and K. Pantel, *Clinical relevance and biology of circulating tumor cells*. Breast Cancer Res, 2011. **13**(6): p. 228.
21. Luzzi, K.J., et al., *Multistep nature of metastatic inefficiency: dormancy of solitary cells after successful extravasation and limited survival of early micrometastases*. Am J Pathol, 1998. **153**(3): p. 865-73.
22. Pantel, K., R.H. Brakenhoff, and B. Brandt, *Detection, clinical relevance and specific biological properties of disseminating tumour cells*. Nat Rev Cancer, 2008. **8**(5): p. 329-40.
23. Hanahan, D. and R.A. Weinberg, *The hallmarks of cancer*. Cell, 2000. **100**(1): p. 57-70.
24. Swanton, C., *Intratumor heterogeneity: evolution through space and time*. Cancer Res, 2012. **72**(19): p. 4875-82.
25. Yates, L.R., et al., *Subclonal diversification of primary breast cancer revealed by multiregion sequencing*. Nat Med, 2015. **21**(7): p. 751-9.
26. Marusyk, A., V. Almendro, and K. Polyak, *Intra-tumour heterogeneity: a looking glass for cancer?* Nat Rev Cancer, 2012. **12**(5): p. 323-34.
27. Kreso, A., et al., *Variable clonal repopulation dynamics influence chemotherapy response in colorectal cancer*. Science, 2013. **339**(6119): p. 543-8.
28. Joyce, J.A. and J.W. Pollard, *Microenvironmental regulation of metastasis*. Nat Rev Cancer, 2009. **9**(4): p. 239-52.
29. Nowell, P.C., *The clonal evolution of tumor cell populations*. Science, 1976. **194**(4260): p. 23-8.

30. McGranahan, N. and C. Swanton, *Clonal Heterogeneity and Tumor Evolution: Past, Present, and the Future*. Cell, 2017. **168**(4): p. 613-628.
31. Marusyk, A. and K. Polyak, *Cancer. Cancer cell phenotypes, in fifty shades of grey*. Science, 2013. **339**(6119): p. 528-9.
32. Ding, L., et al., *Genome remodelling in a basal-like breast cancer metastasis and xenograft*. Nature, 2010. **464**(7291): p. 999-1005.
33. Gerlinger, M., et al., *Intratumor heterogeneity and branched evolution revealed by multiregion sequencing*. N Engl J Med, 2012. **366**(10): p. 883-92.
34. Lindstrom, L.S., et al., *Clinically Used Breast Cancer Markers Such As Estrogen Receptor, Progesterone Receptor, and Human Epidermal Growth Factor Receptor 2 Are Unstable Throughout Tumor Progression*. Journal of Clinical Oncology, 2012. **30**(21): p. 2601-2608.
35. Cleary, A.S., et al., *Tumour cell heterogeneity maintained by cooperating subclones in Wnt-driven mammary cancers*. Nature, 2014. **508**(7494): p. 113-7.
36. Marusyk, A., et al., *Non-cell-autonomous driving of tumour growth supports subclonal heterogeneity*. Nature, 2014. **514**(7520): p. 54-8.
37. Aparicio, S. and C. Caldas, *The implications of clonal genome evolution for cancer medicine*. N Engl J Med, 2013. **368**(9): p. 842-51.
38. Quail, D.F. and J.A. Joyce, *Microenvironmental regulation of tumor progression and metastasis*. Nat Med, 2013. **19**(11): p. 1423-37.
39. Dunn, G.P., et al., *Cancer immunoediting: from immunosurveillance to tumor escape*. Nat Immunol, 2002. **3**(11): p. 991-8.
40. Palucka, A.K. and L.M. Coussens, *The Basis of Oncoimmunology*. Cell, 2016. **164**(6): p. 1233-1247.
41. Yuan, Y., et al., *Quantitative image analysis of cellular heterogeneity in breast tumors complements genomic profiling*. Sci Transl Med, 2012. **4**(157): p. 157ra143.
42. McAllister, S.S. and R.A. Weinberg, *The tumour-induced systemic environment as a critical regulator of cancer progression and metastasis*. Nat Cell Biol, 2014. **16**(8): p. 717-27.
43. Redig, A.J. and S.S. McAllister, *Breast cancer as a systemic disease: a view of metastasis*. J Intern Med, 2013. **274**(2): p. 113-26.

44. Castano, Z., et al., *Stromal EGF and igf-I together modulate plasticity of disseminated triple-negative breast tumors*. *Cancer Discov*, 2013. **3**(8): p. 922-35.
45. Elkabets, M., et al., *Human tumors instigate granulysin-expressing hematopoietic cells that promote malignancy by activating stromal fibroblasts in mice*. *J Clin Invest*, 2011. **121**(2): p. 784-99.
46. Kuznetsov, H.S., et al., *Identification of luminal breast cancers that establish a tumor-supportive macroenvironment defined by proangiogenic platelets and bone marrow-derived cells*. *Cancer Discov*, 2012. **2**(12): p. 1150-65.
47. McAllister, S.S., et al., *Systemic endocrine instigation of indolent tumor growth requires osteopontin*. *Cell*, 2008. **133**(6): p. 994-1005.
48. Krall, J.A., et al., *The systemic response to surgery triggers the outgrowth of distant immune-controlled tumors in mouse models of dormancy*. *Sci Transl Med*, 2018. **10**(436).
49. Sangiovanni, A., et al., *Increased survival of cirrhotic patients with a hepatocellular carcinoma detected during surveillance*. *Gastroenterology*, 2004. **126**(4): p. 1005-14.
50. de Martel, C., et al., *Global burden of cancers attributable to infections in 2008: a review and synthetic analysis*. *Lancet Oncol*, 2012. **13**(6): p. 607-15.
51. Schulz, T.F., *Cancer and viral infections in immunocompromised individuals*. *Int J Cancer*, 2009. **125**(8): p. 1755-63.
52. Kersten, K., et al., *Mammary tumor-derived CCL2 enhances pro-metastatic systemic inflammation through upregulation of IL1beta in tumor-associated macrophages*. *Oncoimmunology*, 2017. **6**(8): p. e1334744.
53. Coffelt, S.B., et al., *IL-17-producing gamma delta T cells and neutrophils conspire to promote breast cancer metastasis*. *Nature*, 2015. **522**(7556): p. 345-348.
54. Bystrykh, L.V., et al., *Counting stem cells: methodological constraints*. *Nat Methods*, 2012. **9**(6): p. 567-74.
55. Wu, A.M., et al., *Cytological evidence for a relationship between normal hemopoietic colony-forming cells and cells of the lymphoid system*. *J Exp Med*, 1968. **127**(3): p. 455-64.
56. Harrison, D.E., C.M. Astle, and C. Lerner, *Number and continuous proliferative pattern of transplanted primitive immunohematopoietic stem cells*. *Proc Natl Acad Sci U S A*, 1988. **85**(3): p. 822-6.

57. Capel, B., et al., *Clonal contributions of small numbers of retrovirally marked hematopoietic stem cells engrafted in unirradiated neonatal W/W^v mice*. Proc Natl Acad Sci U S A, 1989. **86**(12): p. 4564-8.
58. Gerrits, A., et al., *Cellular barcoding tool for clonal analysis in the hematopoietic system*. Blood, 2010. **115**(13): p. 2610-8.
59. Lu, R., et al., *Tracking single hematopoietic stem cells in vivo using high-throughput sequencing in conjunction with viral genetic barcoding*. Nat Biotechnol, 2011. **29**(10): p. 928-33.
60. Schepers, K., et al., *Dissecting T cell lineage relationships by cellular barcoding*. J Exp Med, 2008. **205**(10): p. 2309-18.
61. Nguyen, L.V., et al., *DNA barcoding reveals diverse growth kinetics of human breast tumour subclones in serially passaged xenografts*. Nat Commun, 2014. **5**: p. 5871.
62. Nguyen, L.V., et al., *Clonal analysis via barcoding reveals diverse growth and differentiation of transplanted mouse and human mammary stem cells*. Cell Stem Cell, 2014. **14**(2): p. 253-63.
63. Wagenblast, E., et al., *A model of breast cancer heterogeneity reveals vascular mimicry as a driver of metastasis*. Nature, 2015. **520**(7547): p. 358-62.
64. Porter, S.N., et al., *Lentiviral and targeted cellular barcoding reveals ongoing clonal dynamics of cell lines in vitro and in vivo*. Genome Biol, 2014. **15**(5): p. R75.
65. Bhang, H.E., et al., *Studying clonal dynamics in response to cancer therapy using high-complexity barcoding*. Nat Med, 2015. **21**(5): p. 440-8.
66. Mathis, R.A., E.S. Sokol, and P.B. Gupta, *Cancer cells exhibit clonal diversity in phenotypic plasticity*. Open Biol, 2017. **7**(2).
67. Nolan-Stevaux, O., et al., *Measurement of Cancer Cell Growth Heterogeneity through Lentiviral Barcoding Identifies Clonal Dominance as a Characteristic of In Vivo Tumor Engraftment*. PLoS One, 2013. **8**(6): p. e67316.
68. Yu, C., et al., *High-throughput identification of genotype-specific cancer vulnerabilities in mixtures of barcoded tumor cell lines*. Nat Biotechnol, 2016.
69. Elenbaas, B., et al., *Human breast cancer cells generated by oncogenic transformation of primary mammary epithelial cells*. Genes Dev, 2001. **15**(1): p. 50-65.
70. Ince, T.A., et al., *Transformation of different human breast epithelial cell types leads to distinct tumor phenotypes*. Cancer Cell, 2007. **12**(2): p. 160-70.

71. Mitra, A., et al., *Strategies for achieving high sequencing accuracy for low diversity samples and avoiding sample bleeding using illumina platform*. PLoS One, 2015. **10**(4): p. e0120520.
72. Wong, K.H., Y. Jin, and Z. Moqtaderi, *Multiplex Illumina sequencing using DNA barcoding*. Curr Protoc Mol Biol, 2013. **Chapter 7**: p. Unit 7 11.
73. Meyerhans, A., J.P. Vartanian, and S. Wain-Hobson, *DNA recombination during PCR*. Nucleic Acids Res, 1990. **18**(7): p. 1687-91.
74. Beltman, J.B., et al., *Reproducibility of Illumina platform deep sequencing errors allows accurate determination of DNA barcodes in cells*. BMC Bioinformatics, 2016. **17**: p. 151.
75. Subramanian, A., et al., *A Next Generation Connectivity Map: L1000 Platform and the First 1,000,000 Profiles*. Cell, 2017. **171**(6): p. 1437-1452 e17.
76. Yu, C., et al., *High-throughput identification of genotype-specific cancer vulnerabilities in mixtures of barcoded tumor cell lines*. Nat Biotechnol, 2016. **34**(4): p. 419-23.
77. Day, C.P., G. Merlino, and T. Van Dyke, *Preclinical mouse cancer models: a maze of opportunities and challenges*. Cell, 2015. **163**(1): p. 39-53.
78. Duan, Q., et al., *LINCS Canvas Browser: interactive web app to query, browse and interrogate LINCS L1000 gene expression signatures*. Nucleic Acids Res, 2014. **42**(Web Server issue): p. W449-60.
79. Godar, S., et al., *Growth-inhibitory and tumor-suppressive functions of p53 depend on its repression of CD44 expression*. Cell, 2008. **134**(1): p. 62-73.
80. Wei, R., J.P.C. Wong, and H.F. Kwok, *Osteopontin -- a promising biomarker for cancer therapy*. J Cancer, 2017. **8**(12): p. 2173-2183.
81. Graudens, E., et al., *Deciphering cellular states of innate tumor drug responses*. Genome Biol, 2006. **7**(3): p. R19.
82. Minn, A.J., et al., *Genes that mediate breast cancer metastasis to lung*. Nature, 2005. **436**(7050): p. 518-24.
83. Tuck, A.B., A.F. Chambers, and A.L. Allan, *Osteopontin overexpression in breast cancer: knowledge gained and possible implications for clinical management*. J Cell Biochem, 2007. **102**(4): p. 859-68.
84. Richardson, A.L., et al., *X chromosomal abnormalities in basal-like human breast cancer*. Cancer Cell, 2006. **9**(2): p. 121-32.

85. van de Vijver, M.J., et al., *A gene-expression signature as a predictor of survival in breast cancer*. N Engl J Med, 2002. **347**(25): p. 1999-2009.
86. Ramankulov, A., et al., *Elevated plasma osteopontin as marker for distant metastases and poor survival in patients with renal cell carcinoma*. J Cancer Res Clin Oncol, 2007. **133**(9): p. 643-52.
87. Shevde, L.A., et al., *Osteopontin: an effector and an effect of tumor metastasis*. Curr Mol Med, 2010. **10**(1): p. 71-81.
88. Cheng, L., et al., *Hazard of recurrence among women after primary breast cancer treatment--a 10-year follow-up using data from SEER-Medicare*. Cancer Epidemiol Biomarkers Prev, 2012. **21**(5): p. 800-9.
89. Demicheli, R., et al., *Tumor dormancy and surgery-driven interruption of dormancy in breast cancer: learning from failures*. Nat Clin Pract Oncol, 2007. **4**(12): p. 699-710.
90. Shultz, L.D., et al., *Humanized NOD/LtSz-scid IL2 receptor common gamma chain knockout mice in diabetes research*. Ann N Y Acad Sci, 2007. **1103**: p. 77-89.
91. Campbell, M.J., et al., *Epithelial and fibroblast cell lines derived from a spontaneous mammary carcinoma in a MMTV/neu transgenic mouse*. In Vitro Cell Dev Biol Anim, 2002. **38**(6): p. 326-33.
92. Reilly, R.T., et al., *HER-2/neu is a tumor rejection target in tolerized HER-2/neu transgenic mice*. Cancer Res, 2000. **60**(13): p. 3569-76.
93. Guenet, A. and L. Grumolato, *CRISPR/Cas9 editing of the genome for cancer modeling*. Methods, 2017. **121-122**: p. 130-137.
94. Doudna, J.A. and E. Charpentier, *Genome editing. The new frontier of genome engineering with CRISPR-Cas9*. Science, 2014. **346**(6213): p. 1258096.
95. Yang, L., et al., *CRISPR/Cas9-Directed Genome Editing of Cultured Cells*. Curr Protoc Mol Biol, 2014. **107**: p. 31 1 1-17.
96. Harrod, A., et al., *Genomic modelling of the ESR1 Y537S mutation for evaluating function and new therapeutic approaches for metastatic breast cancer*. Oncogene, 2017. **36**(16): p. 2286-2296.
97. Neggers, J.E., et al., *Identifying drug-target selectivity of small-molecule CRM1/XPO1 inhibitors by CRISPR/Cas9 genome editing*. Chem Biol, 2015. **22**(1): p. 107-16.
98. Mali, P., et al., *RNA-guided human genome engineering via Cas9*. Science, 2013. **339**(6121): p. 823-6.

99. Ran, F.A., et al., *Genome engineering using the CRISPR-Cas9 system*. Nat Protoc, 2013. **8**(11): p. 2281-2308.
100. Burrell, R.A., et al., *The causes and consequences of genetic heterogeneity in cancer evolution*. Nature, 2013. **501**(7467): p. 338-45.
101. Laughney, A.M., et al., *Dynamics of Tumor Heterogeneity Derived from Clonal Karyotypic Evolution*. Cell Rep, 2015. **12**(5): p. 809-20.
102. Gupta, P.B., et al., *Stochastic state transitions give rise to phenotypic equilibrium in populations of cancer cells*. Cell, 2011. **146**(4): p. 633-44.
103. Goldberg, D.E., R.F. Siliciano, and W.R. Jacobs, Jr., *Outwitting evolution: fighting drug-resistant TB, malaria, and HIV*. Cell, 2012. **148**(6): p. 1271-83.
104. Sanchez-Romero, M.A. and J. Casadesus, *Contribution of phenotypic heterogeneity to adaptive antibiotic resistance*. Proc Natl Acad Sci U S A, 2014. **111**(1): p. 355-60.
105. Chait, R., et al., *Pervasive selection for and against antibiotic resistance in inhomogeneous multistress environments*. Nat Commun, 2016. **7**: p. 10333.
106. Levin-Reisman, I., et al., *Antibiotic tolerance facilitates the evolution of resistance*. Science, 2017. **355**(6327): p. 826-830.
107. Borowsky, A.D., et al., *Syngeneic mouse mammary carcinoma cell lines: two closely related cell lines with divergent metastatic behavior*. Clin Exp Metastasis, 2005. **22**(1): p. 47-59.
108. Plumer, A., et al., *Development of fragment-specific osteopontin antibodies and ELISA for quantification in human metastatic breast cancer*. BMC Cancer, 2008. **8**: p. 38.
109. Gu, T., et al., *Osteopontin is involved in the development of acquired chemo-resistance of cisplatin in small cell lung cancer*. Lung Cancer, 2009. **66**(2): p. 176-83.
110. Jia, R., et al., *Osteopontin facilitates tumor metastasis by regulating epithelial-mesenchymal plasticity*. Cell Death Dis, 2016. **7**(12): p. e2564.
111. Liu, G., et al., *Osteopontin induces autophagy to promote chemo-resistance in human hepatocellular carcinoma cells*. Cancer Lett, 2016. **383**(2): p. 171-182.
112. Pang, H., et al., *Knockdown of osteopontin chemosensitizes MDA-MB-231 cells to cyclophosphamide by enhancing apoptosis through activating p38 MAPK pathway*. Cancer Biother Radiopharm, 2011. **26**(2): p. 165-73.

113. Sangaletti, S., et al., *Osteopontin shapes immunosuppression in the metastatic niche*. *Cancer Res*, 2014. **74**(17): p. 4706-19.
114. Singhal, H., et al., *Elevated plasma osteopontin in metastatic breast cancer associated with increased tumor burden and decreased survival*. *Clin Cancer Res*, 1997. **3**(4): p. 605-11.
115. Xu, Y.Y., et al., *Prognostic value of osteopontin expression in breast cancer: A meta-analysis*. *Mol Clin Oncol*, 2015. **3**(2): p. 357-362.
116. Luo, S.D., et al., *Osteopontin Involves Cisplatin Resistance and Poor Prognosis in Oral Squamous Cell Carcinoma*. *Biomed Res Int*, 2015. **2015**: p. 508587.
117. Ding, K., et al., *Overexpression of osteopontin promotes resistance to cisplatin treatment in HCC*. *Oncol Rep*, 2015. **34**(6): p. 3297-303.
118. Ng, L., et al., *Osteopontin Overexpression Induced Tumor Progression and Chemoresistance to Oxaliplatin through Induction of Stem-Like Properties in Human Colorectal Cancer*. *Stem Cells Int*, 2015. **2015**: p. 247892.
119. Cook, A.C., et al., *Osteopontin induces multiple changes in gene expression that reflect the six "hallmarks of cancer" in a model of breast cancer progression*. *Mol Carcinog*, 2005. **43**(4): p. 225-36.
120. Feng, F. and S.R. Rittling, *Mammary tumor development in MMTV-c-myc/MMTV-v-Ha-ras transgenic mice is unaffected by osteopontin deficiency*. *Breast Cancer Res Treat*, 2000. **63**(1): p. 71-9.
121. Wai, P.Y., et al., *Osteopontin silencing by small interfering RNA suppresses in vitro and in vivo CT26 murine colon adenocarcinoma metastasis*. *Carcinogenesis*, 2005. **26**(4): p. 741-51.
122. Wein, L. and S. Loi, *Mechanisms of resistance of chemotherapy in early-stage triple negative breast cancer (TNBC)*. *Breast*, 2017. **34 Suppl 1**: p. S27-S30.
123. Greaves, M., *Evolutionary determinants of cancer*. *Cancer Discov*, 2015. **5**(8): p. 806-20.
124. Schmitt, M.W., L.A. Loeb, and J.J. Salk, *The influence of subclonal resistance mutations on targeted cancer therapy*. *Nat Rev Clin Oncol*, 2016. **13**(6): p. 335-47.
125. Zardavas, D., et al., *Clinical management of breast cancer heterogeneity*. *Nat Rev Clin Oncol*, 2015. **12**(7): p. 381-94.
126. Gerashchenko, T.S., et al., *Intratumoral Morphological Heterogeneity of Breast Cancer As an Indicator of the Metastatic Potential and Tumor Chemosensitivity*. *Acta Naturae*, 2017. **9**(1): p. 56-67.

127. Gerdes, M.J., et al., *Single-cell heterogeneity in ductal carcinoma in situ of breast*. *Mod Pathol*, 2018. **31**(3): p. 406-417.
128. Holmes, M.D., et al., *Aspirin intake and survival after breast cancer*. *J Clin Oncol*, 2010. **28**(9): p. 1467-72.
129. Rice, M.S., et al., *Breast Cancer Research in the Nurses' Health Studies: Exposures Across the Life Course*. *Am J Public Health*, 2016. **106**(9): p. 1592-8.
130. Reinisch, M., et al., *pCR rates in patients with bilateral breast cancer after neoadjuvant anthracycline-taxane based-chemotherapy - A retrospective pooled analysis of individual patients data of four German neoadjuvant trials*. *Breast*, 2017. **32**: p. 73-78.